UNIVERSIDADE FEDERAL DE SÃO CARLOS
CENTRO DE CIÊNCIAS EXATAS E DE TECNOLOGIA
DEPARTAMENTO DE QUÍMICA
PROGRAMA DE PÓS-GRADUAÇÃO EM QUÍMICA

"*IN SITU* CHEMICAL OXIDATION OF CIPROFLOXACIN BY ACTIVATED PEROXYMONOSULFATE USING NANOMETRIC MnOOH: INVESTIGATION OF OPERATIONAL PARAMETERS AND CHANGES ON THE CATALYST SURFACE"

Yeison Núñez de la Rosa*

Thesis presented as part of the requirements to obtain the title of DOCTOR IN SCIENCES, concentration area: PHYSICAL-CHEMISTRY

Advisor: Prof. Dr. José Mario de Aquino

***Scholarship Holder of CAPES (Coordination of Superior Level Staff Improvement)**

São Carlos - SP

2023

UNIVERSIDADE FEDERAL DE SÃO CARLOS

Centro de Ciências Exatas e de Tecnologia
Programa de Pós-Graduação em Química

Folha de Aprovação

Defesa de Tese de Doutorado do candidato Yeison Neder Nuñez de La Rosa, realizada em 24/05/2023.

Comissão Julgadora:

Prof. Dr. José Mario de Aquino (UFSCar)

Profa. Dra. Raquel Fernandes Pupo Nogueira (UNESP)

Prof. Dr. Diogo Paschoalini Volanti (UNESP)

Profa. Dra. Lúcia Helena Mascaro Sales (UFSCar)

Prof. Dr. Luis Augusto Martins Ruotolo (UFSCar)

O Relatório de Defesa assinado pelos membros da Comissão Julgadora encontra-se arquivado junto ao Programa de Pós-Graduação em Química.

"El mundo habrá acabado de joderse —dijo entonces— el día en que los hombres viajen en primera clase y la literatura en el vagón de carga."

Gabriel García Márquez
Cien años de soledad

ACKNOWLEDGMENTS

Thank you all for helping me achieve my goals over the last few years. I couldn't have done it without your support. This section is dedicated to listing all the people who have been a part of my journey, and to saying thank you for all your help.

I thank my supervisor, José Mario for being supportive leader who has helped me grow in my career. He is always available to help and makes room for me in his busy schedule. Thank you for all the time and effort you put into helping me with my PhD research. Your contributions were invaluable. Professor José, I appreciate your guidance and advice throughout our partnership. You have been a great supervisor and I have always felt supported by you. Your encouragement has helped me grow as a researcher and as a person. I am grateful for your help.

My doctoral research would not have been possible without the excellent working conditions I experienced at the LaPE. I would like to express my heartiest appreciation to Drs. Romeu Cardozo Rocha Filho, Nerilso Bocchi, Sonia Regina Biaggio, and my fellow lab-mates. I also thank the secretaries of the PPGQ-UFSCar (Ariane, Cristina, and Luciani) for their behind-the-scenes work that allowed me to successfully complete this journey.

No acknowledgment of mine would be complete without thanking my friends, for always having my back, even from a distance. In particular, I thank *Zorra* and *Luchy,* my dearest lifelong friends.

Por último, pero no menos importante, le agradezco enormemente a mi familia por su apoyo incondicional, amor y dedicación para conmigo. A mis padres Boris y María, por haberme forjado como la persona que soy hoy en día, mis más grandes agradecimientos por alentarme a seguir adelante y perseguir mis objetivos. A mis hermanos Melisa, Jonathan, Yamid y Katerine, que han sido mi ejemplo de vida, les agradezco por cuidarme, aconsejarme y guiarme. A mi esposa Victoria, muchas gracias por el apoyo, dedicación, cariño y compañía durante los momentos más atribulados de este duro camino.

Finally, I also thank the Brazilian funding agencies, CAPES (Finance Code 001), CNPq (grants #465357/2014-8, #302186/2019-0, #305943/2020-0, #406537/2021-6, and #307800/2021-0), and FAPESP (#2014/50918-7 and #2019/07943-4) for the scholarships and financial support.

¡A todos, muchas gracias!

Yeison Núñez D.

SCIENTIFIC PRODUCTION RELATED TO THIS THESIS

The results obtained in this doctoral research have been published in an international journal:

NÚÑEZ-DE LA ROSA, YEISON; CUADRADO DURANGO, LUIS GUILLERMO; FORIM, MOACIR ROSSI; NASCIMENTO, OTACIRO RANGEL; HAMMER, PETER; AQUINO, JOSÉ M. Unraveling the time evolution and *post mortem* changes of nanometric MnOOH during *in situ* oxidation of ciprofloxacin by activated peroxymonosulfate. *Applied Catalysis B: Environmental*, v. 327, 2023.

In addition, the PhD candidate has collaborated with other researchers, from which is co-author of the following publications:

SÁNCHEZ-MONTES, ISAAC; CARNEIRO DOERENKAMP, JUSSARA; **NÚÑEZ-DE LA ROSA, YEISON**; HAMMER, PETER; ROCHA-FILHO, ROMEU; AQUINO, JOSÉ M. Effective Fenton-like degradation of the tebuthiuron herbicide by ferrocene functionalized g-C_3N_4. *Journal of Photochemistry and Photobiology A: Chemistry*, v. 435, 2022.

PINTO, THAIS T.; **NÚÑEZ-DE LA ROSA, YEISON**; HAMMER, PETER; AQUINO, JOSÉ M. On the performance of self-organized TiO_2 nanotubes@MnO_x as supercapacitor: Influence of the heat treatment, cathodic treatment, water aging, and thermal oxides. *Electrochimica Acta*, v. 408, 2022.

LIST OF ABBREVIATIONS

CIP – ciprofloxacin antibiotic

CV – cyclic voltammetry

DMPO – 5,5-dimethyl-1-pyrroline N-oxide

ESR – electron spin resonance

EI – Electrochemical impedance

HRTEM – high-resolution transmission electron microscopy

$HO^{\bullet}$ – hydroxyl radical

HPLC – high-performance liquid chromatography

MnOOH – manganese oxyhydroxide (as-prepared)

3-MnOOH - manganese oxyhydroxide after 3 h of treatment

6-MnOOH - manganese oxyhydroxide after 6 h of treatment

$^1O_2$ – singlet oxygen

PDS – peroxydisulfate

PMS – peroxymonosulfate

$SO_4^{\bullet-}$ – sulfate radical

TEMP – 2,2,6,6-tetramethyl-4-piperidine

TOC – total organic carbon

UHPLC-QToF MS – ultra-high performance liquid chromatography coupled to a time-of-flight mass analyzer

XRD – X-ray diffraction

XPS – X-ray photoelectron spectroscopy

LIST OF TABLES

LIST OF FIGURES

RESUMO

OXIDAÇÃO QUÍMICA *IN SITU* DA CIPROFLOXACINA MEDIADA PELA ATIVAÇÃO DE PEROXIMONOSULFATO USANDO MnOOH NANOMÉTRICO: INVESTIGAÇÃO DE PARÂMETROS OPERACIONAIS E MUDANÇAS NA SUPERFÍCIE DO CATALISADOR. − O composto nanométrico MnOOH foi sintetizado (por uma abordagem verde), caracterizado e usado para remover o antibiótico Ciprofloxacina (CIP) por oxidação química *in situ* usando peroximonossulfato (PMS). O efeito de diferentes concentrações de MnOOH, PMS e pH, as mudanças morfológicas, estruturais, químicas e eletroquímicas foram estudados durante e após os experimentos. A molécula CIP foi completamente oxidada e parcialmente mineralizada (~ 60%) após 6 h sob condições ácidas. O mecanismo de degradação do CIP foi conduzido por oxidantes gerados ($HO^{\bullet}$ e $^1O_2$) durante a ativação *in situ* do PMS e, em menor grau, diretamente na superfície do MnOOH. Este último processo foi confirmado por microscopia eletrônica de transmissão mostrando a formação de uma camada amorfa (MnOx) sobre cristais de MnOOH, também verificado por espectroscopia de fotoelétrons de raios X e o subsequente aumento da resistência à transferência de carga que impediu uma transferência adicional de elétrons para o oxidante PMS. Esse comportamento parece ser recuperável ao ser empregada uma solução PMS recém-preparada.

ABSTRACT

IN SITU CHEMICAL OXIDATION OF CIPROFLOXACIN BY ACTIVATED PEROXYMONOSULFATE USING NANOMETRIC MnOOH: INVESTIGATION OF OPERATIONAL PARAMETERS AND CHANGES ON THE CATALYST SURFACE. − Nanometric MnOOH compound was synthesized by a green approach, characterized, and used to remove ciprofloxacin (CIP) antibiotic by *in situ* chemical oxidation using peroxymonosulfate (PMS). The effects of varying concentrations of MnOOH, PMS and pH, on morphological, structural, chemical, and electrochemical changes were studied during and after the experiments. The CIP molecule was completely oxidized and partially mineralized (~ 60%) after 6 h under acidic conditions. The mechanism of CIP degradation was induced by PMS activated oxidants ($HO^{\bullet}$ and $^1O_2$) and, to a lesser extent, directly on the surface of MnOOH. The latter process was evidenced by transmission electron microscopy showing the formation of an amorphous shell (MnO_x) over MnOOH crystallites, as verified using X-ray photoelectron spectroscopy and the subsequent increase of the charge transfer resistance that hindered a further electron transfer to the PMS oxidant. Such behavior is recoverable when using a freshly prepared PMS solution.

TABLE OF CONTENTS

PREAMBLE

This thesis is an adaptation of the article "*Unraveling the time evolution and post mortem changes of nanometric MnOOH during in situ oxidation of ciprofloxacin by activated peroxymonosulfate*" by Yeison Núñez-de la Rosa, Luis Guillermo Cuadrado Durango, Moacir Rossi Forim, Otaciro Rangel Nascimento, Peter Hammer, and José M. Aquino.

Applied Catalysis B: Environmental, DOI: 10.1016/j.apcatb.2023.122439

Applied Catalysis B: Environmental 327 (2023) 122439

Contents lists available at ScienceDirect

Applied Catalysis B: Environmental

journal homepage: www.elsevier.com/locate/apcatb

Unraveling the time evolution and *post mortem* changes of nanometric MnOOH during *in situ* oxidation of ciprofloxacin by activated peroxymonosulfate

Yeison Núñez-de la Rosa [a], Luis Guillermo Cuadrado Durango [a], Moacir Rossi Forim [a], Otaciro Rangel Nascimento [b], Peter Hammer [c], José M. Aquino [a,*]

[a] Federal University of São Carlos (UFSCar), Departament of Chemistry, 13565-905 São Carlos, SP, Brazil
[b] University of São Paulo (USP), São Carlos Institute of Physics, Department of Physics and Interdisciplinary Science, 13560-970 São Carlos, SP, Brazil
[c] São Paulo State University (UNESP), Institute of Chemistry, Department of Physical Chemistry, 14800-900 Araraquara, SP, Brazil

1 - INTRODUCTION AND GOALS

The constant need for freshwater supply has been increasingly affected by pollution and climate change, resulting in an unprecedented change in the water cycle[1]. Consequences include water scarcity and poor quality for human consumption[2]. In turn, the quality of water for human consumption is directly associated with basic sanitation conditions, as well as the type of treatment methods used for water supply and after its disposal[3].

A report on the evolution of water for consumption, sanitation, and hygiene by the United Nations Children's Foundation (UNICEF) and the World Health Organization (WHO)[4] points to an improvement in the quality of services and supply of water for consumption worldwide from 2000 to 2017. In Brazil, over 75% of the proportion use basic water services (municipal water, wells water, protected dug wells, protected springs, and bottled water), a proportion similar to that for basic sanitation. It is worth noting that these are average values; therefore, in most cases, the complexity of our country is not represented. However, Brazil still faces some shortcomings concerning basic sanitation, which means that a large part of its population has access neither to public treatment supplies nor adequate wastewater disposal.

According to the Brazilian institution *Sistema Nacional de Informações sobre Saneamento*, in 2020, only 79.8% of the collected wastewater were treated; therefore, just over 20% of the wastewater, that is, 1.2 billion m^3, were released directly into the environment. The discharge of wastewater without proper treatment is one of the main sources of pollution of water bodies in Brazil and a major facilitator for emerging contaminants to enter the environment[5].

Since hosting the meeting sponsored by the United Nations (UN) in Rio de Janeiro in 1992 (Rio 92), Brazil has stood out as a pioneer in promoting an international union for sustainable development, human development, and

environmental protection. In continuation of the agreements signed on that date, the 2030 Agenda for Sustainable Development (SD) commits UN member states to take bold and transformative steps to “change the world to a sustainable and resilient path”, “make practicable the human rights of all”, “ending poverty in all its forms", and ensuring that "no one is left behind". The sixth goal of the SD is to ensure the availability and sustainable management of water and sanitation access to drinking water for all. Aligned, the third goal addresses universal health coverage since water quality and the presence or absence of basic sanitation is the source of several health problems.

The contamination of water supply and effluents with emerging contaminants is a much-discussed subject in the literature and is linked to water issues and the SD goals with the UN [6]. Most of these compounds are synthetic, such as personal hygiene products, antibiotics, plasticizers, agricultural pesticides, and textile dyes, thus representing a real risk to water bodies (surface and underground)[7] since they can remain in the environment without being degraded (recalcitrant) by natural organisms[8]. For example, Le Coadou *et al.*[9] and Chow *et al.*[10] detected different amounts of synthetic organic compounds at trace levels, such as hormones, pharmaceuticals, and polyfluoroalkylated substances, in bottled water in France and the United States. In Brazil, specifically in the state of São Paulo, Montagner *et al.*[11] detected 58 different compounds (8 industrial compounds, 9 hormones, 10 illicit drugs, 14 pharmaceuticals, and 17 pesticides) in various water matrices collected from 13 cities, 10 rivers, 4 reservoirs, and 5 wastewater treatment plants (WWTPs). Other studies have reported the presence of organic pollutants in various water sources around the world [11–14].

Regarding water contamination with pharmaceuticals, the literature has indicated that different types and concentrations of antibiotics have been widely detected in rivers, lakes, and seawater worldwide (see TABLE 1.1), with quinolones as one of the main types of antibiotics detected in surface waters since they are highly consumed globally [15].

Antibiotic	CAS number	Country	Average concentration (ng L^{-1})	Reference
Amoxicillin	26787-78-0	Brazil	4 – 8	Montagner *et al.* 2018[11]
		France	5 – 21	Dinh *et al.* 2017[16]
		Kenya	900-1600	Kairigo *et al.* 2020[17]
Cephalexin	15686-71-2	Brazil	575.5	Monteiro *et al.* 2017[18]
		Costa Rica	50-10000	Ramírez-Morales *et al.* 2020[19]
		Iran	2 – 2.4	Kafaei *et al.* 2018[20]
Ciprofloxacin	85721-33-1	Brazil	15.7 – 572	Monteiro *et al.* 2017[18]
		China	9800 – 55200	Li *et al.* 2018[21]
		Colombia	500	Botero-Coy *et al.* 2018[22]
		France	89 – 3400	Dinh *et al.* 2017[16]
		Mexico	83 – 1190	Lesser *et al.* 2018[23]
		Portugal	339	Fernandes *et al.* 2020[24]
		Sweden	83 – 1406	Östman *et al.* 2017[25]
Enrofloxacin	93106-60-6	China	0.4 – 0.9	Zhang *et al.* 2020[26]
		France	636	Dinh *et al.* 2017[16]
Norfloxacin	70458-96-7	Brazil	2 - 4	Montagner *et al.* 2018[11]
		China	0.3 – 0.8	Zhang *et al.* 2020[26]
		France	97 – 9347	Dinh *et al.* 2017[16]
Ofloxacin	82419-36-1	China	45.3	Yao *et al.* 2017[27]
		France	805-8637	Dinh *et al.* 2017[16]
		Portugal	120	Fernandes *et al.* 2020[24]

TABLE 1.1 – Some antibiotics detected in different water matrices.

Both human and veterinary medicines widely use quinolones, one of the largest classes of antibiotics, to treat various bacterial infections. Fluoroquinolones (FQNs) stand out among the derivatives of quinolones and have the basic chemical structure of quinolones (FIGURE 1.1) with a fluorine atom in the C6 position. Its most commonly used form contains a heterocycle with nitrogen in the C7 position, such as norfloxacin (NOR), ofloxacin (OFX), enrofloxacin (ENR), and ciprofloxacin (CIP) (FIGURE 1.2)[28].

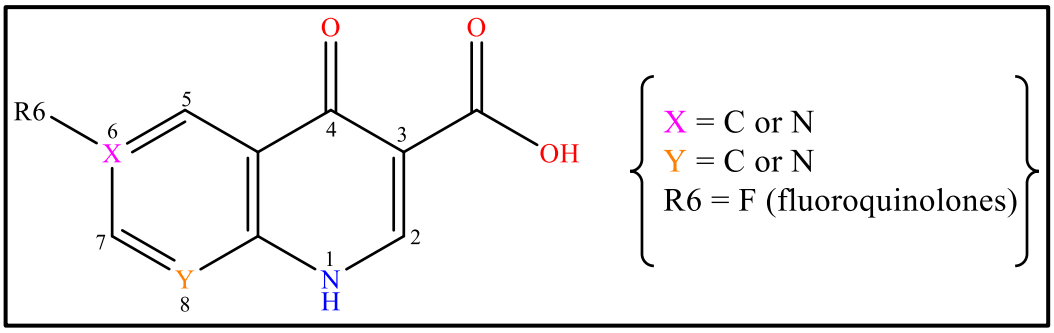

FIGURE 1.1 – General structure of quinolones and fluoroquinolones (Source: adapted from Lungu *et al.* 2022[28]).

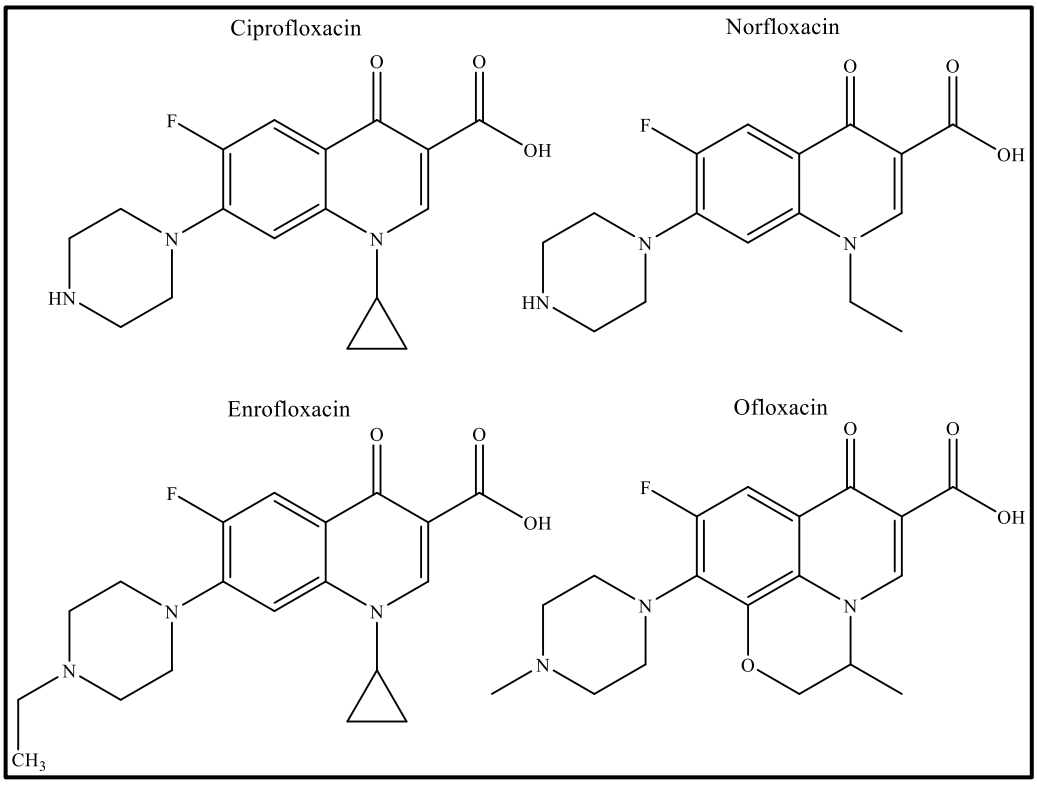

FIGURE 1.2 – Molecular structures of some fluoroquinolones (Source: adapted from Lungu *et al.* 2022[28]).

At present, NOR, CIP, and OFX are mainly used for the treatment of human diseases, while ENR is exclusively used for animal treatments. The bactericidal effect of FQNs involves a mechanism of action that inhibits bacterial DNA replication and transcription. This mechanism is carried out by interacting with the enzymes *i*) Topoisomerase II, essential to initiate the replication process,

and *ii*) Topoisomerase IV, important for the separation of replicated chromosomal DNA during cell division.

After administration, a significant part of the drugs is excreted by humans, and the effluents containing them go directly to wastewater treatment plants. WWTPs are the last barrier to prevent pollutants present in wastewater from entering the environment directly; however, most of these facilities mostly deal with conventional aspects of pollution, such as sedimentable and suspended solids, organic material, nutrients, and some pathogenic microorganisms that cause diseases. Many wastewaters treatment processes have limited ability to treat antibiotics, and antibiotics remaining in the effluent continue to accumulate and diffuse into the environment. FIGURE 1.3[15] shows other routes for these pollutants to enter the environment, such as effluents from pharmaceutical factories, hospital materials, expired drugs improperly discarded, and animal waste[28].

Once in water bodies and even after being submitted to primary, secondary, and tertiary treatment processes, antibiotics can cause harmful effects on human health, even in very low concentrations (ng L^{-1}), due to chronic exposure[8,29,30]. This leads to serious problems such as allergic reactions, alteration of the microbiome, disruption of digestive system functions, and antimicrobial resistance (AMR)[31,32]. It is worth noting that this latter issue emerges when microorganisms, such as bacteria, viruses, parasites, and fungi, evolve, adapt, and become immune to the drugs to which they were previously vulnerable. The more microorganisms are exposed to pharmaceuticals, the more likely they are to adapt to them.

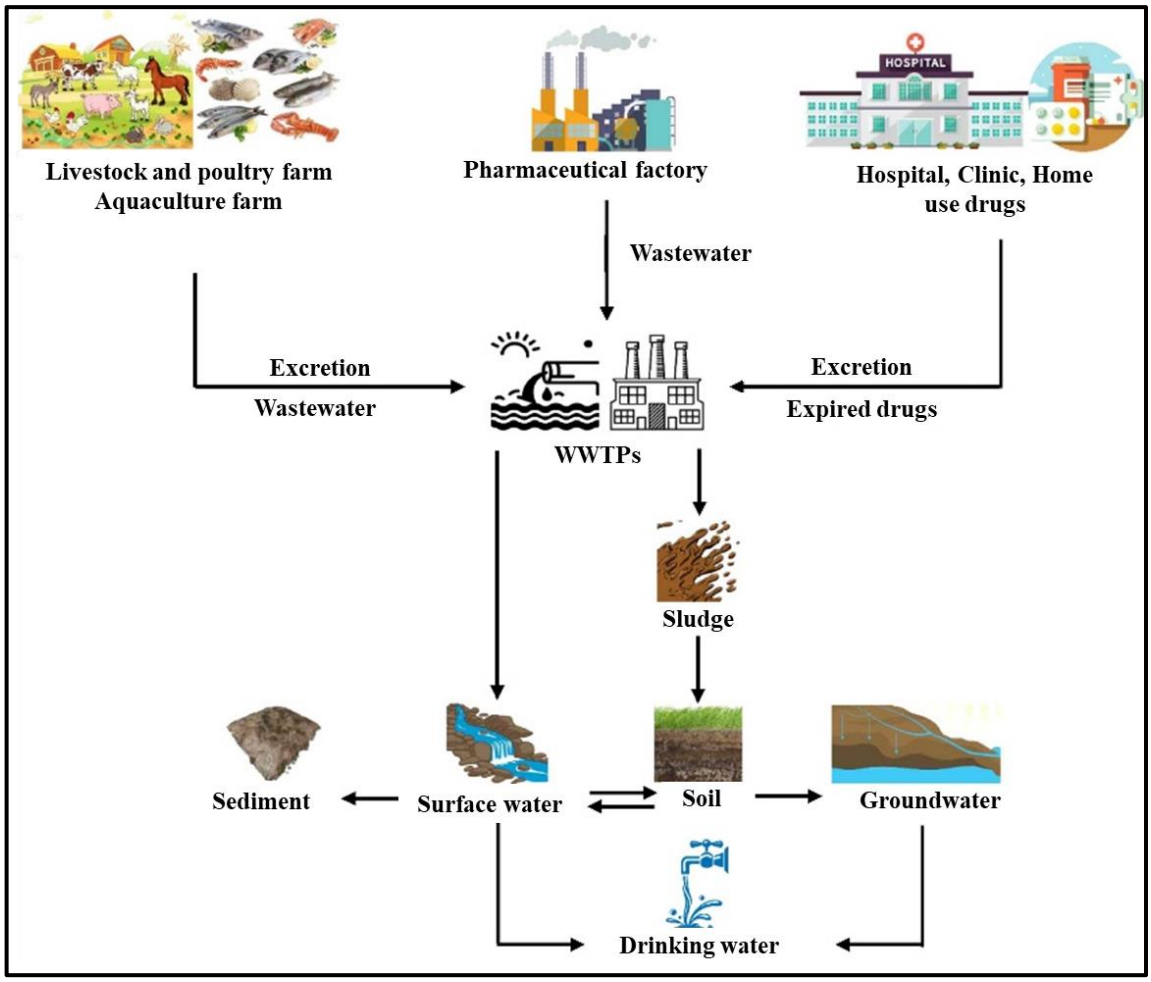

FIGURE 1.3 – Routes of entry and transport of drugs in the environment (Source: figure reproduced from Zou *et al*. 2022[15] allowed by Elsevier).

According to the most recent report by the United Nations Environment Programme (UNEP)[33], AMR can trigger the emergence of drug-resistant pathogens and potentially another global pandemic. Globally, not enough attention has been paid to the threat that AMR poses, with most antibiotics being released into the environment. In 2015, 34.8 billion antibiotic doses were consumed out of which about 90% were excreted in the environment still as active substances. In 2019, infections that showed resistance to antibiotics were associated with the death of nearly 5 million people. If no immediate action is taken, it is estimated that these infections might have caused up to 10 million yearly deaths globally by 2050[33]. Furthermore, the newest report on the global antimicrobial resistance and use surveillance system (GLASS) by the WHO,

published at the end of 2022[34], revealed that bacteria are frequently responsible for bloodstream infections in hospitals, such as *Klebsiella pneumoniae* and *Acinetobacter spp.*, which showed high levels of resistance. These life-threatening infections require treatment with antibiotics of last resort, such as carbapenems. However, 8% of bloodstream infections caused by *Klebsiella pneumoniae* have been reported to be resistant to carbapenems, increasing the risk of death due to uncontrollable infections. The statement also highlights a resistance of over 20% to antibiotics, such as ampicillin, cotrimoxazole, and some fluoroquinolones, in *E. coli*, the most common pathogen in urinary tract infections. Also of concern is the high resistance of the *bacterium Neisseria gonorrhoeae*, which causes gonorrhea (a sexually transmitted disease), towards CIP, which can be greater than 60%. These antibiotics are often used in the oral treatment of some other infections, and such high resistance in very common pathogens is of great concern. Thereby, the situation is delicate from the point of view not only of water pollution but also of human health.

Thus, the growing concern about environmental issues imposes the high priority of developing new technologies to treat water containing emerging contaminants. Advanced oxidative processes (AOPs)[35] are an interesting option among the methods currently available to treat distinct water sources contaminated with organic pollutants. Advanced oxidative processes, including the Fenton reaction, electrochemical oxidation, ozonation, sulfate radical-based advanced oxidative processes (SR-AOPs), etc., can completely degrade organic pollutants by generating highly oxidizing species, such as hydroxyl ($HO^{\bullet}$), sulfate ($SO_4^{\bullet-}$), and superoxide ($O_2^{\bullet-}$) radicals, as well as non-radical species like singlet oxygen ($^1O_2$).

Numerous research works on the degradation of organic pollutants by AOPs have mostly focused on the generation of the hydroxyl radical since its high oxidative power[36] can react non-selectively with organic molecules. Considering its short period of half-life, the $HO^{\bullet}$ radical (~1 ns)[37] is generated *in*

situ during processes based on H_2O_2 activation. The most studied systems in the literature are *i*) photolysis of hydrogen peroxide with UV radiation (UV/H_2O_2), *ii*) Fenton (Fe^{2+}/H_2O_2), and *iii*) photo-Fenton ($UV/Fe^{2+}/H_2O_2$)[36,38]. In the former, the generation of the $HO^{\bullet}$ species is affected by the photolysis of H_2O_2 with UV radiation. In the Fenton-based processes, the $HO^{\bullet}$ radical is produced in an acidic solution (pH 3) by activating H_2O_2, via electron transfer, in the presence of Fe^{2+} ions. Often, UV-vis light is irradiated in the solution (photo-Fenton) for the *in situ* recovery of Fe^{2+} ions, consequently promoting the additional generation of $HO^{\bullet}$ radicals[39]. However, the application of AOPs for H_2O_2 activation is partially limited to the acidic conditions of the solution and the natural decomposition of H_2O_2[40].

Alternatively, the use of $SO_4^{\bullet-}$ radicals is promising due to its longer half-life (~40 μs)[41] and an oxidation potential comparable to the $HO^{\bullet}$ radical ($E°(SO_4^{\bullet-}/SO_4^{2-})$ from +2.60 to +3.10 V_{NHE} and $E°(HO^{\bullet}/HO^{-})$ from +1.90 to +2.70 V_{NHE}, depending on the solution pH)[41–43]. This first condition allows the $SO_4^{\bullet-}$ radical to diffuse a little more through the solution to interact with the polluting organic compound. The reaction of the $SO_4^{\bullet-}$ radical is mainly dictated by oxidation via one electron (Eq. 1), in addition to hydrogen abstraction and addition to C-C type double bonds in organic compounds[43]. Depending on the solution pH, the $SO_4^{\bullet-}$ radical can also react with the OH^- ion (mainly at pH > 9) to produce $HO^{\bullet}$ radicals (Eq. 2).

$$SO_4^{\bullet-} + e^- \rightarrow SO_4^{2-} \quad (1)$$

$$SO_4^{\bullet-} + OH^- \rightarrow SO_4^{2-} + HO^{\bullet} \quad (2)$$

Commonly, $SO_4^{\bullet-}$ radicals are produced by activating the oxidant HSO_5^- (peroxymonosulfate, PMS) or $S_2O_8^{2-}$ (peroxydisulfate, PDS) through thermal activation, photolysis with UV irradiation, homogeneous catalysis using metallic ions (Fe^{2+}, Co^{2+}, Ag^+, Cu^{2+}), or heterogeneous catalysis using metallic oxides and carbon-based compounds[44–52]. Both PMS and PDS can also lead to the

oxidation of organic compounds without involving radical species, as well as through[43] *i*) direct electron transfer, *ii*) formation of high valence species, and *iii*) formation of $^1O_2$, particularly for PMS.

The chemical structures of PMS and PDS are characterized by having an O−O peroxide bond, like H_2O_2 (see FIGURE 1.4). However, the difference between their reactivity derives mainly from this bond, as in PMS it is asymmetric with a partially positive charge induced on the hydrogen-bound peroxide oxygen and with an O−O bond distance of 1.460 Å, with a dissociation energy of 377 kJ mol^{-1}. In the case of PDS, it has a symmetrical charge distribution, a longer binding distance (1.497 Å)[41], and a lower dissociation energy (92 kJ mol^{-1})[43]. Furthermore, the steric hindrance due to the presence of two -SO_3 groups on either side of the O−O bond (see FIGURE 1.4) makes PDS less reactive than PMS with organic molecules containing bulky groups[44,53].

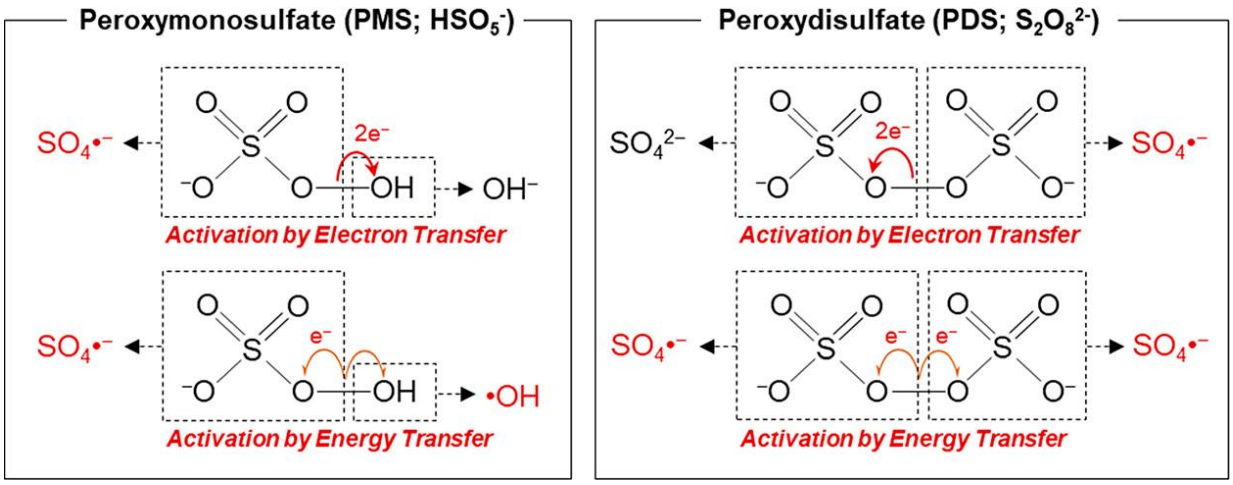

FIGURE 1.4 – Chemical structure and activation mechanism of peroxydisulfate (PDS) and peroxymonosulfate (PMS) by electron- and energy-transfer processes (Source: figure reproduced from Lee *et al.* 2020[43] allowed by the ACS).

These structural differences between PMS and PDS oxidants generate different activation processes. For example, energy transfer processes such as thermolysis and photolysis, which involve homolytic cleavage of the peroxide bond, are more effective in activating PDS than PMS, due to the lower

dissociation energy of the O−O bond. In contrast, PMS is more effectively activated to produce $SO_4^{\bullet-}$ radicals in processes mediated by electron transfer using transition metals, carbon-based catalysts, or metal oxides[43].

The field of environmental science has increasingly studied the PMS oxidant. It has been used as an oxidant in organic synthesis to produce oxidizing species since it has a lower oxidation potential than PDS (1.82 V_{NHE} for PMS and 2.08 V_{NHE} for PDS). Such a characteristic allows PMS to be an oxidizing or reducing agent in the reaction medium, also depending on the conditions adopted to activate it. In addition to radical species, PMS can lead to the production of $^1O_2$. A possible mechanism in the presence of PMS with metallic ions in solution is based on the redox cycle, as shown in equations 3 to 5, with the formation of $HO^{\bullet}$ or $SO_4^{\bullet-}$ radicals; in addition to the recovery of the metallic species at the end of the reaction.

$$M^{n+} + HSO_5^- \rightarrow M^{(n+1)+} + SO_4^{\bullet-} + OH^- \quad (3)$$

$$M^{n+} + HSO_5^- \rightarrow M^{(n+1)+} + SO_4^{2-} + HO^{\bullet} \quad (4)$$

$$M^{(n+1)+} + HSO_5^- \rightarrow M^{n+} + SO_5^{\bullet-} + H^+ \quad (5)$$

The $SO_5^{\bullet-}$ species formed can generate $^1O_2$ by reacting with H_2O (Eq. 6). Furthermore, $^1O_2$ can be generated via self-decomposition of PMS, where protonated and non-protonated HSO_5^- species react with each other (Eq. 7).

$$2SO_5^{\bullet-} + H_2O \rightarrow 2HSO_4^- + 1.5\,^1O_2 \quad (6)$$

$$HSO_5^- + SO_5^{2-} \rightarrow HSO_4^- + SO_4^{2-} + {}^1O_2 \quad (7)$$

The $^1O_2$ oxidant is weaker than $HO^{\bullet}$ and $SO_4^{\bullet-}$ radicals ($E°(^1O_2/O_2^{\bullet-})$ = +0.81 V_{NHE})[43,54], in addition to being highly selective, reacting through reactions of electrophilic addition and electron abstraction[55]. Notwithstanding, it has the advantage of not reacting with interfering species (commonly found in natural, supply, and effluent waters), such as inorganic and those represented by OH^- ions,

halides, oxyanions (HCO_3^-, CO_3^{2-}, HPO_4^{2-}, $H_2PO_4^-$, etc.), or dissolved organic matter (humic acids and others)[43]. Such a characteristic allows $^1O_2$ to react almost exclusively with emerging contaminants compared to $HO^\bullet$ and $SO_4^{\bullet-}$ species.

In recent times, manganese-based oxides have been used for different water treatment applications due to their various properties, such as wide resources, low toxicity, multiple oxidation states of Mn (basically II, III, and IV), and catalytic reactivity[56]. Considering the *in situ* activation of oxidants by Mn-based oxides catalysts, a large number of studies investigated the homolytic cleavage of PMS to generate $HO^\bullet$ and $SO_4^{\bullet-}$ radicals for the degradation of organic pollutants[57,58]. Liu *et al.*[59] used a magnetic nanocomposite based on Fe_3O_4 (magnetite) and MnO_2 for the degradation of 4-chlorophenol. The use of nanometric Fe_3O_4 aims to facilitate its separation and subsequent reuse in other experiments. The work demonstrated that the nanocomposite synthesized at the Fe:Mn molar proportion of 4:1 resulted in the complete oxidation of 4-chlorophenol (50 mg L^{-1}) during a 30-min experiment mineralizing over 50% of the organic load in this same time interval. The use of tert-butanol and ethanol as scavengers showed that the organic compound is preferentially oxidated by the $SO_4^{\bullet-}$ radical. This was demonstrated by the much smaller decrease in the oxidation rate with the use of tert-butanol in the experiments (it reacts preferentially with the $HO^\bullet$ radical). The mechanism proposed for PMS activation involves the reaction of HSO_5^- with surface Mn(IV) to produce Mn(III) (Eq. 8 and 9). Then, the latter reacts with another molecule of HSO_5^- to form the radical $SO_4^{\bullet-}$and Mn(IV) (Eq. 10 and 11).

$$\equiv Mn^{IV} - OH + HSO_5^- \rightarrow \equiv Mn^{IV} - (O)OSO_3^- + H_2O \quad (8)$$

$$\equiv Mn^{IV} - (O)OSO_3^- + H_2O \rightarrow \equiv Mn^{III} - OH + SO_5^{\bullet-} + H^+ \quad (9)$$

$$\equiv Mn^{III} - OH + HSO_5^- \rightarrow \equiv Mn^{III} - (O)OSO_3^- + H_2O \quad (10)$$

$$\equiv Mn^{III} - (O)OSO_3^- + H_2O \rightarrow \equiv Mn^{IV} - OH + SO_4^{\bullet-} + OH^- \quad (11)$$

The Mn(III) species can also react with Fe(III) from magnetite, reducing it to Fe(II), which, in turn, can also react with HSO_5^- to form $SO_4^{\bullet-}$ radicals and Fe(III) again (Eq 12-14).

$$\equiv Mn^{III} - OH + Fe^{III} - OH \rightarrow \equiv Mn^{IV} - OH + \equiv Fe^{II} - OH \quad (12)$$

$$\equiv Fe^{II} - OH + HSO_5^- \rightarrow \equiv Fe^{II} - (O)OSO_3^- + H_2O \quad (13)$$

$$\equiv Fe^{II} - (O)OSO_3^- + H_2O \rightarrow SO_4^{\bullet-} + Fe^{III} - OH + OH^- \quad (14)$$

The $HO^{\bullet}$ radicals might be generated due to the reaction of $SO_4^{\bullet-}$ with H_2O, as in Eq. 15:

$$SO_4^{\bullet-} + H_2O \rightarrow HO^{\bullet} + H^+ + SO_4^{2-} \quad (15)$$

Saputra *et al.*[60] investigated the effect of different crystalline phases of nanometric MnO_2 (α, β, and γ) for the activation of PMS and degradation of phenol. The difference between these phases lies in the manner in which the fundamental structures of MnO_6 are packaged. As the PMS is activated by this molecule interacting with the catalyst surface, it is expected that samples with greater adsorption towards organic molecules result in higher oxidation rates, which was true for the α-MnO_2 phase. Furthermore, the greater variation in oxidation states ($Mn^{4+} \rightarrow Mn^{3+} \rightarrow Mn^{2+}$) in this last phase facilitated the activation of PMS. Saputra *et al.*[61] also investigated the effect of the Mn oxidation state (such as MnO, Mn_2O_3, Mn_3O_4, and MnO_2) on PMS activation. As Mn has different oxidation states in solids, the activation of PMS can generate two different radicals: $SO_4^{\bullet-}$ or $SO_5^{\bullet-}$, as shown in some chemical reactions below (Eq. 16-20):

$$HSO_5^- + 2MnO_2 \rightarrow Mn_2O_3 + SO_5^{\bullet-} + OH^- \quad (16)$$

$$HSO_5^- + 2Mn_3O_4 \rightarrow 3Mn_2O_3 + SO_4^{\bullet-} + H^+ \quad (17)$$

$$HSO_5^- + Mn_2O_3 \rightarrow 2MnO_2 + SO_4^{\bullet-} + H^+ \quad (18)$$

$$HSO_5^- + 2MnO \rightarrow Mn_2O_3 + SO_4^{\bullet-} + H^+ \quad (19)$$

$$HSO_5^- + 3Mn_2O_3 \rightarrow 2Mn_3O_4 + SO_5^{\bullet -} + OH^- \quad (20)$$

These results showed that Mn_2O_3 has the highest ability to activate PMS when considering the investigated four manganese oxide compounds. This occurs because Mn(III) species can undergo disproportionation reaction and the resulting species promote the electron transfer between the catalyst and PMS molecules. Therefore, the structure of manganese oxides and the content of Mn(III) on the surface of such compounds play a critical role in the oxidative and catalytic reactivity of manganese oxides. The commonly reported Mn(III)-based catalysts include Mn_2O_3, Mn_3O_4, and MnOOH (manganese oxyhydroxide). Among them, MnOOH has received increasing attention from the scientific community because of its efficient electron transfer rate, high surface-active sites and surface hydroxyl sites[61,62].

He *et al.*[63] investigated the activation of PMS by γ-MnOOH (with different morphologies) for the degradation of 2,4-dichlorophenol. The obtained results showed that the catalytic activity of γ-MnOOH decreased from nanowires to multi-branches and then to nanorods. Different parameters, such as specific surface area, zeta potential, and redox potential were measured to investigate the reason why distinct morphologies resulted in distinct catalytic performances of γ-MnOOH. The key role on the catalytic activity was played by the surface charge density (*i.e.* zeta potential), as it promotes the interfacial reactivity between PMS and MnOOH surface sites.

Currently, MnOOH composites have also been used for the degradation of pollutants (see TABLE 1.2) due to their several synergistic effects (*e.g.*, generation of surface defects, improvement of material's stability and catalytic activity).

Catalysts	Pollutant	Experimental conditions	Reactivity	Active Species	Ref.
γ-MnOOH-rGO	Bentazone	[Catalyst] = 75 mg L^{-1} [PMS] = 615 mg L^{-1} [Betazone] = 10 mg L^{-1} pH = 7; sunlight	96% removal of Bentazone in 90 min	$HO^{\bullet}$ $^1O_2$	Li, *et al.* 2020[64]
MnOOH@nylon	2,4-dichlorophenol	[Catalyst] = 0.76 mg cm^2 [PMS] = 138 mg L^{-1} [2,4-DCP] = 25 mg L^{-1} pH = 6	97.9% removal of 2,4-DCP in 120 min	$HO^{\bullet}$ $^1O_2$ $SO_4^{\bullet-}$ $O_2^{\bullet-}$	Zhang, *et al.* 2021[65]
$NiCo_2O_4$/MnOOH/GO	Ciprofloxacin	[Catalyst] = 0.15 g L^{-1} [PMS] = 30.44 mg L^{-1} [CIP] = 6.63 mg L^{-1} pH = 7	99% removal of CIP in 30 min	$HO^{\bullet}$ $^1O_2$ $SO_4^{\bullet-}$ $O_2^{\bullet-}$	Nguyen, *et al.* 2022[66]
Mn_3O_4/γ-MnOOH	Norfloxacin	[Catalyst] = 0.2 g L^{-1} [NOR] = 10 mg L^{-1} pH = 7, sunlight, magnetic field	98.8% removal of NOR in 60 min	$O_2^{\bullet-}$ h^+	Li, *et al.* 2021[67]

TABLE 1.2 – Summary of degradation of pollutants by MnOOH composites.

Kamagate *et al*.[68] reported the important role of MnO_2 and manganite in oxidizing norfloxacin (NOR) antibiotic and oxide-bound Mn(II) species to activate persulfate. The performances of using manganite were similar for organic oxidation and mineralization[68]. The authors also observed the MnO_2/NOR system showed an increase in the concentration of dissolved Mn(II) species over time. The issue of Mn(II) (and other species) leaching is particularly problematic and limits, in many cases, the reuse of manganese oxides and other catalysts. Therefore, some studies have focused on minimizing such an issue, as investigated by Liu *et al.*[69] by using a carbon layer over Mn_3O_4 nanoparticles. The carbon-coated particles exhibited low values of charge transfer resistance for higher carbon amounts due to the improvement of electrical conductivity and oxidant activation. All these strategies are important to design better catalysts and avoid contamination with metallic ions. However, little attention has been paid to the time evolution of the Mn oxide catalyst during and after activation (*post-*

mortem) using distinct oxidants, although it is crucial for developing efficient catalysts.

Thus, this thesis aimed to synthesize, characterize and apply MnOOH oxyhydroxide nanoparticles to activate the PMS oxidant in the degradation of the ciprofloxacin (CIP) antibiotic. More specifically, we studied the influence of MnOOH and PMS concentration, as well as the solution pH on the PMS activation. For this purpose, the main oxidants produced during the CIP degradation were studied using electron spin resonance (ESR) and the produced organic intermediates were identified through liquid chromatography coupled to high-resolution mass spectrometry (UHPLC-QToF MS). In addition, to understand the deactivation process of MnOOH, we investigated the time evolution of MnOOH morphology, crystalline structure, superficial oxidation state, and electrochemical parameters using high-resolution transmission electron microscopy (HRTEM), X-ray photoelectron spectroscopy (XPS), and electrochemical measurements.

2 - MATERIALS AND METHODS

2.1 − Chemical reagents

All chemicals, including CIP (ciprofloxacin hydrochloride monohydrate, EMS), $KMnO_4$ (analytical reagent - a.r. Sigma Aldrich), $C_{12}H_{22}O_{11}$ (a.r. Synth), $MnSO_4$ (a.r. Sigma Aldrich), HNO_3 (a.r., Qhemis), NaOH (a.r Impex), H_2SO_4 (a.r., JTBaker), PMS (available as Oxone®, $KHSO_5 \cdot 0.5KHSO_4 \cdot 0.5K_2SO_4$, Sigma Aldrich), DMPO (5,5-dimethyl-1-pyrroline N-oxide, a.r. CaymanChem), TEMP (2,2,6,6-tetramethyl-4-piperidine, a.r. Sigma Aldrich), $Na_2S_2O_3$ (a.r. Synth), CH_3OH (HPLC grade, JTBaker), and HCOOH (a.r., JTBaker) were used as received without prior treatment. All solutions were prepared using deionized water (Millipore Milli-Q Academic system, $\rho \geq 18.2$ MΩ cm).

2.2 – Synthesis of MnOOH

MnOOH was prepared according to the procedure reported in the work of Crisostomo *et al.*[70] with some modifications. Briefly, 50 mL of a 0.19 mol L^{-1} $KMnO_4$ solution was slowly added under constant stirring to a previously prepared solution containing 0.5 g of sucrose in 7.5 mL of water in the presence of 0.75 mL of concentrated HNO_3 (65% *m/V*). Then, 10 mL of a 0.65 mol L^{-1} $MnSO_4$ solution was slowly dripped to the mixture. The resultant solution was refluxed at ~100 °C for 1 h. After hot filtration, the brown solid product was washed with deionized water and vacuum dried using a desiccator.

2.3 – MnOOH characterization

X-ray diffraction (XRD) experiments were performed using a D8 Advanced ECO (Bruker) instrument in the reflection mode (Cu-$K_{\alpha 1}$ radiation of 1.54 Å, 40 kV, and 25 mA) at a scanning rate of 1° min^{-1} from 10° to 80° (2θ). The surface morphology was analyzed using a TECNAI G^2 F20 (FEI) high-resolution transmission electron microscopy (HRTEM).

The surface elemental analysis of MnOOH was carried out by XPS using a commercial spectrometer (UNI-SPECS UHV) with a base pressure lower than 10^{-7} Pa. The Mg Kα line was used ($h\nu$ = 1254.6 eV) as the ionization source and the pass energy of the analyzer was set to 15 eV. The inelastic background of the C 1s, O 1s, and Mn $2p_{3/2}$ high-resolution spectra was subtracted using the Shirley method. The composition was determined by the relative proportions of the peak areas corrected by the Scofield's atomic sensitivity factors with an accuracy of ±5%. The deconvolution of the experimental spectra was performed using a Voigtian type function, with Gaussian (70%) and Lorentzian (30%) combinations. The width at half height varied between 1.0 and 2.0 eV and the position of the peaks was determined with an accuracy of ±0.1 eV with respect to the hydrocarbon peak located at 295.0 eV.

Electrochemical impedance (EI) measurements (±10 mV of perturbation from 5 kHz to 1 mHz) and cyclic voltammetry (CV) measurements (20 mV s^{-1}) were performed in an acidified (H_2SO_4, pH 3) 0.1 mol L^{-1} Na_2SO_4 solution at ambient conditions and using a conventional three-electrode cell with a Pt foil and an Ag/AgCl/KCl (3 mol L^{-1}) as a counter and reference electrode, respectively. The working electrode was composed of a carbon paper substrate as current collector on which a slurry containing a mixture of MnOOH (75% *m/m*), prepared at different treatment times (as-prepared, 3 h, and 6 h), XC-72 carbon (20% *m/m* from Cabot) and polyvinylidene fluoride (5% *m/m* from Sigma Aldrich) was deposited by drop coating. The slurry was previously mashed in an

agate mortar and dispersed in 500 μL of N-methyl pyrrolidone. Before electrochemical assays, the as-prepared electrodes were dried at 60 ºC for 12 h. All measurements were carried out in the dark.

To further confirm the oxidation state of manganese in MnOOH (before and during degradation experiments at specific time intervals), a potentiometric titration method originally described by Vetter and Jaeger[71] and adapted by Cheng *et al.*[72] was used. Briefly, 50 mg of MnOOH was dissolved in 25 mL of a 0.25 mol L^{-1} $FeSO_4$ solution acidified with H_2SO_4 (Eq. 21). Then, the solution was diluted to 100 mL with deionized water. The resulting mixture was titrated using a previously standardized 0.5 mol L^{-1} $KMnO_4$ solution (Eq. 22) to obtain the first endpoint (V_1). Subsequently, $Na_4P_2O_7 \cdot 10H_2O$ (solid) was added to the previous solution until a pH value between 6 and 7 was reached. Finally, titration was resumed (Eq. 23) until the second endpoint (V_2) was reached. The *x* value of the equations was calculated according to (Eq. 24).

$$MnO_x \cdot mH_2O + (2x\text{-}2)Fe^{2+} + 2xH^+ \rightarrow Mn^{2+} + (2x\text{-}2)Fe^{3+} + (x+m)H_2O \quad (21)$$

$$5Fe^{2+} + MnO_4^- + 8H^+ \rightarrow 5Fe^{3+} + Mn^{2+} + 4H_2O \quad (22)$$

$$4Mn^{2+} + MnO_4^- + 8H^+ + 15H_2P_2O_7^{2-} \rightarrow 5Mn(H_2P_2O_7)_3^{3-} + 4H_2O \quad (23)$$

$$x = 1 + \left(\frac{5\times(V_0 - V_1)}{2\times[(4\times V_2) - V_1]}\right) \quad (24)$$

where V_0 is the endpoint volume of the same $KMnO_4$ solution in the blank titration, *i.e.*, without MnOOH. The endpoint of each titration was determined using a potentiometer with a Pt electrode and an Ag/AgCl/KCl (3 mol L^{-1}) as reference electrode.

All previous measurements were carried out for the as-prepared MnOOH and after 3 h (3-MnOOH) and 6 h (6-MnOOH) of treatment. For this purpose, before analysis, the catalyst samples were collected at specific times (3

and 6 h), filtered, washed three times with deionized water, and dried under vacuum in a desiccator for 12 h.

2.4 – Oxidation and mineralization of CIP

The *in situ* chemical activation of PMS using MnOOH for the oxidation and mineralization of CIP (50 mg L^{-1} – see chemical structure in FIGURE 1.2) was carried out in a glass vessel (1.5 L) equipped with a magnetic stirrer. The PMS solution was continuously added to the reaction vessel during experiments using a peristaltic pump at 0.12 mL min^{-1}. The effect of different parameters such as the solution pH (3.0, 7.0, and 10.0), MnOOH dosage (0.5, 1.0, and 2.0 g L^{-1}), and PMS concentration (1.0, 2.0, and 4.0 g L^{-1}) were evaluated. The solution pH was continuously monitored and adjusted by adding concentrated H_2SO_4 or NaOH solutions (5 mol L^{-1}). Other operational variables, such as the solution volume, treatment time, solution temperature, and stirring were kept constant at 1.0 L, 360 min, 25 °C, and 600 rpm, respectively. Samples were collected from the reaction mixture at predetermined time intervals, filtered through a 0.22 μm cellulose acetate cartridge, and quenched with excess $Na_2S_2O_3$ (1.0 mol L^{-1}), except when residual oxidant was quantified.

After optimization of the experimental conditions, a recycling test (5 consecutive degradation experiments) was carried out. For this purpose, after each run, the MnOOH compound was recovered by vacuum filtration, washed thoroughly with deionized water, and dried under vacuum before further use.

2.5 – Analyses of degradation experiments

The evolution of the CIP concentration was monitored by high-performance liquid chromatography (HPLC, Shimadzu 20A) at 270 nm and using a core-shell C-18 reversed-phase column as the stationary phase (150 mm × 4.6

mm i.d., 5 μm particle size, 100 Å pore size, from Phenomenex®). A mixture of aqueous 0.1% (*V/V*) formic acid (eluent A) and methanol (eluent B) was used as the mobile phase in a gradient elution mode in the following sequence: from 10% to 90% of B in 10 min and then, back to 10% after 3 min. The last condition was kept for 2 min before subsequent analyses. The flow rate, injection volume, and temperature of the column were kept fixed at 1.0 mL min^{-1}, 25 μL, and 24 °C, respectively.

The intermediates formed during the CIP degradation process were determined by ultra-high performance liquid chromatography coupled to a time-of-flight mass analyzer (UHPLC-QToF MS), according to a methodology described in TEXT A1 available in the APPENDIX A.

The short-chain carboxylic acids were also determined by HPLC. For such, a RezexTM ROA-H column (300 mm × 7.8 mm i.d., 8 μm particle size, from Phenomenex®) as the stationary phase and a 2.5 mmol L^{-1} H_2SO_4 solution as the mobile phase were used at 0.5 mL min^{-1}. The carboxylic acids were identified by comparing their retention times with those of previously analyzed standards. The injection volume, detection wavelength, and the temperature of the column were 25 μL, 210 nm, and 23 °C, respectively.

Inorganic ions were also analyzed by HPLC with a conductivity detector (Shimadzu CDD-10A SP). For anion determination, a Shodex SI-52 4E column at 45 °C and 3.6 mmol L^{-1} Na_2CO_3 solution at 0.8 mL min^{-1} was used as the stationary and mobile phases, respectively. For this analysis, a chemically suppressor system (Thermo Scientific™ ACRS 500) pumping a regenerating solution of 3.6 mmol L^{-1} H_2SO_4 at 0.8 mL min^{-1} was used. Concerning cation determination, a Shodex YS-50 column at 40 °C and a mixture of 4.0 mmol L^{-1} oxalic acid and 6.0 $mmol^{-1}$ tartaric acid solution at 1.0 mL min^{-1} were used without the suppressor system.

The amount of residual oxidant was determined using the spectrophotometric method adapted from the work of Liang *et al.*[73]. Briefly, 2.9 mL of a 0.6 mol L^{-1} KI solution and 0.06 mol L^{-1} $NaHCO_3$ solution were added to 1.0 mL of sample previously filtered. The resulting solutions were hand-shaken and allowed to equilibrate for 15 min before analysis in a UV-Vis spectrophotometer (Shimadzu UV-1800) at 352 nm.

Total organic carbon concentration ([TOC]) was measured with a GE Sievers Innovox analyzer. The [TOC] determination was performed after mixing a diluted volume of sample with $Na_2S_2O_8$ (30% *m/V*) and H_3PO_4 (6 mol L^{-1}) solutions. The TOC content was analyzed by subtraction of the measured values of inorganic and total carbon, in terms of produced CO_2. More experimental details can be found in our previous works[74, 75].

To identify the main working oxidant species, ESR tests were also carried out using DMPO and TEMP solutions as spin probes to confirm the presence of radicals (mainly $HO^{\bullet}$) and non-radicals ($^1O_2$) oxidant species, respectively. The ESR measurements were performed in an E-109 X-band Varian system spectrometer, using a rectangular cavity at room temperature. A 200 μL flat quartz cell was used to analyze samples. To elucidate the chemical structure of the main byproducts resulting from DMPO oxidation, UHPLC-QToF MS analyses were carried out. All these experimental details can be seen in TEXT A2, available in the APPENDIX A.

3 - RESULTS AND DISCUSSIONS

3.1 − Characterization of MnOOH

FIGURE 3.1a shows TEM images of the as-prepared MnOOH oxyhydroxide compound. The morphology of the catalyst exhibited a rod-like structure with a length and diameter ranging from 130 to 270 nm and 20–30 nm, respectively, corroborating the work of Crisostomo *et al.*[70]. To confirm the crystallinity of MnOOH nanoparticles HRTEM micrography can be seen in FIGURE 3.1b. The lattice fringe spacing was close to 3.4 Å, corresponding to the $(11\bar{1})$ diffraction plane of MnOOH[70].

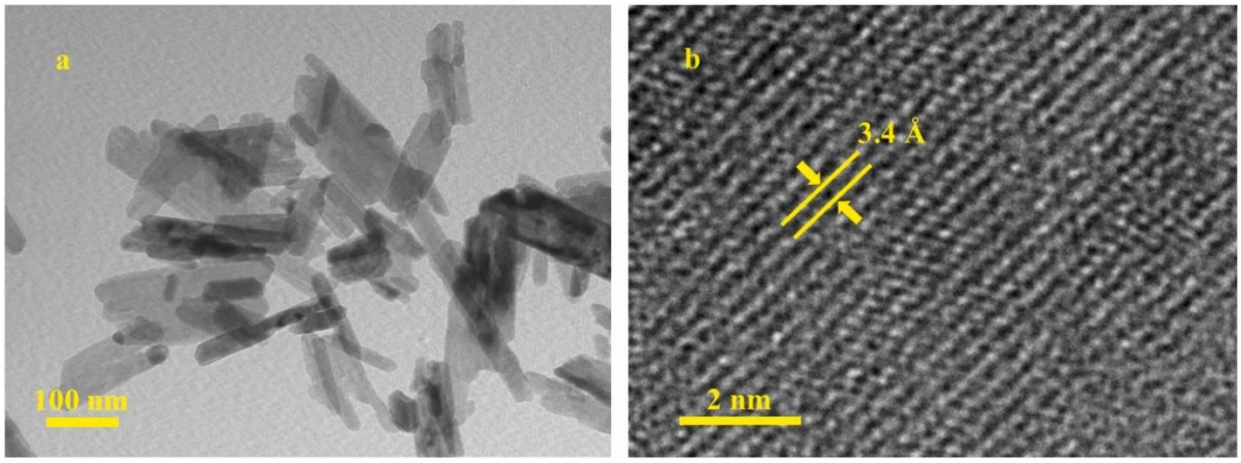

FIGURE 3.1 − **a)** Transmission electron microscope (TEM) image and **b)** high-resolution TEM (HRTEM) of the as-prepared MnOOH.

FIGURE 3.2 shows the XRD of the as-prepared catalyst on which the diffraction pattern can be indexed to the ICSD card number 98–008–4949. No impurities were observed in the XRD pattern.

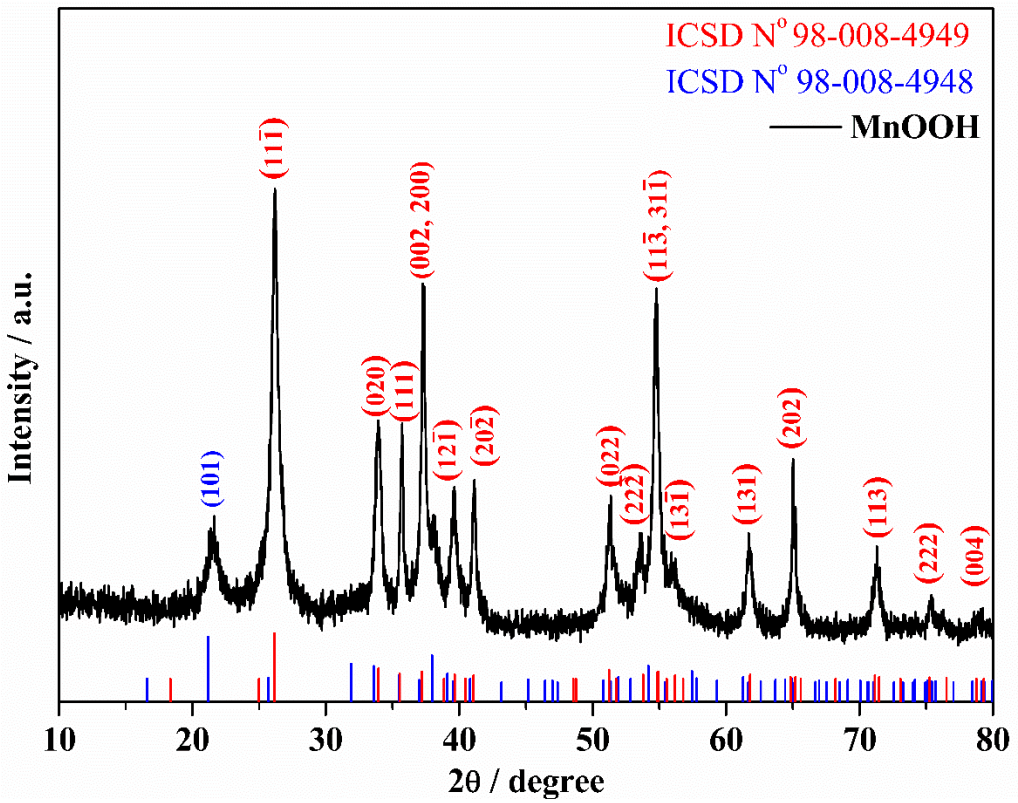

FIGURE 3.2 − X-ray diffraction (XRD) patterns of the as-prepared MnOOH compound. Note: most peaks were in accordance with the ICSD card Nº 98-008-4949 (Manganite), expect the diffraction peak at ~20º. This last seems to refer to another crystalline phase of MnOOH (ICSD Nº 98-008-4948: Groutite).

To further confirm the surface composition of the MnOOH, XPS analyses were performed. As shown in FIGURE 3.3, the high-resolution C 1s spectrum was deconvoluted into four peaks related to hydrocarbons (C–H) at 284.8 eV and oxygenated groups of alcohol/ether (C–O type at 286.2 eV), carbonyl (C=O at 287.8 eV), and carboxyl (–O–C=O at 289.4 eV)[76]. The presence of carbon functional groups is typical for *ex situ* analysis and derives mainly from physiosorbed surface contamination. However, it cannot be excluded that part of these functional groups, such as carboxyl was attached to the catalyst during the synthesis procedure and during longer treatment periods. These functional groups have to be taken into account in terms of the adsorption performance of MnOOH[77], as discussed below.

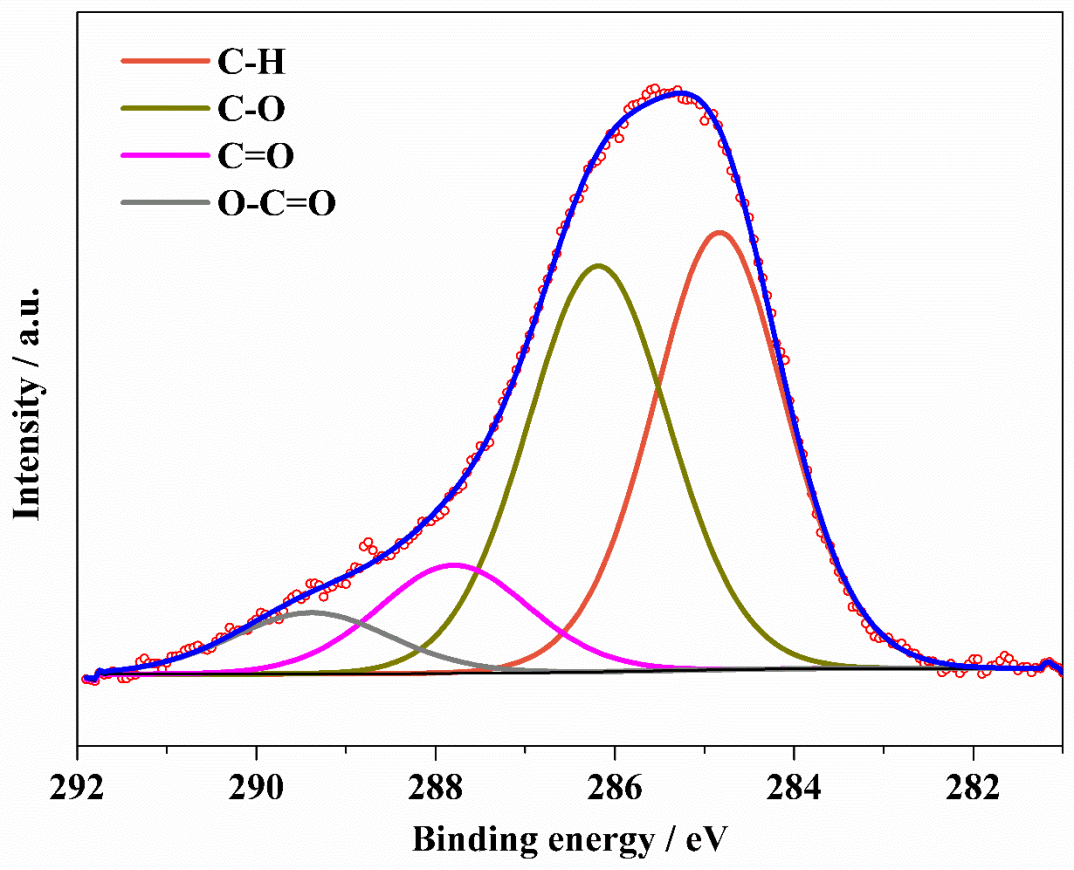

FIGURE 3.3 − High-resolution XPS spectrum of C 1s for the as-prepared MnOOH compound.

The signals of O 1s were resolved into four peaks, as can be seen in FIGURE 3.4a. The main components of all spectra are related to O–Mn (O^{-2}) type bonds at 529.5 eV and hydroxyl groups (HO–Mn) on the oxide/hydroxyl near surface at 530.8 eV[76]. In addition, the components of oxygenated groups at 530.8 eV (O=C), 532.1 eV (O–C), and 533.1 eV (O–C=O) were previously identified in the C 1s spectrum. Besides, the peaks of Mn $2p_{3/2}$ spectrum (FIGURE 3.4b) were resolved into four peaks corresponding to MnO (640.7 eV), MnOOH/Mn_2O_3 (642.1 eV), MnO_2 (643.5 eV), and MnO_3 (645.0 eV)[76]. The above results confirm the successful synthesis of MnOOH.

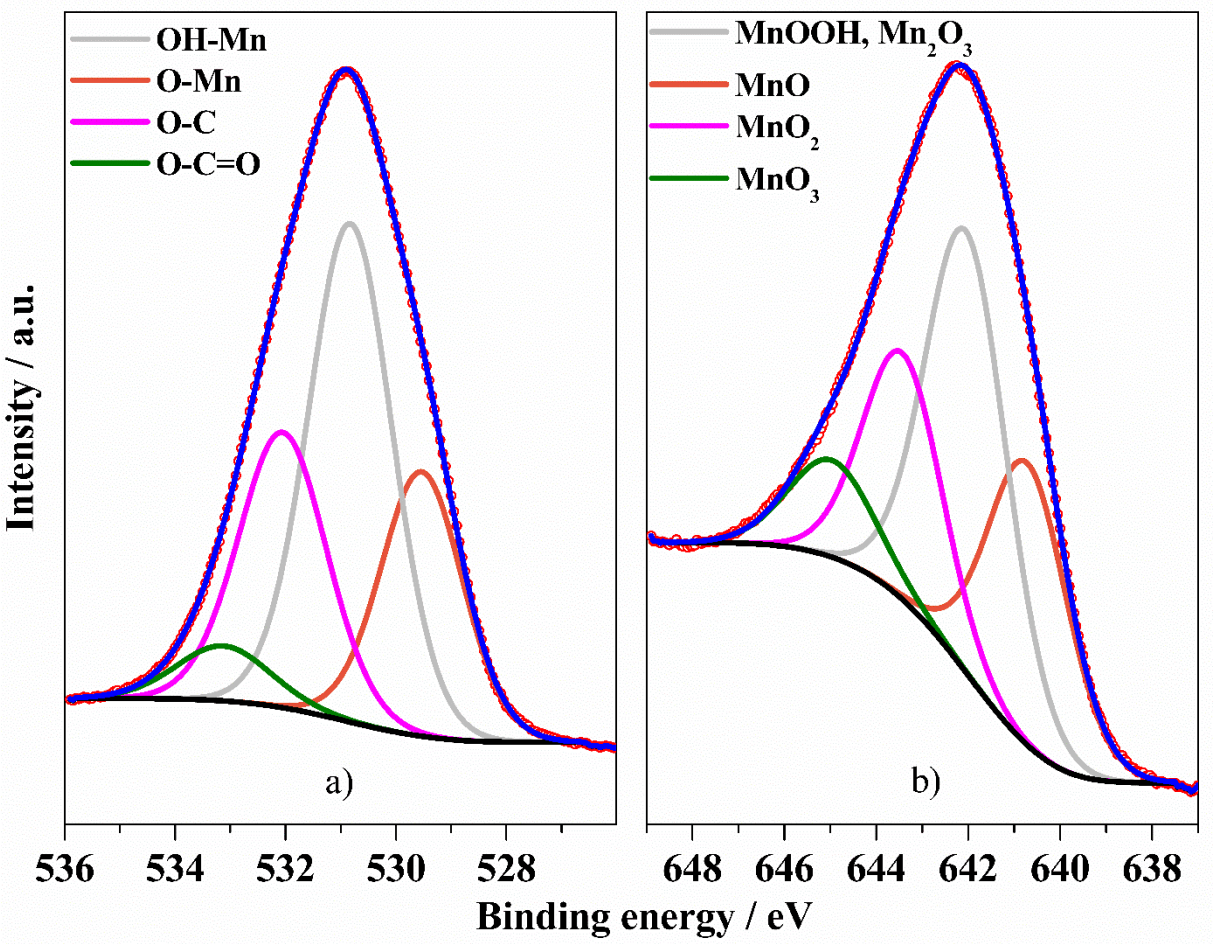

FIGURE 3.4 − High-resolution XPS spectra of **a)** O 1s and **b)** Mn $2p_{3/2}$ for the MnOOH compound for the as-prepared MnOOH

3.2 − Catalytic performance evaluation

3.2.1 − Performance of MnOOH/PMS system on CIP decomposition

FIGURE 3.5 shows the evolution of the remaining fraction of CIP and TOC as a function of treatment time using 1.0 g L^{-1} of MnOOH and PMS at pH 3.0. The catalytic activity and adsorption performance of MnOOH were first monitored. As can be observed in FIGURE 3.5a, ~25% CIP was adsorbed and/or oxidized in MnOOH after 6 h (see discussion below), which is likely due to hydrogen bonding between pollutant and the oxygen-containing functional groups in the catalyst, such as hydroxyl[78, 79]. The sole use of PMS led to 80% of CIP oxidation and only 10% converted to CO_2 at the same treatment time (the

observed TOC values fluctuation is quite common when low abatement values are attained[80, 81]). That behavior is probably due to the direct hydroxylation/dealkylation reaction on the piperazine ring of CIP by PMS[82, 83]. When catalyst and PMS were combined, the CIP molecule was completely oxidized in 3 h, whereas 60% of mineralization was achieved. To confirm whether the coupling was synergistic or not, CIP and TOC removal levels for the uncombined experiments (control experiments) were summed, as represented by the dashed line (named as theoretical line) in FIGURE 3.5. As the CIP and TOC removal levels using the MnOOH/PMS system were higher than the theoretical line (control experiments), a synergistic process was confirmed due to the *in situ* activation of PMS by MnOOH to produce powerful oxidizing species (see below).

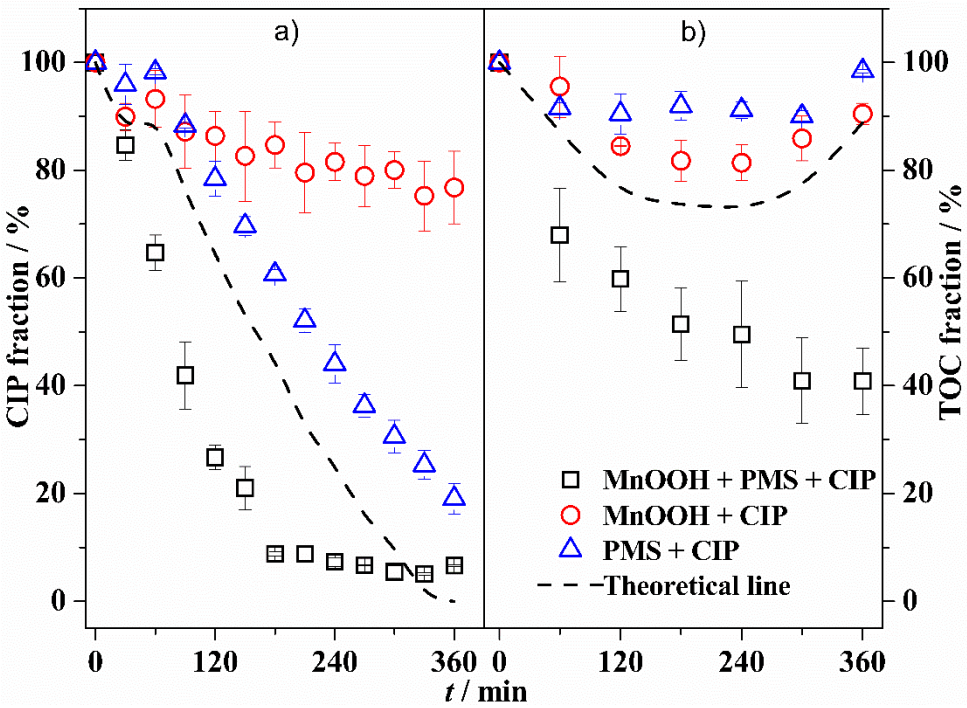

FIGURE 3.5 − Remaining fraction of CIP (CIP fraction) and TOC (TOC fraction) as a function of treatment time (t) for (○) adsorption performance of MnOOH, (△) oxidation by PMS alone, and (□) oxidation by the MnOOH/PMS system. The theoretical line is based on the sum of uncombined experiments (− −). Conditions: 50 mg L^{-1} CIP, 1.0 g L^{-1} MnOOH, 1.0 g L^{-1} PMS, pH 3.0, and 25 °C. Error bars refer to two repetitions.

3.2.2 − Effects of solution pH

The solution pH is a significant factor affecting the catalytic performance of heterogeneous reactions. Thus, an investigation into the effect of different pH conditions (3.0, 7.0, and 10.0) towards CIP oxidation and mineralization was conducted. Complete oxidation of CIP was attained in all studied pH conditions (~100% in 3 h), as seen in FIGURE 3.6; however, a slight increase in the pseudo-first order kinetic constant from acidic to alkaline solutions was observed, as can be seen in TABLE A1.

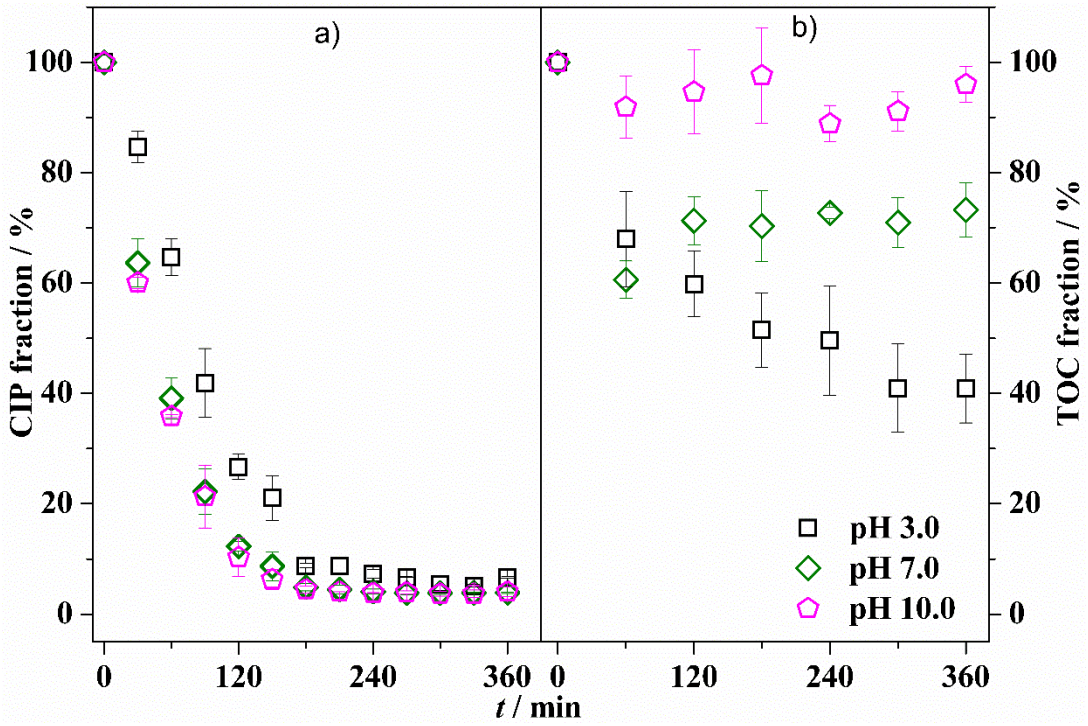

FIGURE 3.6 − Remaining fraction of CIP (CIP fraction) and TOC (TOC fraction) as a function of treatment time (t) at distinct pH values: (□) 3.0; (◇) 7.0; (⬠) 10.0. Conditions: 50 mg L^{-1} CIP, 1.0 g L^{-1} MnOOH, 1.0 g L^{-1} PMS, and 25 °C. Error bars refer to two repetitions.

That behavior can be explained considering *i*) the dependence of the CIP species reactivity with solution pH (*i.e.*, cationic, zwitterion/neutral, or anionic – pK_{a1} and pK_{a2} is equal to 6.09 and 8.62[84], respectively) as reported by

Zhou *et al.*[83] – in that work (only using CIP and PMS), the anionic and zwitterion/neutral species (pH > 7) were more susceptible to PMS (pK_a = 9.4[85]) oxidation due to the higher reactivity of the secondary amine in the piperazine ring – and *ii*) to the fact that at alkaline solutions, $^1O_2$ oxidizing species can be also produced (Eq. 25)[86], leading to a superior oxidation level. Now, taking into account the contribution mediated by the activated PMS with MnOOH, acidic solutions are expected to have an improved performance than at alkaline conditions due to surface charge repulsion (see discussion below). The last process might be more appropriate for similar rates of CIP oxidation (through PMS activation) from acidic to alkaline conditions than the one reported by Zhou *et al.*[83], *i.e.* without PMS activation. It is also important to highlight that any structural modification of CIP can lead to a signal loss during HPLC analyses and, therefore, the amount of oxidant is crucial.

$$HSO_5^- + SO_5^{2-} \rightarrow {}^1O_2 + 2SO_4^{2-} + H^+ \quad (25)$$

An opposite effect was observed during TOC removal, *i.e.*, acidic solutions led to superior mineralization levels and rates, as the type of oxidant (particularly, $SO_4^{\bullet-}$ and $HO^\bullet$ and not $^1O_2$) is essential to convert CIP and its byproducts to CO_2. That behavior can be explained by *i*) the surface charge of MnOOH, since metal oxides/hydroxides show a pH-dependent surface charging and *ii*) reactions mediated by $^1O_2$. As the pH for the point of zero charge (pH_{pzc}) was *ca*. 6.5 (see FIGURE A1), which is consistent with available literature[68], it is expected that when the solution pH was over this value (7.0 and 10.0), the MnOOH surface charge was negative. So, PMS activation by MnOOH might be hindered due to electrostatic repulsion. Likewise, at basic conditions the observed oxidation without significant CO_2 conversion is due to the produced low power $^1O_2$ species (Eq. 25) specially at pH 10[86].

To assess the possible effect of homogeneous reaction mediated by Mn(II) species leaching from the MnOOH compound at acidic conditions, ion chromatography experiments were carried out. As seen in FIGURE A2, high levels (~350 mg L^{-1}) of Mn(II) were detected in the absence of PMS (only MnOOH and MnOOH+CIP – the last is probably due to a redox reaction between Mn(III)/Mn(IV) species with the piperazine group in CIP as described in [68, 87]). When using PMS, independently of the organic compound, low Mn(II) leaching values were measured (~25 mg L^{-1}). On the solid surface, Mn(II) reduces PMS resulting in the formation of $SO_4^{\bullet-}$/$HO^{\bullet}$ and MnO_2 (i.e., Mn(IV) and catalyst deactivation) as already described elsewhere[68, 88, 89]. In solution, the possible formation of unstable Mn(III) from Mn(II) species (Eq. 26 and Eq. 27) can lead to a disproportionation reaction resulting in the formation of low reactive MnO_2 (Eq. 28). The Mn(III) species can also react with PMS (Eq. 29) to produce $SO_5^{\bullet-}$ species and, possibly, $^1O_2$ (Eq. 30)[90].

$$Mn^{2+} + HSO_5^- \rightarrow Mn^{3+} + SO_4^{-\bullet} + OH^- \quad (26)$$

$$Mn^{2+} + SO_4^{-\bullet} \rightarrow Mn^{3+} + SO_4^{2-} \quad (27)$$

$$2Mn^{3+} + 2H_2O \rightarrow Mn^{2+} + MnO_2 + 4H^+ \quad (28)$$

$$Mn^{3+} + HSO_5^- \rightarrow Mn^{2+} + SO_5^{-\bullet} + H^+ \quad (29)$$

$$2SO_5^{-\bullet} + H_2O \rightarrow 2HSO_4^- + 1{,}5\ {}^1O_2 \quad (30)$$

To investigate the possible effect of homogeneous reactions at acidic conditions, experiments were carried out in solutions intentionally contaminated with Mn(II) and without the solid MnOOH catalyst. As seen in FIGURE 3.7, no significant oxidation or mineralization levels for CIP were observed in the presence of Mn(II) species, suggesting a negligible contribution of homogeneous reactions. A similar behavior was observed in the work of Anipsitakis and

Dionysiou[88], in which distinct transition metallic ions (Co(II), Ce(III), Mn(II), Ni(II), Ru(III), and V(III)) were tested for the activation of H_2O_2, PMS (HSO_5^-) and PDS ($S_2O_8^{2-}$). In the case of Mn(II) ions, PMS can be activated leading to trapped sulfate radicals, as represented by Eq. 31.

$$Mn^{2+} + HSO_5^- \rightarrow [Mn^{III}(SO_4^{-\bullet})]^{2+} + OH^- \quad (31)$$

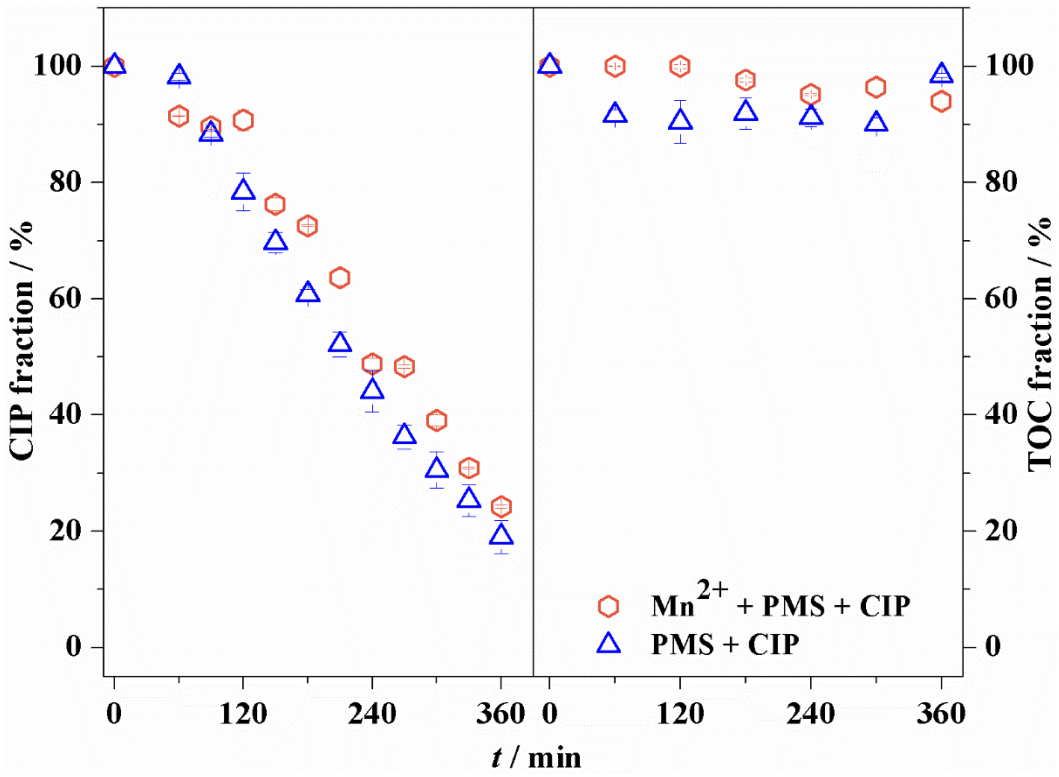

FIGURE 3.7 − Remaining fraction of CIP (CIP fraction) and TOC (TOC fraction) as a function of treatment time (*t*). Effect of homogeneous reactions for oxidation by (△) PMS and (○) Mn^{2+}/PMS system. Conditions: 50 mg L^{-1} CIP, 350 mg L^{-1} Mn^{2+}, 1.0 g L^{-1} PMS, pH 3.0 and 25 °C.

3.2.3 − Effect of PMS and MnOOH concentration

The effects of PMS (1.0 – 4.0 g L^{-1}) and MnOOH (0.5 – 2.0 g L^{-1}) concentration on CIP oxidation and mineralization were investigated, as seen in FIGURE 3.8. As expected, the oxidation levels and rates (see TABLE A2) of CIP were enhanced at increasing concentrations of PMS. However, no significant differences for the CIP mineralization levels and rates were observed. A maximum of ~60% TOC removal was attained after 6 h. That behavior might be caused by the insufficient active sites on the MnOOH surface, which limits the PMS activation. The use of PMS concentrations higher than 1 g L^{-1} can also result in an excess of unreacted oxidant (~30% and ~50% when using 2 and 4 g L^{-1}, respectively, of PMS), as can be seen in FIGURE A3 for the experiments showed in FIGURE 3.8.

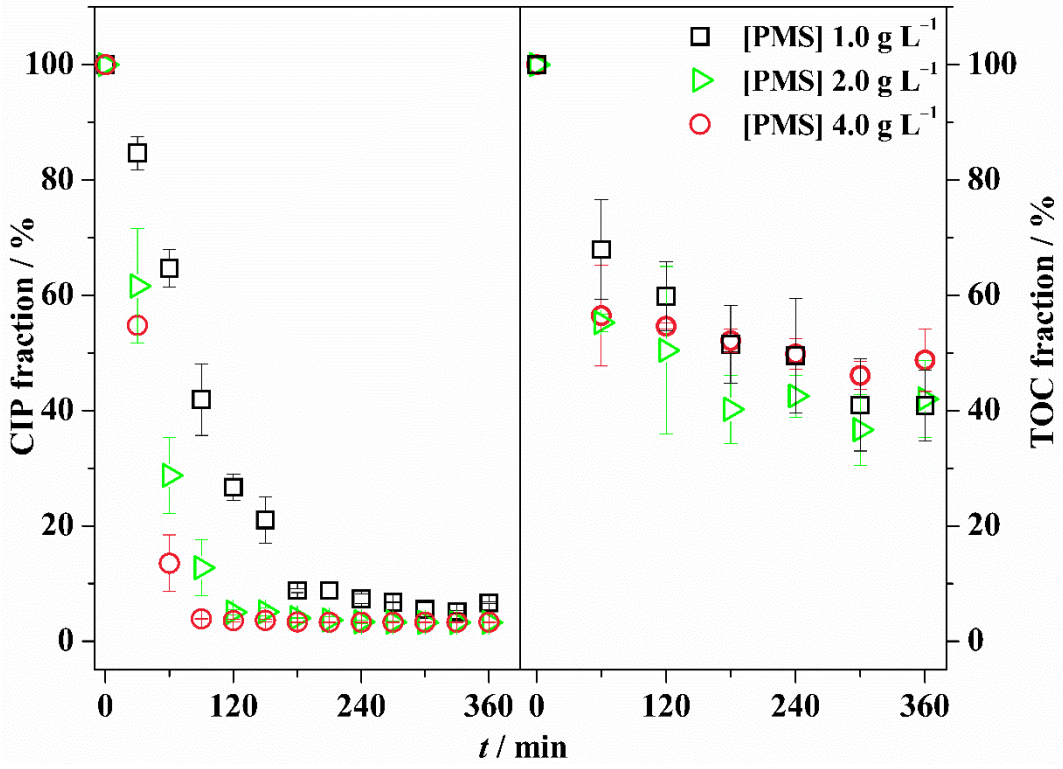

FIGURE 3.8 − Remaining fraction of CIP (CIP fraction) and TOC (TOC fraction) as a function of treatment time (t) at distinct PMS concentration values: (□) 1.0, (▷) 2.0, and (○) 4.0. g L^{-1}. Conditions: 50 mg L^{-1} CIP, 1.0 g L^{-1} MnOOH, pH 3.0, and 25 °C. Error bars refer to two repetitions.

The investigation of MnOOH concentration has not led to any significant oxidation levels and rates of CIP from 0.5 to 2.0 g L^{-1} (see FIGURE 3.9), which confirms the hypothesis that the degradation of CIP is mainly influenced by oxidation with PMS. For TOC removal, a slight increase of 20% was noticed when the MnOOH concentration increased from 0.5 to 1.0 g L^{-1} after 6 h, without further increments at 2.0 g L^{-1}. This result was not expected, since by increasing the amount of catalyst, a higher number of adsorption sites available for PMS activation would be expected. That behavior may be due to the agglomeration of MnOOH particles found in solution, leading to no effective increment in the active area. Similar results were also reported for distinct heterogeneous systems[91, 92].

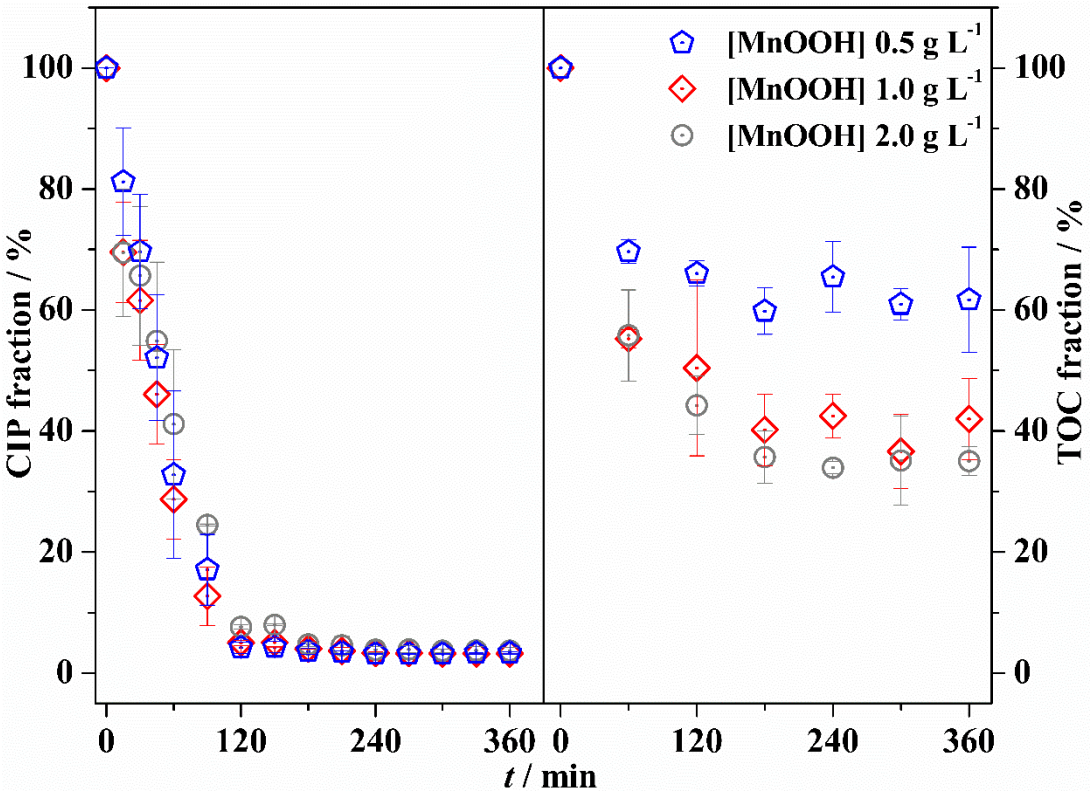

FIGURE 3.9 − Remaining fraction of CIP (CIP fraction) and TOC (TOC fraction) as a function of treatment time (*t*). Effect of MnOOH concentration:(⬠) 0.5 g L^{-1}; (◇) 1.0 g L^{-1}; (⊙) 2.0. g L^{-1}. Conditions: 50 mg L^{-1} CIP, 2.0 g L^{-1} PMS, pH 3.0, and 25 °C. Error bars refer to two repetitions.

Thus, the optimized conditions were acidic solutions (pH 3.0) using 1.0 g L^{-1} of MnOOH and PMS at 25 °C, including TOC removal. The remaining analyzes were carried out at the same conditions.

3.3 − CIP degradation products and pathways: UHPLC-QToF MS and carboxylic acid determinations

For the optimized condition and considering the high levels of conversion to CO_2, only five intermediates were identified (see TABLE A3) for the *m/z* values and FIGURE A4 for the total ion chromatographic profiles) using a UHPLC-QToF MS system (see FIGURE A5) for the MS/MS spectra of intermediates showed in TABLE A3. FIGURE 3.10 shows the proposed degradation route, in which oxidation (probably mediated by $HO^{\bullet}$, $SO_4^{\bullet-}$, and $^1O_2$) is initiated on the side chain of the piperazine group due to its high electron density[93] resulting in products with *m/z* 334.1198, 348.1355, and 362.1147. After successive loss of two formaldehyde groups followed by an amine group, byproducts with *m/z* 306.1258 and 263.0827 were produced, respectively. In the final stages of CIP oxidation, the production of carboxylic acids (mainly formic, acetic, propionic, and adipic acids – see FIGURE A6) clearly indicates the breakdown and oxidation of the aromatic ring as well as the piperazine moiety before complete conversion to CO_2. The presence of F^- ion species was investigated; however, no reliable concentration values were obtained due to interferences in the baseline of the conductivity measurements promoted by the PMS salt precursor.

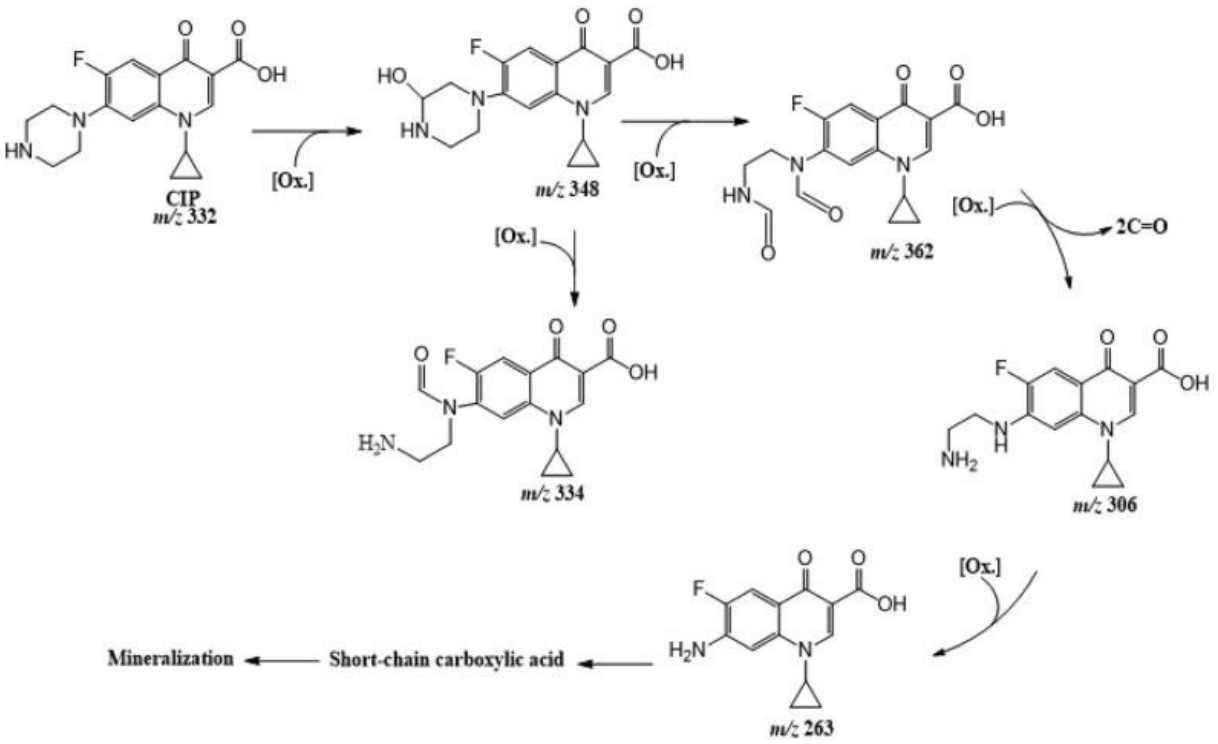

FIGURE 3.10 − Proposed degradation pathways of CIP in the MnOOH/PMS system. Conditions: 50 mg L^{-1} CIP, 1.0 g L^{-1} PMS, 1.0 g L^{-1} MnOOH, pH 3.0, and 25 °C.

3.4 − Identification of the main working oxidants

The ESR spectrum resulting from the reaction of MnOOH, PMS, and DMPO is displayed in FIGURE 3.11. An intense resonance triplet line (1:1:1) was observed from N magnetic dipole moment resulting from two consecutive addition reactions in the adjacent alpha carbon atom. A less intense resonance line split into a 1:2:2:1 was also observed and attributed to the DMPO-OH compound (DMPO-SO_4 is unstable and easily hydrolyzed[94]). The hyperfine constant $a^H = a^N$ = 16.1 G is slightly higher than the more common 14.9 G probably due to the variable ionic strength and solution pH close to 10[95].

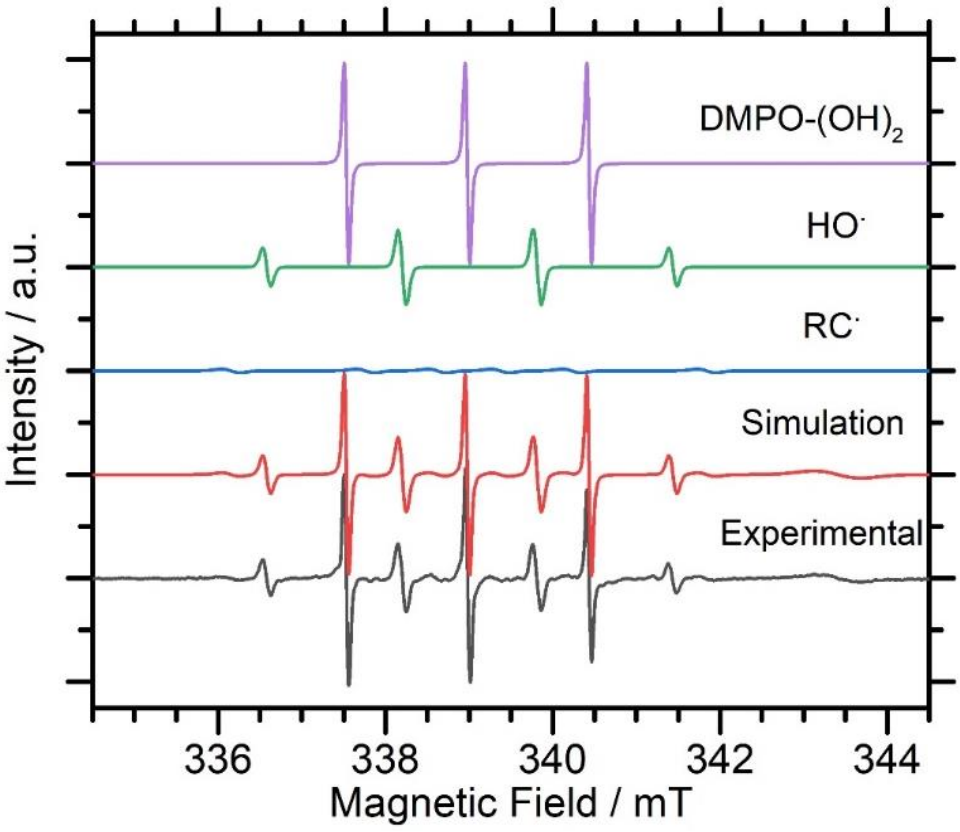

FIGURE 3.11 − Electron spin resonance measurement for the experiment using MnOOH (1.0 g L^{-1}), PMS (1.0 g L^{-1}), DMPO (100 mol L^{-1}) at pH 3. ESR measurement conditions: microwave frequency 9.51334 GHz; field amplitude modulation 1.0 G; frequency modulation 100 kHz; time constant 0.064 s; center field 3395 G; field sweep 100 G; sweep time 60 s; microwave power 20 mW.

The spectra named DMPO-$(OH)_2$ (to simulate the alpha hydrogen abstraction, see the chemical structure in FIGURE A7), $HO^{\bullet}$, and $RC^{\bullet}$ were simulated and combined (see red line). The carbon radical ($RC^{\bullet}$) showed a low intensity signal probably due to the use and manipulation of plastic tips and containers. No signals were observed in the presence of DMPO alone.

To elucidate the main oxidation byproducts resulting from DMPO oxidation new ESR measurements were performed with small field modulation to resolve the superhyperfine splitting. The result suggests that the superhyperfine splitting is compatible with nuclear spin from three equivalent hydrogens of the

CH_3 group and two equivalent hydrogens from two OH groups to unpaired electron on NO fragment indicating the DMPO-$(OH)_2$ adduct (see FIGURE 3.12).

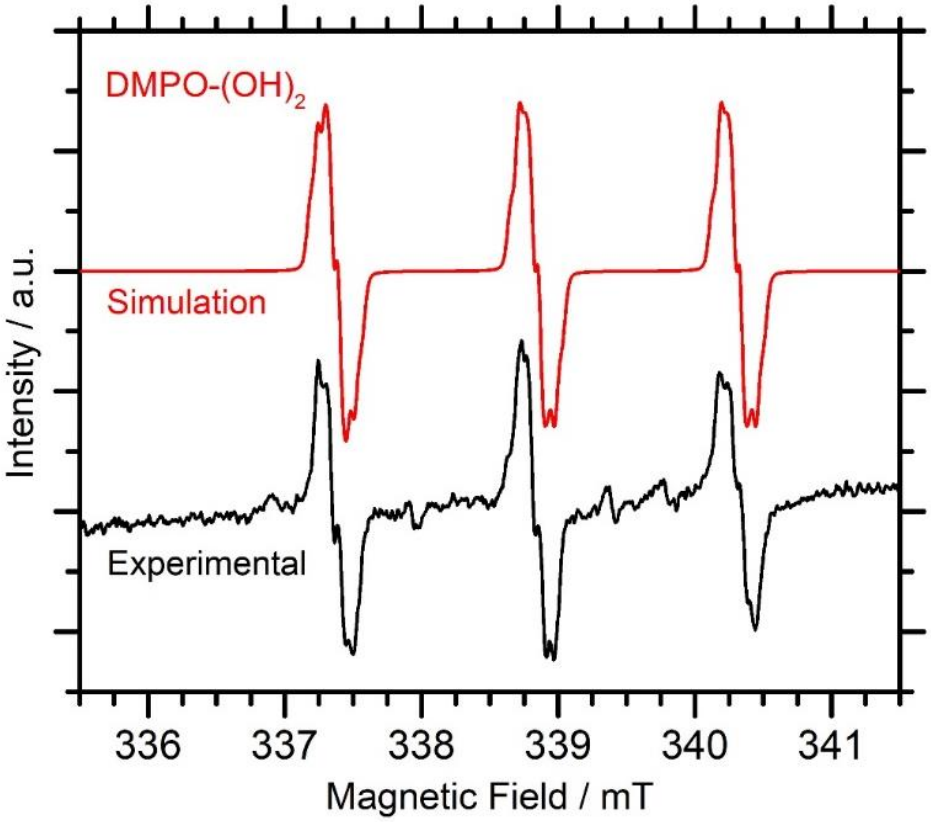

FIGURE 3.12 − Electron spin resonance measurement for the experiment using MnOOH (1.0 g L^{-1}), PMS (1.0 g L^{-1}), DMPO (100 mol L^{-1}) at pH 3. ESR measurement conditions: microwave frequency 9.51334 GHz; field amplitude modulation 0.2 G; frequency modulation 100 kHz; time constant 0.064 s; center field 3395 G; field sweep 100 G; sweep time 60 s; microwave power 20 mW.

The spectrum named DMPO-$(OH)_2$ was measured at appropriate ESR conditions (after 20 min reaction) to detail the superhyperfine splitting and was also properly simulated (see red line). The superhyperfine splitting is compatible with nuclear spin from three equivalent hydrogens of CH_3 group and two equivalent hydrogens from two OH groups. (a^N = 14.9 G, a^{CH3} = 0.52 G, and $a^{(OH)2}$ = 0.90 G). See the reaction in FIGURE A7.

To confirm the latter possibility, UHPLC-QToF MS measurements were also carried out as previously described. As can be seen in the extracted ion chromatogram of FIGURE A8 and in the MS/MS spectra of FIGURE A9, DMPO-OH (*m/z* 130.0860) and DMPO$(OH)_2$ (*m/z* 148.0966) compounds were detected. The proposed fragmentation route for each compound is depicted in FIGURE A10, in agreement with studies of Domingues *et al.*[96], Guo *et al.*[97], and Pavlovic & Hopke[98]. Thus, the triplet signal results from two consecutive addition reactions involving $HO^{\bullet}$ radicals. For the experiments using TEMP, the results were not conclusive as the characteristic triplet (1:1:1) was observed in the control experiment using PMS (1.0 g L^{-1}). Hence, only small modifications were observed when using MnOOH and PMS (see the characteristic triplet signals in FIGURE A11).

3.5 − Time evolution of MnOOH: morphological, structural, and electrical analyses

To investigate and understand the morphological, structural, and electric changes taking place in the MnOOH catalyst during the CIP degradation in the presence of PMS, XPS, TEM, cyclic voltammetry, electrochemical impedance, and Mn average oxidation state analyses were carried out before (as-prepared MnOOH) and after 3 h (3-MnOOH) and 6 h (6-MnOOH) of treatment in the optimized conditions.

The deconvoluted high-resolution XPS C 1s spectra for the MnOOH at distinct conditions (as-prepared and after 3 and 6 h of treatment) are displayed in FIGURE 3.13. As mentioned above, the assigned carbon functional groups are typical for surface contamination, as the technique probes about 5 nm thick surface layer. For the 6 h sample, $–CO_3$/$–CO_2$ and $–CF_2$/$–CF_3$ termination groups appear at 289.9 eV and 292.1 eV, respectively. The presence of fluorine groups, also identified by the appearance of the F 1s signal (~0.3 at% for the 6-MnOOH

and 0.2 at% for the 3-MnOOH) at ~689 eV (not shown) is interesting and may indicate a direct electron transfer from MnOOH to the CIP molecule through the piperazine moiety. That behavior is corroborated by the *i*) presence of Mn(II) species detected in the treating solution which might be produced through electron transfer reactions between the piperazine moiety of CIP and MnOOH – see Kamagate *et. al.*[68] and Zhang, H. & Huang, C. H.[87] for more details and *ii*) adsorption/oxidation of CIP using MnOOH without oxidant – see FIGURE 3.5a.

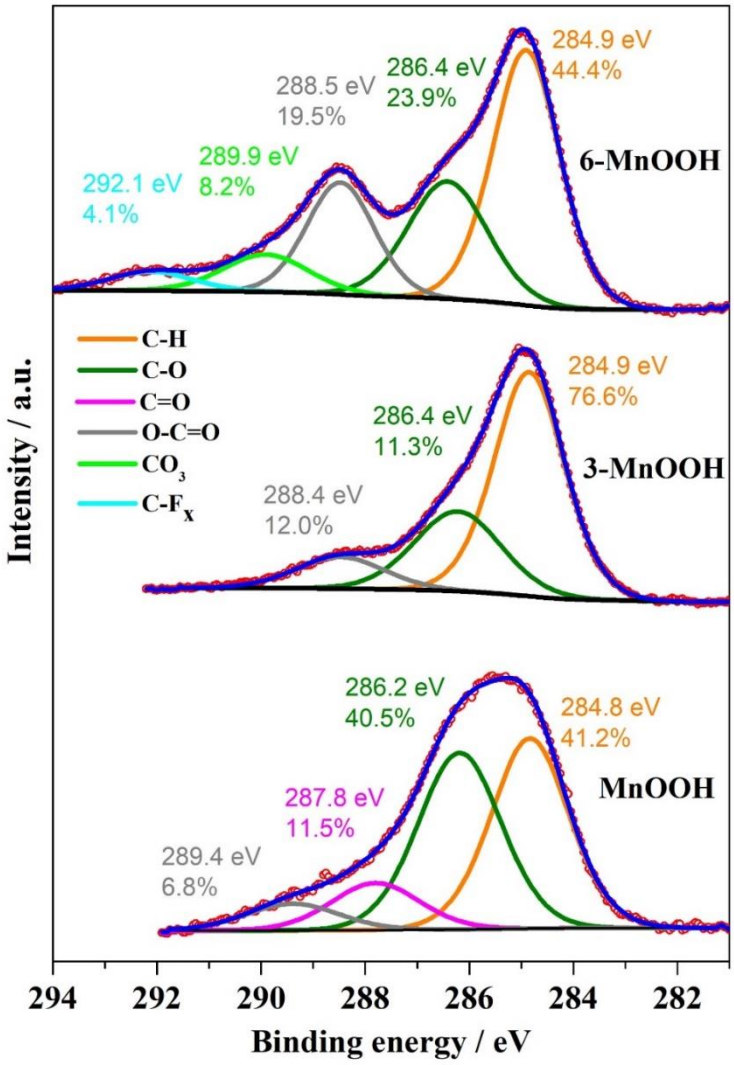

FIGURE 3.13 − High-resolution XPS spectra of C 1s for MnOOH at distinct conditions: as-prepared (MnOOH) and after 3 h (3-MnOOH) and 6 h (6-MnOOH) of treatment. Experimental conditions: 50 mg L^{-1} CIP, 1.0 g L^{-1} MnOOH, 1.0 g L^{-1} PMS, pH 3.0, and 25 °C

The main components of the O 1s spectra at 529.5 eV and 530.8 eV are related to O–Mn bonds (O^{-2} species) and hydroxylic groups on the oxide/hydroxide surface, respectively (see FIGURE 3.14). In addition, there are contributions of oxygenated groups resulting from contamination by hydrocarbons (O–C at ~532.1 eV and O–C=O at ~533.1 eV), previously identified in the C 1s spectra. For the 6-MnOOH sample, a $–CO_3$ type termination at 531.8 eV and a high binding energy component (534.6 eV) were attributed to molecular H_2O.

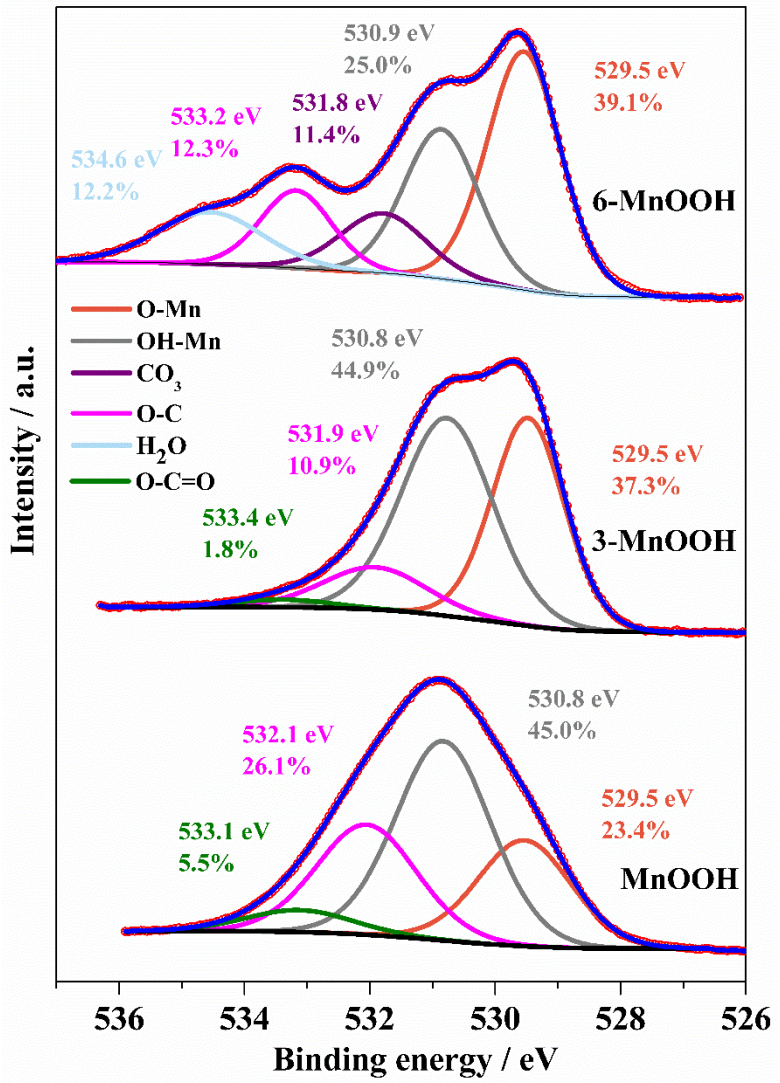

FIGURE 3.14 − High-resolution XPS spectra of O 1s for MnOOH at distinct conditions: as-prepared (MnOOH), after 3 h (3-MnOOH), and 6 h (6-MnOOH) of treatment. Conditions: 50 mg L^{-1} CIP, 1.0 g L^{-1} MnOOH, 1.0 g L^{-1} PMS, pH 3.0, and 25 °C).

Some important features can be extracted from the XPS C 1s an O 1s spectra for different collection times: *i*) a significant increase of the peak area related to the O–Mn bonds, from 23.4% (as-prepared) to 37.3% (3 h) and 39.1% (6 h), *ii*) subsequently a decrease of the HO–Mn components, from 45.0% (as-prepared) to 44.9% (3 h) and 25.0% (6 h), and *iii*) appearance of new intensities after 6 h treatment, related to $–CO_3$ and $–CF_2$/$–CF_3$ terminations. These findings suggest that MnOOH is oxidized to higher oxidation states (inactivation process), possibly supplying electrons to the oxidant (main process), and activating both PMS and the CIP molecule. As a result of the MnOOH inactivation, an outside-in conversion reaction may take place, that is, forming a core-shell compound of Mn(III) covered by an oxide layer of higher oxidation states after 6 h of treatment. This finding is supported by the observed decrease in the TOC removal rate and cessation of oxidant consumption after ~3 h, as shown below. The inactivation is probably caused by the thickening of the oxide layer that hinders the electron transfer to PMS (see discussion below). Moreover, the $–CF_2$/$–CF_3$ termination seems to confirm a direct electron transfer from MnOOH to CIP after a first phase of the adsorption process (see red circle in FIGURE 3.5a).

To obtain more information on the inactivation process, Mn $2p_{3/2}$ spectra were fitted with 4 and 5 components corresponding to different oxidation states of Mn (see FIGURE 3.15). For the as-prepared sample, the predominant intensity is related to MnOOH (or Mn_2O_3) at 642.1 eV with 44.6% peak area, followed by MnO_2 at 643.5 eV (23.4%), MnO at 640.7 eV (22.9%), and MnO_3 at 645.0 eV (9.1%). For the 3-MnOOH sample, initially a partial reduction process takes place increasing the fraction of the MnO phase, probably due to the initial leaching of Mn(III) ions. However, the 6-MnOOH sample shows an increase of the oxidation on the sample surface after 6 h. The intensity of the MnO_3 oxidation state increases on the expense of MnOOH, accompanied by the appearance of a new intensity at 536.6 eV attributed to the Mn_2O_7 phase. These results are

consistent with O 1s data, and find evidence of a significant decrease of the MnOOH phase (44.6–23.4%) during CIP degradation.

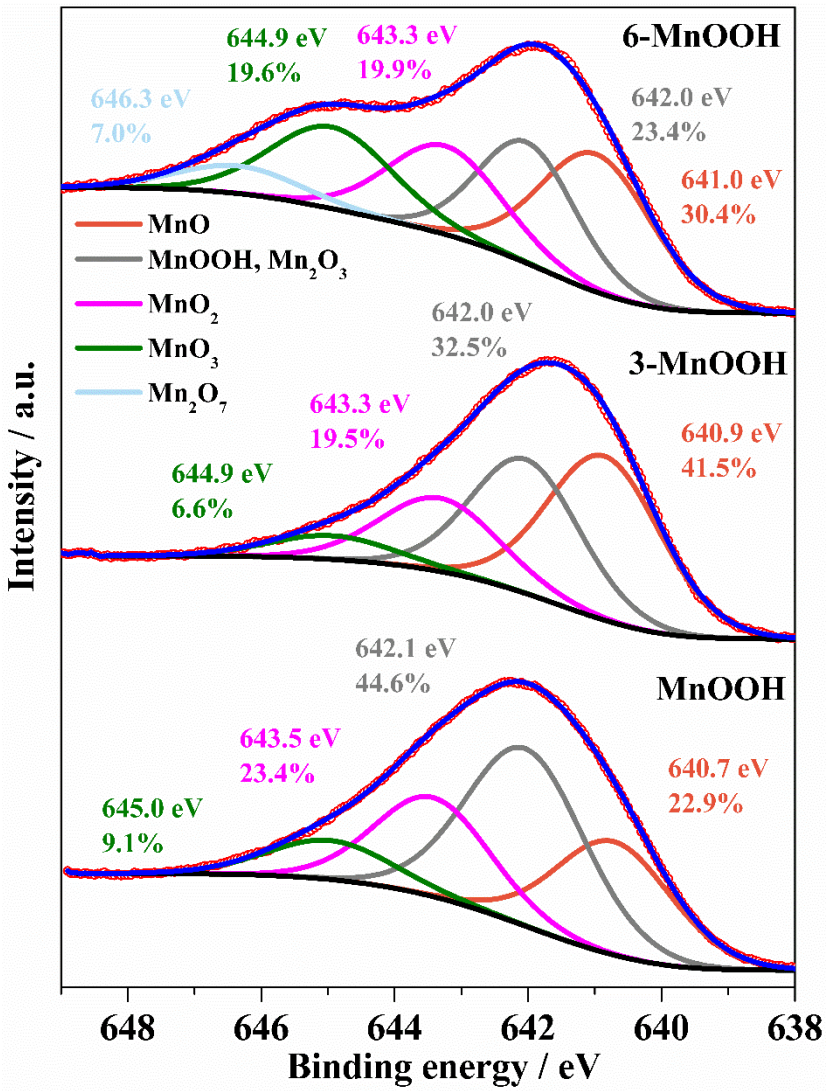

FIGURE 3.15 − High-resolution XPS spectra of Mn $2p_{3/2}$ for MnOOH at distinct conditions: as-prepared (MnOOH), after 3 h (3-MnOOH), and 6 h (6-MnOOH) of treatment. Conditions: 50 mg L^{-1} CIP, 1.0 g L^{-1} MnOOH, 1.0 g L^{-1} PMS, pH 3.0, and 25 °C).

To further understand the evolution of Mn average oxidation state potentiometric titration experiments were carried out. As shown in TABLE A4, the average oxidation state of Mn in the as-prepared sample increased from 3.02 to 3.26 after 3 h and then to 3.36 after 6 h of treatment. The result confirms that

Mn(II) in the MnOOH compound is being gradually oxidized to Mn(IV) species and transferring electrons to CIP, but mainly to PMS. Such structural transformation was not confirmed by XRD whose diffraction pattern remained close to that of the as-prepared MnOOH (FIGURE 3.16).

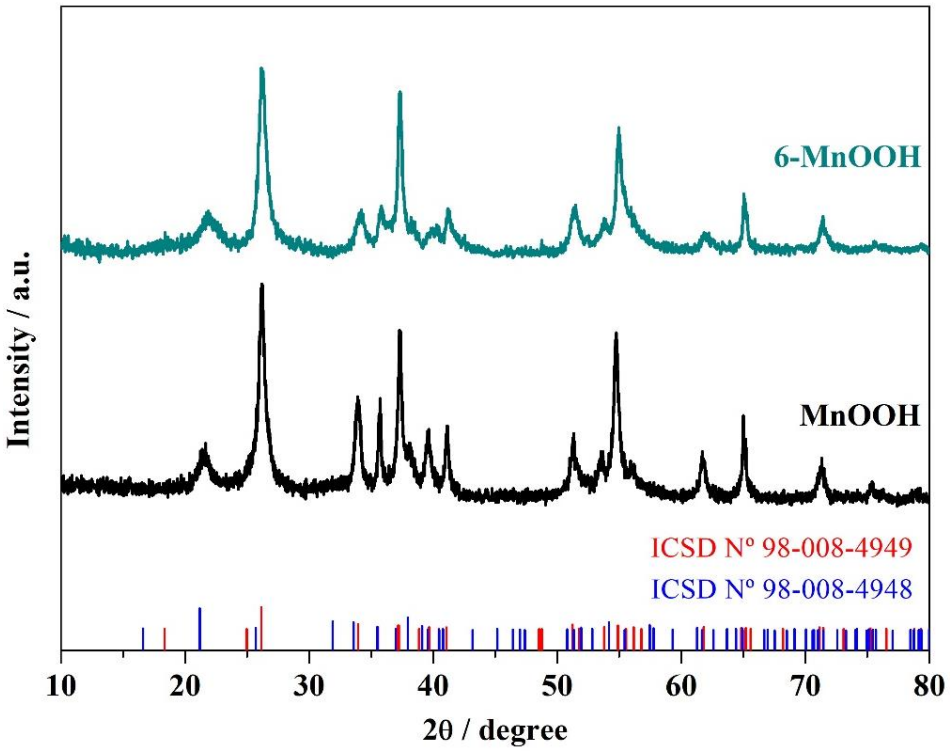

FIGURE 3.16 − X-ray diffraction (XRD) patterns for distinct conditions: as-prepared (MnOOH) and after 6 h (6-MnOOH) of treatment (experimental conditions: 50 mg L^{-1} CIP, 1.0 g L^{-1} MnOOH, 1.0 g L^{-1} PMS, pH 3.0, and 25 °C). Note: most peaks were in accordance with the ICSD card Nº 98-008-4949 (Manganite), expect the diffraction peak at ~20º. This last seems to refer to another crystalline phase of MnOOH (ICSD Nº 98-008-4948: Groutite).

However, upon visual inspection of the assayed MnOOH compound, it can be readily attested that a color change from brown to black occurred (FIGURE 3.17).

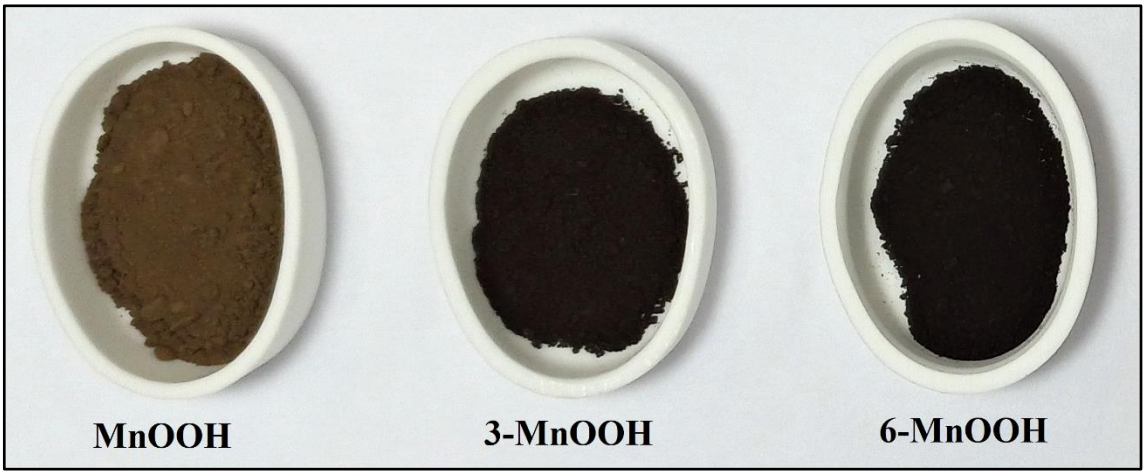

FIGURE 3.17 − Images of MnOOH powders at distinct conditions: as-prepared (MnOOH), after 3 h (3-MnOOH), and 6 h (6-MnOOH) of treatment.

HRTEM images of the as-prepared and 3-MnOOH confirm the appearance of an amorphous phase (shell) in the outer region of the MnOOH as seen in FIGURE 3.18a, in contrast to a crystalline region in the inner part of the particle. Note that such structure, *i.e.*, core-shell, was not observed in the as-prepared MnOOH (see the aligned fringes throughout the particle of FIGURE 3.18b).

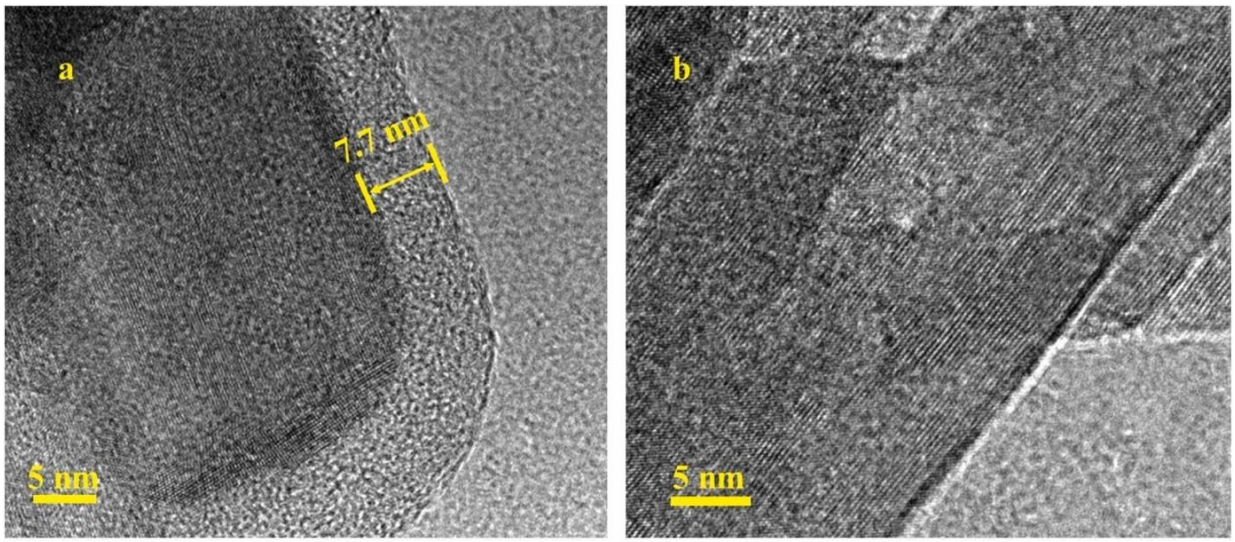

FIGURE 3.18 − High-resolution TEM (HRTEM) for MnOOH at distinct conditions: **a)** after 3 h (3-MnOOH) of treatment and **b)** as-prepared (MnOOH). Conditions: 50 mg L^{-1} CIP, 1.0 g L^{-1} MnOOH, 1.0 g L^{-1} PMS, pH 3.0, and 25 °C.

CV measurements (20 mV s^{-1} and 2nd scan) for the 3-MnOOH, 6-MnOOH, and as-prepared are shown in FIGURE 3.19. The electrochemical profile of the as-prepared sample is characterized by a capacitive behavior without clear oxidation and reduction peaks. That behavior is different from the one of 3-MnOOH and 6-MnOOH samples, in which an oxidation (0.98 V *vs.* Ag/AgCl/KCl (3 mol L^{-1})) and reduction (0.81 V *vs.* Ag/AgCl/KCl (3 mol L^{-1})) peaks (Mn(III) to Mn(IV) with Na^+ ion intercalation) can be clearly seen due to the produced MnO_2 from reaction with PMS oxidant.

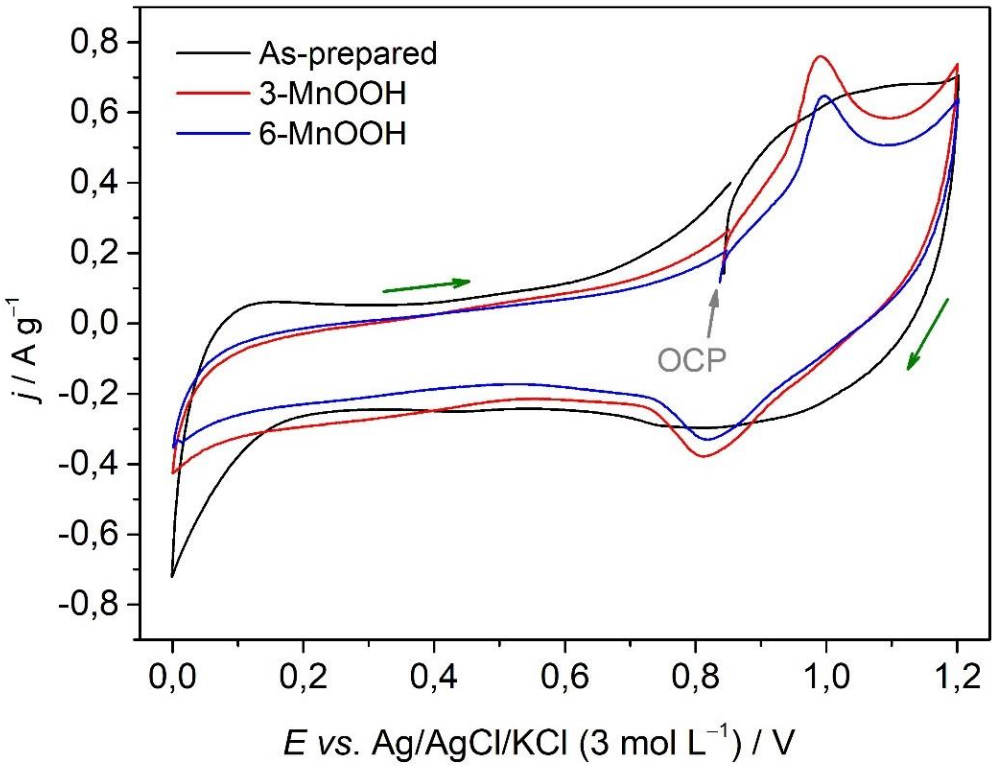

FIGURE 3.19 − Cyclic voltammetry (20 mV s^{-1} and 2nd scan) measurements of the as-prepared MnOOH and after 3 (3-MnOOH) and 6 h (6-MnOOH) of treatment. The potential scan started from OCP (open circuit potential – 1 h rest before measurement). A 0.1 mol L^{-1} Na_2SO4 (pH 3) solution at ambient conditions was used. The green arrows indicate the scan direction.

The electrochemical impedance of those samples is displayed in FIGURE 3.20. The equivalent circuit used to obtain the best fits of the experimental data was composed of the solution resistance (R_{sol}), carbon material charge transfer resistance (R_C), and the oxide charge transfer resistance (R_{oxide}) at high and medium to low frequencies, respectively. The constant phase elements CPE_C are in parallel with the R_C element and CPE_{Oxide} with the double layer from the oxide material at medium to low frequencies, respectively.

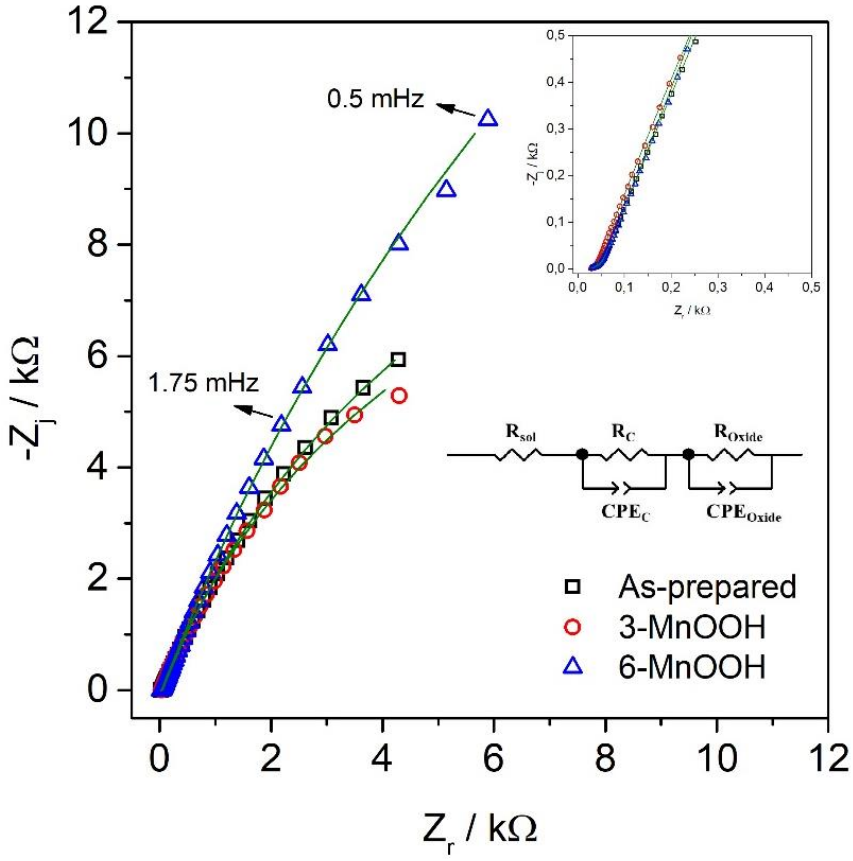

FIGURE 3.20 - Complex plane for the MnOOH samples in the as-prepared condition and after 3 (3-MnOOH) and 6 h (6-MnOOH) of treatment. The equivalent circuit used to fit data generated (see continuous line) by electrochemical impedance is shown in the inset. A 0.1 mol L^{-1} Na_2SO_4 (pH 3) solution at ambient conditions was used.

The time evolution of the R_{oxide} for the as-prepared, 3-MnOOH, and 6-MnOOH shows in FIGURE A12 a resistance increase from $2.9 \pm 1.0 \times 10^4$ Ω (as-prepared) to $6.8 \pm 2.7 \times 10^4$ Ω (6 h), during PMS activation mediated by MnOOH, hindering further oxidant activation. This is also seen by the increase of the impedance modulus when comparing the 6-MnOOH with the as-prepared sample (FIGURE 3.21).

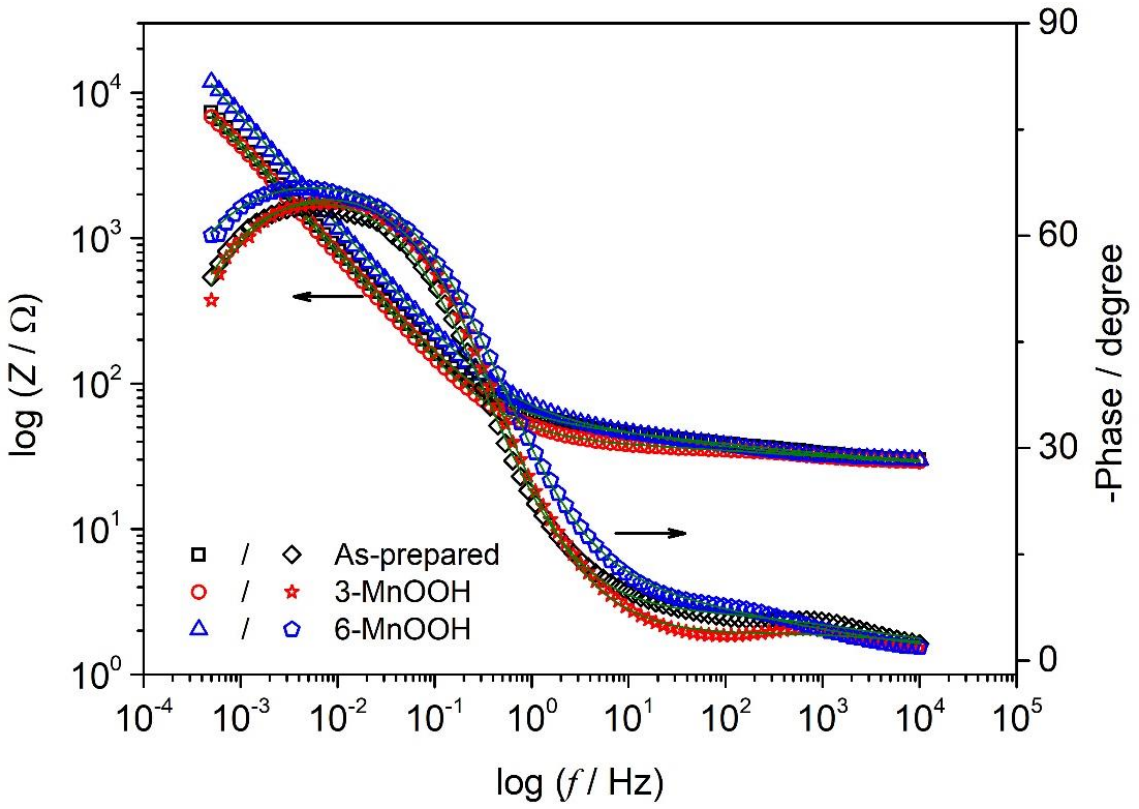

FIGURE 3.21 − Bode plots for the MnOOH samples in the as-prepared condition and after 3 (3-MnOOH) and 6 h (6-MnOOH) of treatment. A 0.1 mol L^{-1} Na_2SO_4 (pH 3) solution at ambient conditions was used.

Taking into account the *post mortem* analyses, a decrease in the efficiency of the MnOOH/MnO_2 compound during the recycling test would be expected. However, from the second until the fifth run, the oxidation of CIP remained close to the results of the as-prepared material, as seen in FIGURE 3.22.

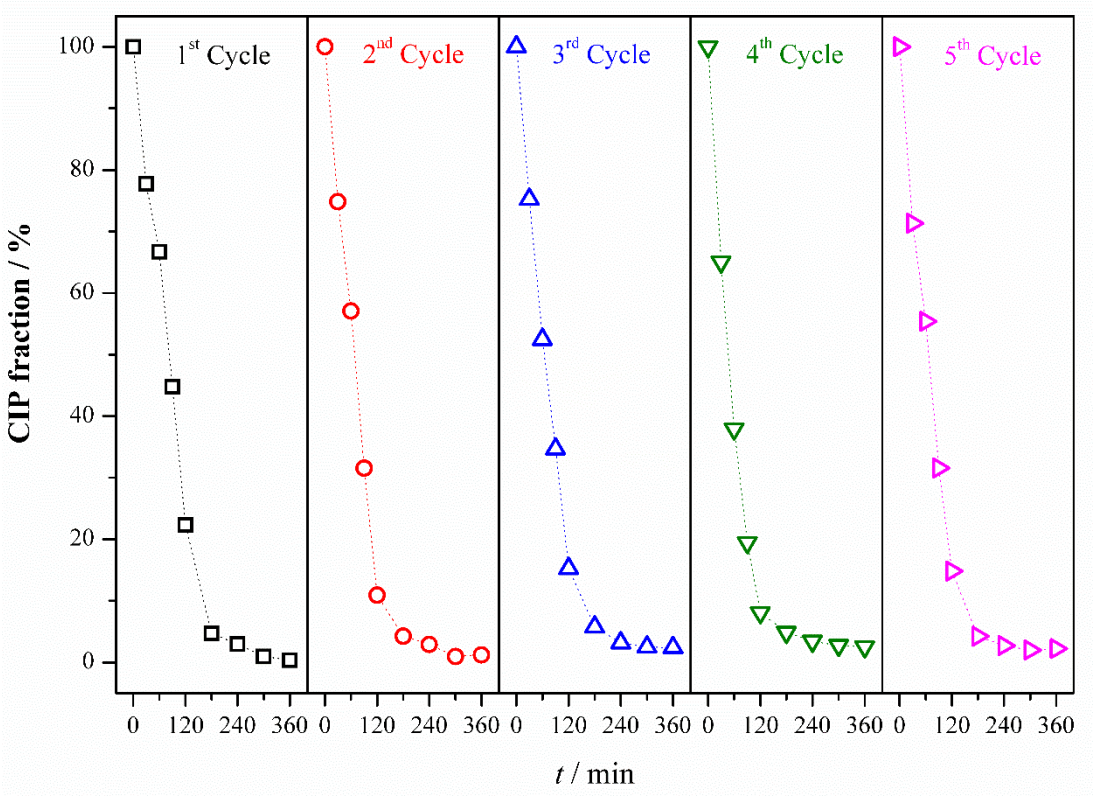

FIGURE 3.22 - Remaining fraction of CIP (CIP fraction) as a function of treatment time (*t*) for five consecutive experiments. The oxide material was vacuum filtered and dried before use. Experimental conditions: 50 mg L^{-1} CIP, 1.0 g L^{-1} MnOOH, pH 3.0, and 25 °C.

During such experiments and after adding PMS, the black MnOOH/MnO_2 composite turned to the brown color, similar to the as-prepared material. As discussed in detail in the work of Li *et al.* [99], this might indicate that Mn(IV) was reduced by adsorbed PMS to Mn(III) whose degree will certainly depend on the PMS concentration and oxide termination groups. Further studies will be carried out to understand that behavior.

4 − CONCLUSIONS

Nanometric MnOOH oxyhydroxide was successfully synthesized to activate peroxymonosulfate (PMS) oxidant under acidic conditions. In the optimized experimental condition, within 3 h a complete oxidation of CIP antibiotic with more than 60% mineralization within 6 h was attained, without contributions from homogeneous reactions (i.e., Mn(II) species). A low number and intensity of intermediate compounds were detected by UHPLC-QToF MS due to the high oxidizing conditions leading to the production of carboxylic acid and inorganic ions. The latter specie was only detected by XPS on the surface of MnOOH after 6 h treatment. Thus, the CIP molecule might be oxidized through *i*) PMS activation promoted by MnOOH resulting in $HO^{\bullet}$ radicals and, to a minor extent, *ii*) directly on the MnOOH surface through direct electron transfer. The preceding result was confirmed by ESR measurements and structural changes that took place on the MnOOH surface, i.e., an increase of the oxidation state of Mn oxides at the expense of MnOOH, as evidenced by XPS and potentiometric titration. The Mn oxidation led to the formation of an amorphous shell structure of MnO_2 and MnO_3 over the MnOOH crystallites with the subsequent increase of the charge transfer resistance that hindered the electron transfer to the PMS oxidant or CIP byproducts. Apparently, these behaviors seem to be recovered when using a freshly prepared PMS solution. These findings may shed light on the synthesis of improved/engineered compounds to activate oxidants.

5 − REFERENCES

1. GETIRANA, A., LIBONATI, R. & CATALDI, M. "Brazil is in water crisis — it needs a drought plan". Nature, **600**: 218, 2021.

2. TZANAKAKIS, V. A., PARANYCHIANAKIS, N. V. & ANGELAKIS, A. N. "Water Supply and Water Scarcity". Water, **12**: 2347, 2020.

3. SARAVANAN, A., SENTHIL KUMAR, P., JEEVANANTHAM, S., KARISHMA, S., TAJSABREEN, B., YAASHIKAA, P.R., RESHMA, B. "Effective water/wastewater treatment methodologies for toxic pollutants removal: Processes and applications towards sustainable development". Chemosphere **280**: 2021.

4. WHO & UNICEF − Progress on household drinking water, sanitation and hygiene, 2000 – 2017. Special focus on inequalities, 2019.

5. SISTEMA NACIONAL DE INFORMAÇÕES SOBRE SANEAMENTO − Diagnóstico temático serviços de água e esgoto - visão geral ano de referência 2020. Brazil, 2021.

6. UNITED NATIONS − The sustainable development goal report 2022. Annual report, 2022.

7. RICHARDSON, S. D. & TERNES, T. A. "Water Analysis: Emerging Contaminants and Current Issues". Anal. Chem. **90**: 398, 2018.

8. MANZETTI, S., VAN DER SPOEL, E. R. & VAN DER SPOEL, D. "Chemical properties, environmental fate, and degradation of seven classes of pollutants". Chem. Res. Toxicol. **27**: 713, 2014.

9. LE COADOU, L., LE MÉNACH, K., LABADIE, P., DÉVIER, M.-H., PARDON, P., AUGAGNEUR, S. & BUDZINSKI, H. "Quality survey of natural mineral water and spring water sold in France: Monitoring of hormones, pharmaceuticals, pesticides, perfluoroalkyl substances,

phthalates, and alkylphenols at the ultra-trace level". Sci. Total Environ. **603**–**604**: 651, 2017.

10. CHOW, S. J., OJEDA, N., JACANGELO, J. G. & SCHWAB, K. J. "Detection of ultrashort-chain and other per- and polyfluoroalkyl substances (PFAS) in U.S. bottled water". Water Res. **201:** 2021.

11. MONTAGNER, C. C., SODRÉ, F. F., ACAYABA R. D., VIDAL, C., CAMPESTRINI, I., LOCATELLI, M. A., PESCARA, I. C., ALBUQUERQUE, A. F., UMBUZEIRO, G. A. & JARDIM, W. F. "Ten Years-Snapshot of the Occurrence of Emerging Contaminants in Drinking, Surface and Ground Waters and Wastewaters from São Paulo State, Brazil". J. Braz. Chem. Soc. **30**: 614, 2018.

12. BORRULL, J., COLOM, A., FABREGAS, J., POCURULL, E. & BORRULL, F. "A liquid chromatography tandem mass spectrometry method for determining 18 per- and polyfluoroalkyl substances in source and treated drinking water". J. Chromatogr. A. **1629**: 2020.

13. TRIASSI, M., MONTUORI, P., PROVVISIERO, D. P., DE ROSA, E., DI DUCA, F., SARNACCHIARO, P. & DÍEZ, S. "Occurrence and spatial-temporal distribution of atrazine and its metabolites in the aquatic environment of the Volturno River estuary, southern Italy". Sci. Total Environ. **803**: 2022.

14. WAN, Y., TRAN, T. M., NGUYEN, T. V., WANG, A., WANG, J. & KANNAN, K. "Neonicotinoids, fipronil, chlorpyrifos, carbendazim, chlorotriazines, chlorophenoxy herbicides, bentazon, and selected pesticide transformation products in surface water and drinking water from northern Vietnam". Sci. Total Environ. **750**: 2021.

15. ZOU, M., TIAN, W., ZHAO, J., CHU, M. & SONG, T. "Quinolone antibiotics in sewage treatment plants with activated sludge treatment

processes: A review on source, concentration and removal". Process Saf. Environ. Prot. **160**: 116, 2022.

16. DINH, Q. T, MOREAU-GUIGON, E., LABADIE, P., ALLIOT, F., TEIL, M. J., E BLANCHARD, M. & CHEVREUIL, M. "Occurrence of antibiotics in rural catchments". Chemosphere **168:** 483, 2017.

17. KAIRIGO, P., NGUMBA, E., SUNDBERG, L.-R., GACHANJA, A. & TUHKANEN, T. "Occurrence of antibiotics and risk of antibiotic resistance evolution in selected Kenyan wastewaters, surface waters and sediments". Sci. Total Environ. **720**: 2020.

18. MONTEIRO, M. A., SPISSO, B. F., FERREIRA, R. G., PEREIRA, M. U., GRUTES, J. V., DE ANDRADE, B. R. & D'AVILA, L. A. "Development and Validation of Liquid Chromatography-Tandem Mass Spectrometry Methods for Determination of Beta-Lactams, Macrolides, Fluoroquinolones, Sulfonamides and Tetracyclines in Surface and Drinking Water from Rio de Janeiro, Brazil". J. Braz. Chem. Soc. **29**: 801, 2017.

19. RAMÍREZ-MORALES, D., MASÍS-MORA, M., MONTIEL-MORA, J. R., CAMBRONERO-HEINRICHS, J. C., BRICEÑO-GUEVARA, S., ROJAS-SÁNCHEZ, C. E., MÉNDEZ-RIVERA, M., ARIAS-MORA, V., TORMO-BUDOWSKI, R., BRENES-ALFARO, L. & RODRÍGUEZ-RODRÍGUEZ, C. E. "Occurrence of pharmaceuticals, hazard assessment and ecotoxicological evaluation of wastewater treatment plants in Costa Rica". Sci. Total Environ. **746**: 2020.

20. KAFAEI, R., PAPARI, F., SEYEDABADI, M., SAHEBI, S., TAHMASEBI, R., AHMADI, M., SORIAL, G. A., ASGARI, G. & RAMAVANDI, B. "Occurrence, distribution, and potential sources of antibiotics pollution in the water-sediment of the northern coastline of the Persian Gulf, Iran". Sci. Total Environ. **627**: 703, 2018.

21. LI, S., SHI, W., WEI LIU, W., LI, H., ZHANG, W., HU, J., KE, Y., SUN, W. & NI, J. "A duodecennial national synthesis of antibiotics in China's major rivers and seas (2005–2016)". Sci. Total Environ. **615**: 906, 2018.

22. BOTERO-COY, A. M., MARTÍNEZ-PACHÓN, D., BOIX, C., RINCÓN, R. J., CASTILLO, N., ARIAS-MARÍN, L. P., MANRIQUE-LOSADA, L., TORRES-PALMA, R., MONCAYO-LASSO, A. & HERNÁNDEZ, F. "An investigation into the occurrence and removal of pharmaceuticals in Colombian wastewater". Sci. Total Environ. **642**: 842, 2018.

23. LESSER, L. E., MORA, A., MOREAU, C., MAHLKNECHT, J., HERNÁNDEZ-ANTONIO, A., RAMÍREZ, A. I. & BARRIOS-PIÑA, H. "Survey of 218 organic contaminants in groundwater derived from the world's largest untreated wastewater irrigation system: Mezquital Valley, Mexico". Chemosphere. **198**: 510, 2018.

24. FERNANDES, M. J., PAÍGA, P., SILVA, A., LLAGUNO, C. P., CARVALHO, M., VÁZQUEZ, F. M. & DELERUE-MATOS, C. "Antibiotics and antidepressants occurrence in surface waters and sediments collected in the north of Portugal". Chemosphere. **239**: 2020.

25. ÖSTMAN, M., LINDBERG, R. H., FICK, J., BJÖRN, E. & TYSKLIND, M. "Screening of biocides, metals and antibiotics in Swedish sewage sludge and wastewater". Water Res. **115**: 318, 2017.

26. ZHANG, G., LU, S., WANG, Y., LIU, X., LIU, Y., XU, J., ZHANG, T., WANG, Z. & YANG, Y. "Occurrence of antibiotics and antibiotic resistance genes and their correlations in lower Yangtze River, China". Environ. Pollut. **257**:, 2020.

27. YAO, L., WANG, Y., TONG, L., DENG, Y., LI, Y., GAN, Y., GUO, W., DONG, C., DUAN, Y. & ZHAO, K. "Occurrence and risk assessment of antibiotics in surface water and groundwater from different depths of

aquifers: A case study at Jianghan Plain, central China". Ecotoxicol. Environ. Saf. **135**: 236, 2017.

28. LUNGU, I. A., MOLDOVAN, O. L., BIRIȘ, V. & RUSU, A. "Fluoroquinolones Hybrid Molecules as Promising Antibacterial Agents in the Fight against Antibacterial Resistance". Pharmaceutics **14**: 1749, 2022.

29. BILA, D. M. & DEZOTTI, M. "Desreguladores endócrinos no meio ambiente: efeitos e conseqüências". Quim. Nova. **30**: 651, 2007.

30. BIEL-MAESO, M., CORADA-FERNÁNDEZ, C. & LARA-MARTÍN, P. A. "Removal of personal care products (PCPs) in wastewater and sludge treatment and their occurrence in receiving soils". Water Res. **150**: 129, 2019.

31. GUO, W.; PAN, B.; SAKKIAH, S.; YAVAS, G.; GE, W.; ZOU, W.; TONG, W. & HONG, H. "Persistent Organic Pollutants in Food: Contamination Sources, Health Effects and Detection Methods". Int. J. Environ. Res. Public Health. **16**: 4361, 2019.

32. BEN, Y., FU, C., HU, M., LIU, L., WONG, M. H. & ZHENG, C. "Human health risk assessment of antibiotic resistance associated with antibiotic residues in the environment: A review". Environ. Res. **169**: 483, 2019.

33. UNITED NATIONS ENVIRONMENT PROGRAMME − Environmental Dimensions of Antimicrobial Resistance: Summary for Policymakers. 2022.

34. WORLD HEALTH ORGANIZATION − Global antimicrobial resistance and use surveillance system (GLASS) report 2022. 2022.

35. MIKLOS, D. B., REMY, C., JEKEL, M., LINDEN, K. G., DREWES, J. E. & HÜBNER, U. "Evaluation of advanced oxidation processes for water and wastewater treatment – A critical review". Water Res. **139**: 118, 2018.

36. BABUPONNUSAMI, A. & MUTHUKUMAR, K. "A review on Fenton and improvements to the Fenton process for wastewater treatment". J. Environ. Chem. Eng. **2**: 557, 2014.

37. OLMEZ-HANCI, T. & ARSLAN-ALATON, I. " Comparison of sulfate and hydroxyl radical based advanced oxidation of phenol" Chem. Eng. J. **224:** 10, 2013.

38. WANG, X., JING, J., ZHOU, M. & DEWIL, R. "Recent advances in H_2O_2-based advanced oxidation processes for removal of antibiotics from wastewater". Chinese Chem. Lett. **34**: 2023.

39. PIGNATELLO, J. J. "Dark and photoassisted iron(3+)-catalyzed degradation of chlorophenoxy herbicides by hydrogen peroxide" Environ. Sci. Technol. **26**: 944, 1992.

40. CHEN, J., XU, J. & SHING, C. "Decomposition rate of hydrogen peroxide bleaching agents under various chemical and physical conditions". J. Prosthet. Dent. **69**: 46, 1993.

41. OH, W. D., DONG, Z. & LIM, T. T. "Generation of sulfate radical through heterogeneous catalysis for organic contaminants removal: Current development, challenges and prospects". Appl. Catal. B Environ. **194**: 169, 2016.

42. GUERRA-RODRÍGUEZ, S., RODRÍGUEZ, E., SINGH, D. & RODRÍGUEZ-CHUECA, J. "Assessment of Sulfate Radical-Based Advanced Oxidation Processes for Water and Wastewater Treatment: A Review". Water **10**: 1828, 2018.

43. LEE, J., VON GUNTEN, U. & KIM, J. H. "Persulfate-Based Advanced Oxidation: Critical Assessment of Opportunities and Roadblocks". Environ. Sci. Technol. **54**: 3064, 2020.

44. AO, X., LIU, W., SUN, W., CAI, M., YE, Z., YANG, C., LU, Z. & LI, C. "Medium pressure UV-activated peroxymonosulfate for ciprofloxacin degradation: Kinetics, mechanism, and genotoxicity". Chem. Eng. J. **345**: 87, 2018.

45. CHEN, Y., LI, M., TONG, Y., LIU, Z., FANG, L., WU, Y., FANG, Z., WU, F., & HUANG, L. Z. "Radical generation via sulfite activation on $NiFe_2O_4$ surface for estriol removal: Performance and mechanistic studies". Chem. Eng. J. **368**: 495, 2019.

46. JI, Y., KONG, D., LU, J., JIN, H., KANG, F., YIN, X. & ZHOU, Q. "Cobalt catalyzed peroxymonosulfate oxidation of tetrabromobisphenol A: Kinetics, reaction pathways, and formation of brominated by-products". J. Hazard. Mater. **313**: 229, 2016.

47. JI, Y., SHI, Y., DONG, W., WEN, X., JIANG, M. & LU, J. "Thermo-activated persulfate oxidation system for tetracycline antibiotics degradation in aqueous solution". Chem. Eng. J. **298**: 225, 2016.

48. PAN, X., CHEN, J., WU, N., QI, Y., XU, X., GE, J., WANG, X., LI, C., QU, R., SHARMA, V. K. & WANG, Z. "Degradation of aqueous 2,4,4′-Trihydroxybenzophenone by persulfate activated with nitrogen doped carbonaceous materials and the formation of dimer products". Water Res. **143**: 176, 2018.

49. XIAO, S., CHENG, M., ZHONG, H., LIU, Z., LIU, Y., YANG, X. & LIANG, Q. "Iron-mediated activation of persulfate and peroxymonosulfate in both homogeneous and heterogeneous ways: A review". Chem. Eng. J. **384**: 2020.

50. YUN, W. C., LIN, K. Y. A., TONG, W. C., LIN, Y. F. & DU, Y. "Enhanced degradation of paracetamol in water using sulfate radical-based advanced oxidation processes catalyzed by 3-dimensional Co_3O_4 nanoflower". Chem.

Eng. J. **373**: 1329, 2019.

51. ZHAO, Q., MAO, Q., ZHOU, Y., WEI, J., LIU, X., YANG, J., LUO, L., ZHANG, J., CHEN, H., CHEN, H. & TANG, L. "Metal-free carbon materials-catalyzed sulfate radical-based advanced oxidation processes: A review on heterogeneous catalysts and applications". Chemosphere **189**: 224, 2017.

52. ZHOU, L., YANG, X., JI, Y. & WEI, J. "Sulfate radical-based oxidation of the antibiotics sulfamethoxazole, sulfisoxazole, sulfathiazole, and sulfamethizole: The role of five-membered heterocyclic rings". Sci. Total Environ. **692**: 201, 2019.

53. WACŁAWEK, S., LUTZE, H. V., GRÜBEL, K., PADIL, V. V., ČERNÍK, M. & DIONYSIOU, D. D. "Chemistry of persulfates in water and wastewater treatment: A review". Chem. Eng. J. **330**: 44, 2017.

54. KOPPENOL, W. H., STANBURY, D. M. & BOUNDS, P. L. "Electrode potentials of partially reduced oxygen species, from dioxygen to water". Free Radic. Biol. Med. **49**: 317, 2010.

55. KEARNS, D. R. "Physical and chemical properties of singlet molecular oxygen". Chem. Rev. **71**: 395, 1971.

56. YANG, Y., ZHANG, P., HU, K., ZHOU, P., WANG, Y., ASIF, A. H., DUAN, X., SUN, H. & WANG, S. " Crystallinity and valence states of manganese oxides in Fenton-like polymerization of phenolic pollutants for carbon recycling against degradation" Appl. Catal., B. **135**: 121593, 2022.

57. YANG, R., FAN, Y., YE, R., TANG, Y., CAO, X., YIN, Z. & ZENG, Z. "MnO_2 -Based Materials for Environmental Applications". Adv. Mater. **33**: 2021.

58. YANG, Y., ZHANG, P., HU, K., DUAN, X., REN, Y., SUN, H. & WANG, S. "Sustainable redox processes induced by peroxymonosulfate and metal doping on amorphous manganese dioxide for nonradical degradation of water contaminants". Appl. Catal. B Environ. **286**: 2021.

59. LIU, J., ZHAO, Z., SHAO, P. & CUI, F. "Activation of peroxymonosulfate with magnetic Fe_3O_4–MnO_2 core–shell nanocomposites for 4-chlorophenol degradation". Chem. Eng. J. **262**: 854, 2015.

60. SAPUTRA, E., MUHAMMAD, S., SUN, H., ANG, H. M., TADÉ, M. O. & WANG, S. "Different crystallographic one-dimensional MnO_2 nanomaterials and their superior performance in catalytic phenol degradation". Environ. Sci. Technol. **47**: 5882, 2013.

61. SAPUTRA, E., MUHAMMAD, S., SUN, H., ANG, H. M., TADÉ, M. O. & WANG, S. "Manganese oxides at different oxidation states for heterogeneous activation of peroxymonosulfate for phenol degradation in aqueous solutions". Appl. Catal. B Environ. **142**–**143**: 729, 2013.

62. ELIZAROVA, G. L., ZHIDOMIROV, G. M. & PARMON, V. N. "Hydroxides of transition metals as artificial catalysts for oxidation of water to dioxygen" Catal. Today. **58**: 71, 2000.

63. HE, D., LI, Y., LYU, C., SONG, L., FENG,W. & ZHANG, S. "New insights into MnOOH/peroxymonosulfate system for catalytic oxidation of 2,4-dichlorophenol: morphology dependence and mechanisms". Chemosphere. **255:** 126961, 2020.

64. LI, N., LI, R., YU, Y., ZHAO, J., YAN, B. & CHEN, G. "Efficient degradation of Bentazone via peroxymonosulfate activation by 1D/2D-MnOOH-RGO under simulated sunlight: performance and mechanism insight". Sci. Total Environ. **741:** 140492, 2020.

65. ZHANG, H., WANG, X., LI, Y., ZUO, K. & LYU, C. "A Novel MnOOH coated nylon membrane for efficient removal of 2,4-dichlorophenol through peroxymonosulfate activation". J. Hazard. Mater. **414:** 125526, 2021.

66. NGUYEN, T. B., LE, V. R., HUANG, C. P., CHEN, C. W., CHEN, L. & DONG, C. D. "Construction of ternary NiCo2O4/MnOOH/GO composite for peroxymonosulfate activation with enhanced catalytic activity toward ciprofloxacin degradation". Chem. Eng. J. **446:** 5, 2022.

67. LI, N., HE, M., LU, X., LIANG, L., LI, R., YAN, B. & CHEN, G. "Enhanced norfloxacin degradation by visible-light-driven Mn_3O_4/γ-MnOOH photocatalysis under weak magnetic field". Sci. Total Environ. **761:** 143268, 2021.

68. KAMAGATE, M., PASTUREL, M., BRIGANTE, M. & HANNA, K. "Mineralization Enhancement of Pharmaceutical Contaminants by Radical-Based Oxidation Promoted by Oxide-Bound Metal Ions". Environ. Sci. Technol. **54**: 476, 2020.

69. LIU, Y., LUO, J., TANG, L., FENG, C., WANG, J., DENG, Y., LIU, H., YU, J., FENG, H. & WANG, J. " Origin of the enhanced reusability and electron transfer of the carbon-coated Mn_3O_4 nanocube for persulfate activation". ACS Catal. **10:** 14857, 2020.

70. CRISOSTOMO, V. M. B., NGALA, J. K., ALIA, S., DOBLEY, A., MOREIN, C., CHEN, C. H., SHEN, X. & SUIB, S. L. "New synthetic route, characterization, and electrocatalytic activity of nanosized manganite". Chem. Mater. **19**: 1832, 2007.

71. VETTER, K. J. & JAEGER, N. "Potentialausbildung an der Mangandioxid-Elektrode als oxidelektrode mit nichtstöchiometrischem oxid". Electrochim. Acta. **11**: 401, 1966.

72. CHENG, F., SHEN, J., PENG, B., PAN, Y., TAO, Z. & CHEN, J. "Rapid room-temperature synthesis of nanocrystalline spinels as oxygen reduction and evolution electrocatalysts". Nat. Chem. **3**: 79, 2011.

73. LIANG, C., HUANG, C. F., MOHANTY, N. & KURAKALVA, R.M. "A rapid spectrophotometric determination of persulfate anion in ISCO". Chemosphere. **73:** 1540, 2008.

74. COLEDAM, D. A. C., SÁNCHEZ-MONTES, I., SILVA, B. F. & AQUINO, J. M. "On the performance of HOCl/Fe^{2+}, HOCl/Fe^{2+}/UVA, and HOCl/UVC processes using *in situ* electrogenerated active chlorine to mineralize the herbicide picloram". Appl. Catal. B Environ. **227**: 170, 2018. (2018).

75. MONTES, I. J. S., SILVA, B. F. & AQUINO, J. M. "On the performance of a hybrid process to mineralize the herbicide tebuthiuron using a DSA® anode and UVC light: a mechanistic study". Appl. Catal. B Environ. **200**: 237, 2017.

76. POWELL, C. "X-ray photoelectron spectroscopy database XPS, Version 4.1" NIST standard reference database, **20**: 1989.

77. VARGHESE, S.P., BABU, A.T., BABU, B. & ANTONY, R. "γ-MnOOH nanorods: efficient adsorbent for removal of methylene blue from aqueous solutions". J. Water Process Eng. **19**: 1, 2017.

78. MA, J., YANG, M., YU, F. & ZHENG, J. "Water-enhanced removal of ciprofloxacin from water by porous graphene hydrogel". Sci. Rep. **5**: 13578, 2015.

79. WANG, Q., ZHOU, D., LIN, K. & CHEN, X. "Carbon nitride–based cuprous catalysts induced nonradical-led oxidation by peroxydisulfate: role of cuprous and dissolved oxygen". Chem. Eng. J. **419**: 2021.

80. FERNANDES, C. H. M., SILVA, B. F. & AQUINO, J. M. "On the performance of distinct electrochemical and solar-based advanced oxidation

processes to mineralize the insecticide imidacloprid". Chemosphere. **275**, 2021.

81. SÁNCHEZ-MONTES, I., WACHTER, N., SILVA, B. F. & AQUINO, J. M. "Comparison of UVC-based advanced oxidation processes in the mineralization of bisphenol A: identification of oxidation by products and toxicity evaluation". Chem. Eng. J. **386**: 2020.

82. DING, D., ZHOU, L., KANG, F., YANG, S., CHEN, R., CAI, T., DUAN, X. & WANG, S. "Synergistic adsorption and oxidation of ciprofloxacin by biochar derived from metal-enriched phytoremediation plants: experimental and computational insights". ACS Appl. Mater. Interfaces. **12**: 53788, 2020.

83. ZHOU, Y., GAO, Y., PANG, S. Y., JIANG, J., YANG, Y., MA, J., YANG, Y., DUAN, J. & GUO, Q. "Oxidation of fluoroquinolone antibiotics by peroxymonosulfate without activation: kinetics, products, and antibacterial deactivation". Water Res. **145**: 210, 2018.

84. SHARMA, P. C,. JAIN, A., JAIN, S., PAHWA, R. & YAR, M. S. "Ciprofloxacin: review on developments in synthetic, analytical, and medicinal aspects". J. Enzym. Inhib. Med. Chem. **25**: 577, 2010.

85. YUAN, Z., SUI, M., YUAN, B., LI, P., WANG, J., QIN, J. & XU, G. "Degradation of ibuprofen using ozone combined with peroxymonosulfate". Environ. Sci. Water Res. Technol. **3**: 960, 2017.

86. QI, C., LIU, X., MA, J., LIN, C., LI, X. & ZHANG, H. "Activation of peroxymonosulfate by base: implications for the degradation of organic pollutants". Chemosphere. **151**:280, 2016.

87. ZHANG, H. &HUANG, C. H. "Oxidative transformation of fluoroquinolone antibacterial agents and structurally related amines by manganese oxide". Environ. Sci. Technol. **39:** 4474, 2005.

88. ANIPSITAKIS, G.P. & DIONYSIOU, D.D. "Radical generation by the interaction of transition metals with common oxidants". Environ. Sci. Technol. **38**: 3705, 2004.

89. WANG, J., B, H., YANG, M., LIU, R., HU, C., LIU, H. & QU, J. "Anaerobically-digested sludge disintegration by transition metal ions-activated peroxymonosulfate (PMS): comparison between Co^{2+}, Cu^{2+}, Fe^{2+} and Mn^{2+}". Sci. Total Environ. **713**: 2020.

90. ZHANG, B. T., ZHAO, L. & LIN, J. M. "Determination of folic acid by chemiluminescence based on peroxomonosulfate-cobalt(II) system". Talanta. **74**:1154, 2008.

91. TICHAPONDWA, S. M., NEWMAN, J. P. & KUBHEKA, O. "Effect of TiO_2 phase on the photocatalytic degradation of methylene blue dye". Phys. Chem. Earth Parts ABC, **118**: 2020.

92. HAN, X., ZHANG, H., ZHANG, C., ZHAO, Y., ZHANG, N. & LIANG, J. "Preparation of sepiolite nanofibers supported zero valent iron composite material for catalytic removal of tetracycline in aqueous solution". Front. Chem. **9**: 1, 2021.

93. WACHTER, N., AQUINO, J. M., DENADAI, M., BARREIRO, J. C., SILVA, A. J., CASS, Q. B., BOCCHI, N. & ROCHA-FILHO, R. C. "Electrochemical degradation of the antibiotic ciprofloxacin in a flow reactor using distinct BDD anodes: reaction kinetics, identification and toxicity of the degradation products". Chemosphere. **234**: 461, 2019.

94. GUAN, Y. H., MA, J., LI, X. C., FANG, J. Y. & CHEN, L. W. "Influence of pH on the formation of sulfate and hydroxyl radicals in the UV/peroxymonosulfate system". Environ. Sci. Technol. **45**: 9308, 2011.

95. KIRINO, Y., OHKUMA, T. & KWAN, T. "Spin trapping with 5, 5-dimethylpyrroline-n-oxide in aqueous solution". Chem. Pharm. Bull. **29**: 29, 1981.

96. DOMINGUES, P., DOMINGUES, M. R. M., AMADO, F. M. L., FERRER-CORREIA, A. J. "Detection and characterization of hydroxyl radical adducts by mass spectrometry". J. Am. Soc. Mass Spectrom. **12**: 1214, 2001.

97. GUO, Q., QIAN, S. Y. & MASON, R. P. "Separation and identification of DMPO adducts of oxygen-centered radicals formed from organic hydroperoxides by HPLC-ESR, ESI-MS and MS/MS". J. Am. Soc. Mass Spectrom. **14**: 862, 2003.

98. PAVLOVIC, J. & HOPKE, P.K. "Technical Note: detection and identification of radical species formed from α-pinene/ozone reaction using DMPO spin trap". Atmos. Chem. Phys. Discuss. **2009**: 23695, 2009.

99. LI, H. YUAN, N., QIAN, J. & PAN, B. "Mn_2O_3 as an electron shuttle between peroxymonosulfate and organic pollutants: the dominant role of surface reactive Mn(IV) species". Environ. Sci. Technol. **56**: 4498, 2022.

APPENDIX A

TEXT A1

UHPLC chromatographic conditions for the CIP oxidation byproducts

The samples were analyzed using an Agilent 1290 Infinity II Ultra High-Performance Liquid Chromatograph (UHPLC – from Agilent Technologies, Santa Clara, CA, USA). Chromatographic separation was performed using a Zorbax Eclipse Plus C18 column (50 mm × 2.1 mm i.d., 1.8 µm, Agilent, USA). The mobile phase consisted of 0.1% formic acid solution (solvent A) and methanol (solvent B). The chromatographic gradient used was as follows: 0-20 min, 65% B; 20-24 min, 65 to 85% B; 24-27 min, 85-65% B. Column oven and autosampler temperatures were set to 30 and 10°C, respectively. The mobile phase flow and injection volume were 0.250 mL min^{-1} and 2.0 µL, respectively.

Q-ToF MS analyses

Mass spectra were obtained using an Agilent 6545B Q-ToF MS system (Agilent Technologies, Santa Clara, CA, USA) equipped with an ESI Jet interface, operated in positive ion mode using a capillary voltage of 4.0 kV. The desolvation gas flow was 11 L min^{-1} and the gas flow in the cone was 8 L min^{-1}. The low and high collision energies were 6 V and from 12 to 17 V, respectively. Molecular ion and fragment ions were simultaneously obtained by the MSE acquisition mode. Data collected were analyzed ranging between 100 and 1000 Da and processed by the MassHunter Workstation Software version B.08.00 (Agilent Technologies, Santa Clara, CA, USA).

Analysis of CIP degradation products by UHPL-Q-ToF MS

The Q-ToF MS analyses were carried out in the MS fullscan and MSE modes to obtain information about the exact masses of the CIP standard and possible degradation products. For the sample analysis, we obtained work solutions of 10 mg L^{-1} diluted in ultrapure H2O (Milli-Q Direct - Q 3 UV, Millipore, Billerica, MA, USA). The total ion chromatograms (TIC) of samples in the ESI^+ positive ionization mode showed peaks of ion intensities corresponding to the degradation products of ciprofloxacin (CIP). The spectrometric parameters were optimized for the CIP standard. For identification of the main degradation products, several parameters were evaluated at low and high different collision energies.

TEXT A2

Experimental details for elucidating working oxidants

The use of DMPO and TEMP as spin probe were carried out using 5 mL of deionized H_2O (pH 3). In a typical experiment, 5 mg of MnOOH and 5 mg of PMS (corresponding to 1.0 g L^{-1} of each compound) were transferred to a 20 mL glass flask. Then, acidified H_2O (5 mL – pH 3) were added to start the reaction under magnetic stirring. After a 1 min reaction, 125 µL of a 4 mol L^{-1} DMPO (final concentration of 100 mmol L^{-1}) solution was added and the reaction was let for 1 min under stirring. After this time, to a 1 mL of sample, NaOH solution (60 µL of a 0.125 mol L^{-1}) was added to precipitate Mn(II) ions (pH ~7). Then, the samples were centrifuged for 30 s to separate the solid MnOOH. For ESR analyses, 200 µL of samples was transferred to a quartz capillary tube. The same procedure was used for the UHPLC analyses - see below the analyses details.

For the experiment using TEMP (50 mmol L^{-1}), only ESR measurements were carried out.

UHPLC chromatographic conditions for the DMPO oxidation byproducts

The oxidation products resulting from DMPO oxidation by unknown radicals were carried out by UHPLC using a Zorbax Eclipse Plus C18 column (50 mm × 2.1 mm i.d., 1.8 µm, Agilent, USA). The mobile phase consisted of 0.1% formic acid solution (solvent A) and acetonitrile (solvent B). A gradient elution mode at 0.350 mL·min^{-1} was used to separate the main products according to the following sequence: 0-1 min, 5% B; 1-10 min, 95% B; 10-10.1 min, 95-5% B; and 10.5-13 min, 5% B. The injection volume, column, and autosampler temperatures were set to 1.0 µL and 35ºC, respectively.

Q-TOF/MS analyses

Qualitative analyses were performed using an Agilent 6545B Q-ToF MS system (Agilent Technologies, Santa Clara, CA, USA) equipped with an ESI Jet interface, operated in positive ion mode using a capillary voltage of 2.0 kV. The desolvation gas flow and gas flow in the cone were 11 $L \cdot min^{-1}$ and 10 $L \cdot min^{-1}$, respectively. The collision energies ranged from 5 V to 16 V. Other variables such as source temperature, fragmentation voltage, skimmer voltage, and nozzle voltage were set to 300ºC, 40 V, 35 V and 225 V, respectively. Molecular and fragment ions were simultaneously obtained by the MS^E acquisition mode. Data collected were analyzed ranging from 50 to 600 Da and processed by the MassHunter Workstation Software version B.08.00 (Agilent Technologies, Santa Clara, CA, USA).

TABLE A1 - Pseudo-first order kinetic constants (*k*) for the removal of CIP and TOC at different pH conditions. Experimental conditions: 50 mg L^{-1} CIP, 1.0 g L^{-1} MnOOH, 1.0 g L^{-1} PMS, and 25 °C. Mean values were obtained after two repetitions.

pH	**CIP fraction**		**TOC fraction**	
	k_{1st} / 10^{-3} min^{-1}	R^2	k_{1st} / 10^{-3} min^{-1}	R^2
3.0	11 ±1	0.97 ±0.01	3.3 ±0.8	0.967 ±0.001
7.0	17 ±1	0.998 ±0.001	1.1 ±0.1	0.95 ±0.04
10.0	18 ±2	0.996 ±0.003	-	-

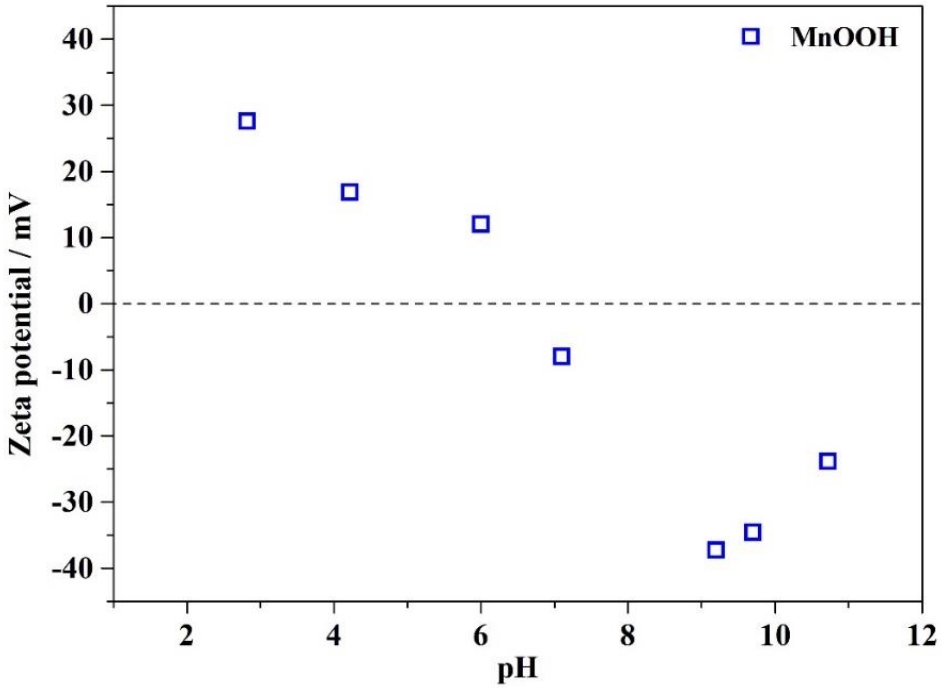

FIGURE A1 − Evolution of the zeta potential values as a function of the solution pH for the as-prepared MnOOH.

An indirect method proposed by Cattania *et al*. [1] and using XPS measurements was also carried out to estimate the pH_{pzc} of the catalyst. In this method, the pH_{pzc} is determined using the chemical shifts of different components in MnOOH together with the linear relationship shown in eq. 1:

$$pH_{pzc} = 11.32 - 1.14((BE_{O1s\ oxide} - 530.0) + (BE_{cation} - BE_{metal})) \quad (1)$$

where BE is the binding energy of the target component. In this case, BE_{cation} = 642.1 eV, $BE_{O1s\ oxide}$ = 530.8 eV and, BE_{metal} = 639.0 eV (value for Mn(s) obtained from [2]). Thus, the pH_{pzc} calculated was 6.9, a value that is in the range reported in the literature for synthetic and mineral MnOOH [3–6].

[1] M.G. Cattania, S. Ardizzone, C.L. Bianchi, S. Carella, An experimental correlation between points of zero charge and X-ray photoelectron spectroscopy chemical shifts of oxides, Colloids Surf. Physicochem. Eng. Asp. 76 (1993) 233–240. https://doi.org/10.1016/0927-7757(93)80083-Q.

[2] D. Briggs, in: D.E. Packham (Ed.), Handb. Adhes., John Wiley & Sons, Ltd, Chichester, UK, 2005: pp. 621–622. https://doi.org/10.1002/0470014229.ch22.

[3] S. Guo, W. Sun, W. Yang, Q. Li, J.K. Shang, Superior As(III) removal performance of hydrous MnOOH nanorods from water, RSC Adv. 5 (2015) 53280–53288. https://doi.org/10.1039/C5RA09157H.

[4] M. Ramstedt, B.M. Andersson, A. Shchukarev, S. Sjöberg, Surface properties of hydrous manganite (γ-MnOOH). A potentiometric, electroacoustic, and X-ray photoelectron spectroscopy Study, Langmuir. 20 (2004) 8224–8229. https://doi.org/10.1021/la0496338.

[5] X. Xu, Y. Zhang, S. Zhou, R. Huang, S. Huang, H. Kuang, X. Zeng, S. Zhao, Activation of persulfate by MnOOH: degradation of organic compounds by nonradical mechanism, Chemosphere. 272 (2021) 129629. https://doi.org/10.1016/j.chemosphere.2021.129629.

[6] M. Kosmulski, Compilation of PZC and IEP of sparingly soluble metal oxides and hydroxides from literature, Adv. Colloid Interface Sci. 152 (2009) 14–25. https://doi.org/10.1016/j.cis.2009.08.003.

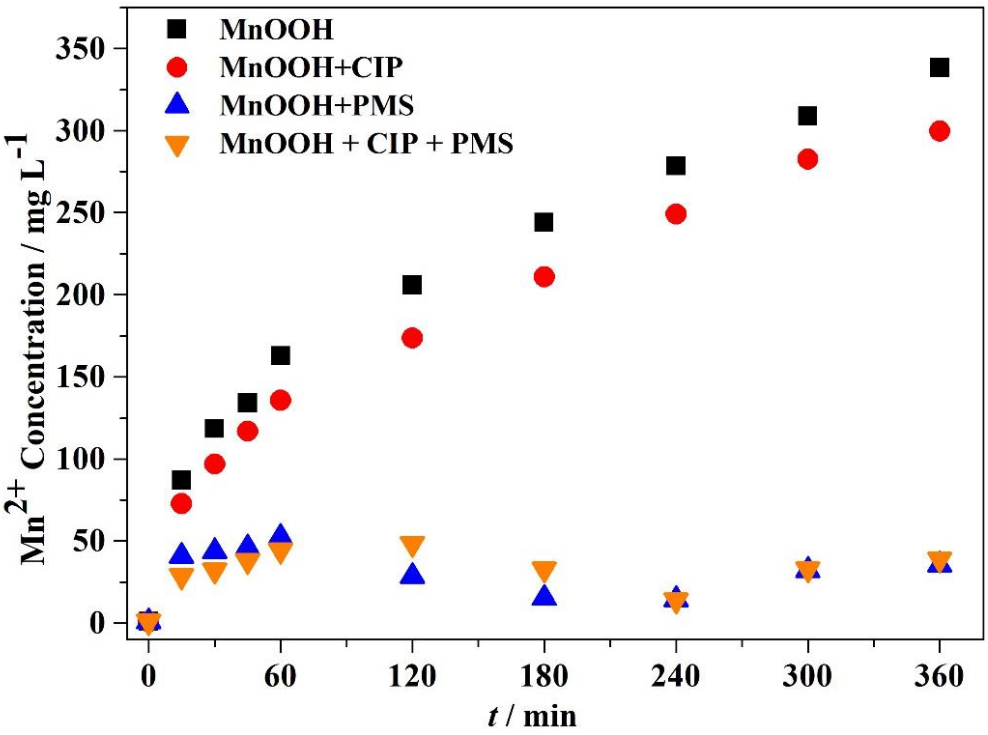

FIGURE A2 – Concentration of Mn(II) species leaching from the MnOOH during the reaction at acidic conditions for (■) MnOOH alone, (●) MnOOH/CIP, (▲) MnOOH/PMS, and (▼) MnOOH/CIP/PMS systems. Conditions: 50 mg L^{-1} CIP, 1.0 g L^{-1} MnOOH, 1.0 g L^{-1} PMS, pH 3.0, and 25 °C.

TABLE A2 - Pseudo-first order kinetic constants (*k*) for the removal of CIP and TOC at different PMS concentrations. Reaction conditions: 50 mg L^{-1} CIP, 1.0 g L^{-1} MnOOH, pH 3.0, and 25 °C. Mean values were obtained after two repetitions.

[PMS] / g L^{-1}	**CIP fraction**		**TOC fraction**	
	***k_{1st}* / 10^{-3} min^{-1}**	**R^2**	***k_{1st}* / 10^{-3} min^{-1}**	**R^2**
1.0	11 ±1	0.97 ±0.01	3 ±1	0.967 ±0.001
2.0	23 ±1	0.98 ±0.01	6 ±1	0.94 ±0.04
4.0	33 ±2	0.97 ±0.01	3. 0 ±0.4	0.89 ±0.03

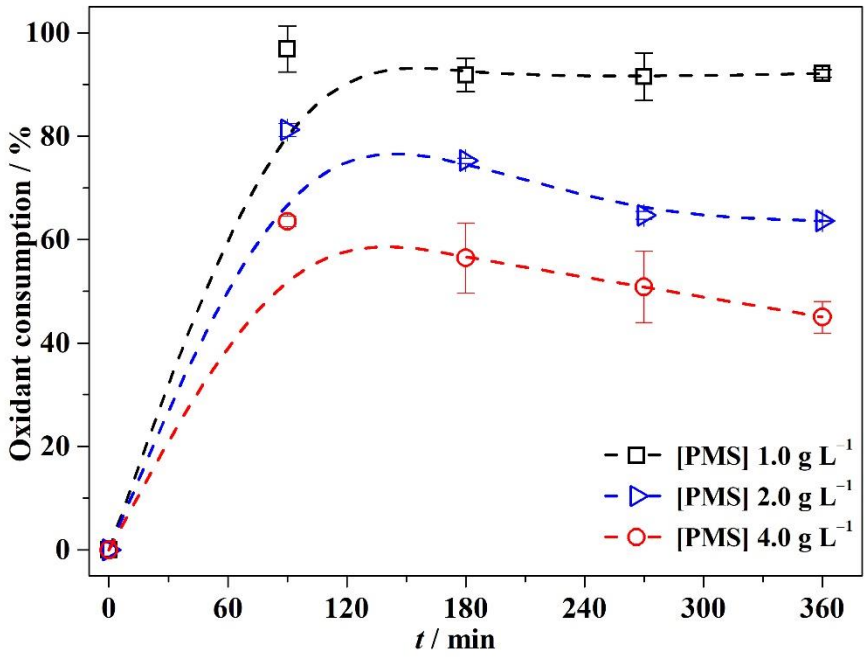

FIGURE A3 - Oxidant consumption during the CIP removal using different PMS concentrations: (□) 1.0, (▷) 2.0, and (○) 4.0 g L^{-1}. Experimental conditions: 50 mg L^{-1} CIP, 1.0 g L^{-1} MnOOH, pH 3.0, and 25 °C. Error bars refer to two repetitions.

TABLE A3 - Retention times, detected peaks in the ESI^+ mass spectra, and assignments for degradation products of CIP.

Product	Retention time / min	ESI Mode		
		m/z	**Attribution (ESI^+)**	**Error / ppm**
CIP	8.974	332.1408	$[M+H]^+$	-0.602
		314.1304	$[M+H-H_2O]^+$	
		288.1507	$[M+H-H_2O-CO_2]^+$	
		245.1081	$[M+H-CO_2-C_2H_5N]^+$	
P1	8.182	306.1258	$[M+H]^+$	1.307
		288.1142	$[M+H-H_2O]+$	
P2	9.612	348.1355	$[M+H]^+$	-1.436
		330.1243	$[M+H-H_2O]^+$	
P3	6.453	334.1198	$[M+H]^+$	-1.496
		316.1039	$[M+H-H_2O]^+$	
P4	11.425	362.1147	$[M+H]^+$	-1.380
		344.1039	$[M+H-H_2O]^+$	
P5	14.052	263.0827	$[M+H]^+$	-1.900
		245.0722	$[M+H-H_2O]^+$	

Experimental conditions: 50 mg L^{-1} CIP, 1.0 g L^{-1} MnOOH, 1.0 g L^{-1} PMS, pH 3.0 and 25 °C.

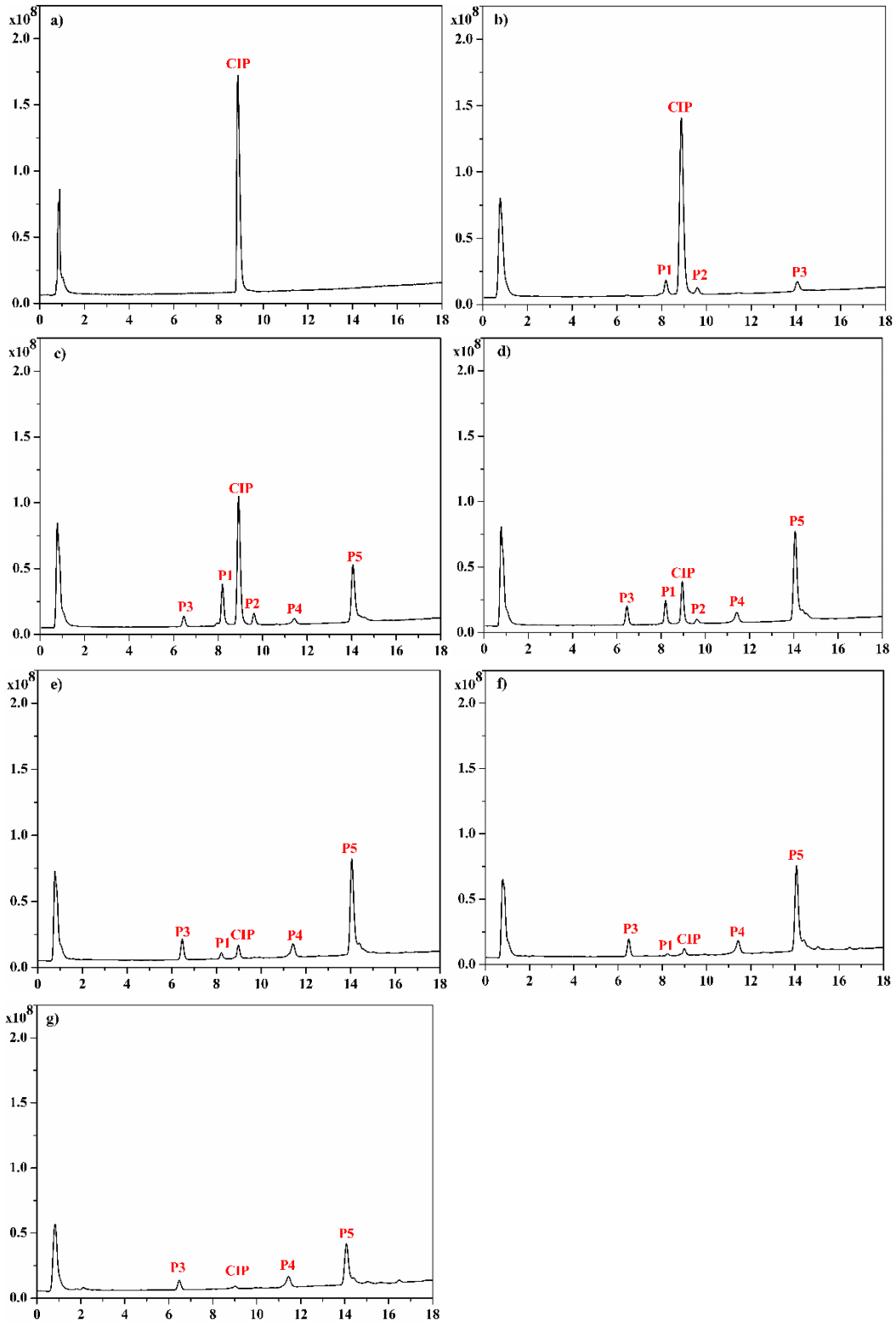

FIGURE A4 - Total ion chromatographic (TIC) profiles obtained from the separation method developed for CIP in the UHPLC-QToF MS mode at distinct treatment time: **a)** 0 h, **b)** 1 h, **c)** 2 h, **d)** 3 h, **e)** 4 h, **f)** 5 h, and **g)** 6 h.

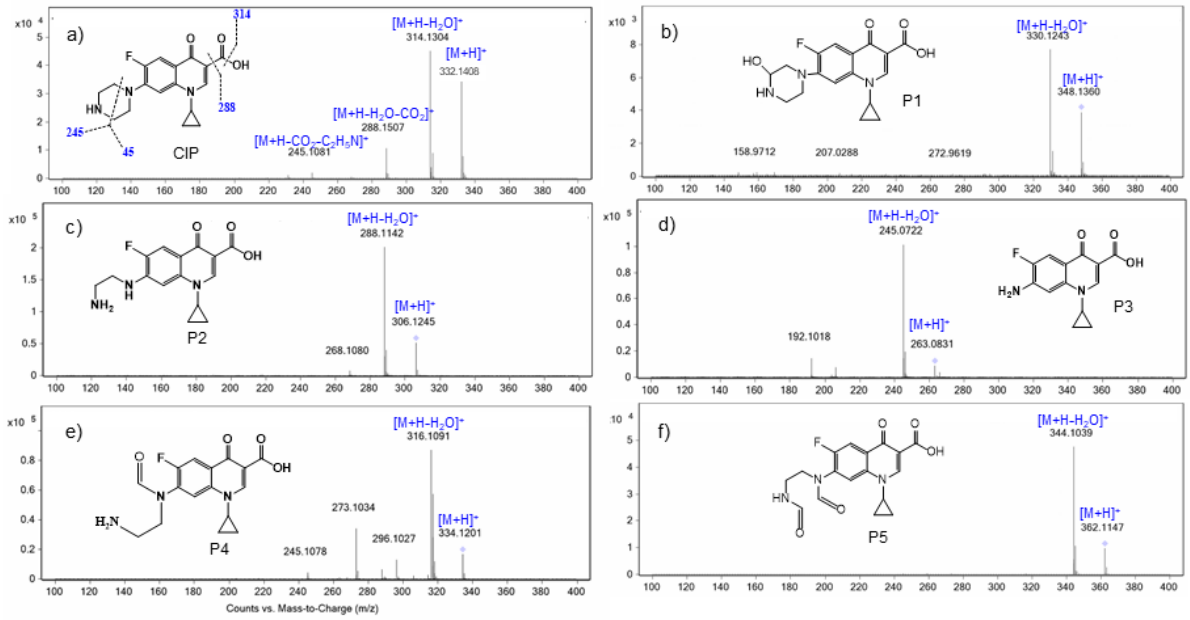

FIGURE A5 - UHPLC-QToF MS analyses by MS^E acquisition mode for CIP and its degradation products: **a)** CIP, **b)** P1, **c)** P2, **d)** P3, **e)** P4, and **f)** P5. Experimental conditions: 50 mg L^{-1} CIP, 1.0 g L^{-1} PMS, 1.0 g L^{-1} MnOOH, pH 3.0, and 25 °C.

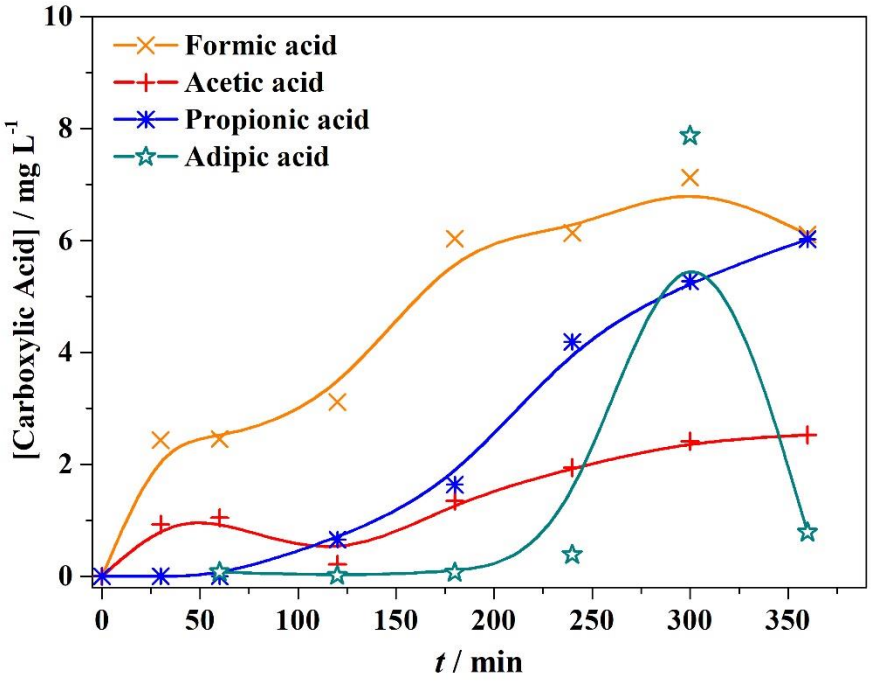

FIGURE A6 - Concentration evolution of the main detected carboxylic acids as a function of the treatment time (*t*) during the CIP degradation in the MnOOH/PMS system: (×) formic, (+) acetic, (✳) propionic, and (☆) adipic acid. Experimental conditions: 50 mg L^{-1} CIP, 1.0 g L^{-1} PMS, 1.0 g L^{-1} MnOOH, pH 3.0, and 25 °C.

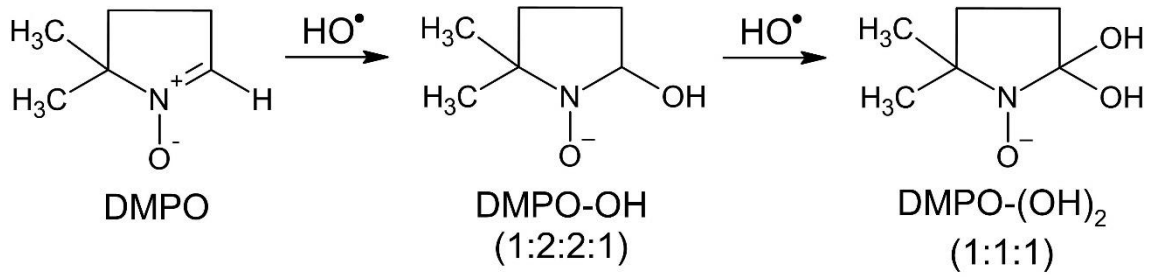

FIGURE A7 – Chemical structure of DMPO, DMPO-(OH) and DMPO-$(OH)_2$.

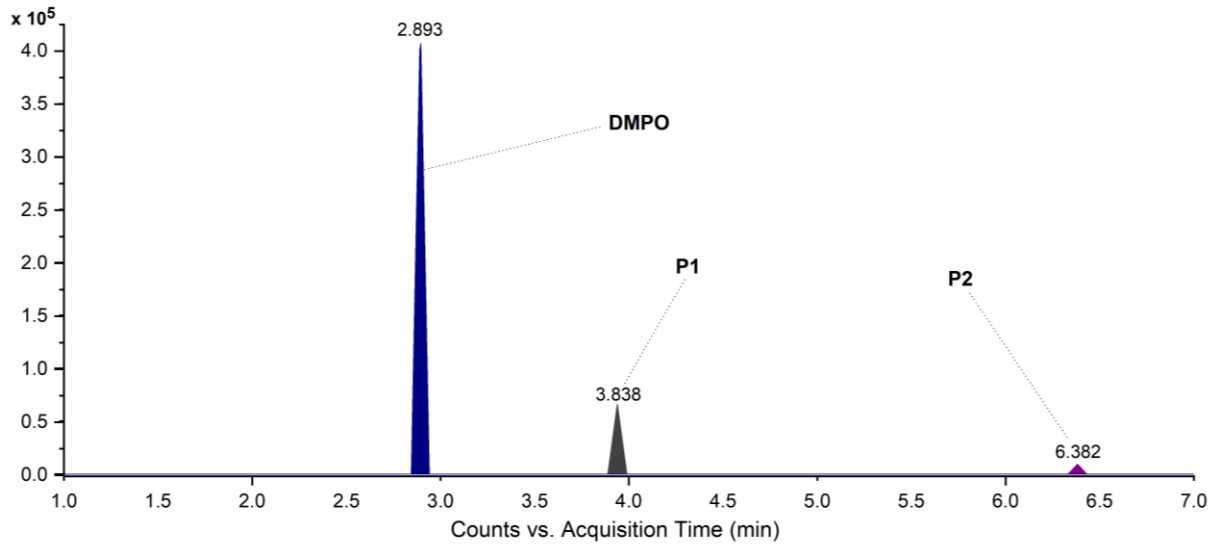

FIGURE A8 - Extracted ion chromatogram for identification of DMPO, DMPO-OH (P1) and DMPO-$(OH)_2$ (P2) by UHPLC-QToF MS.

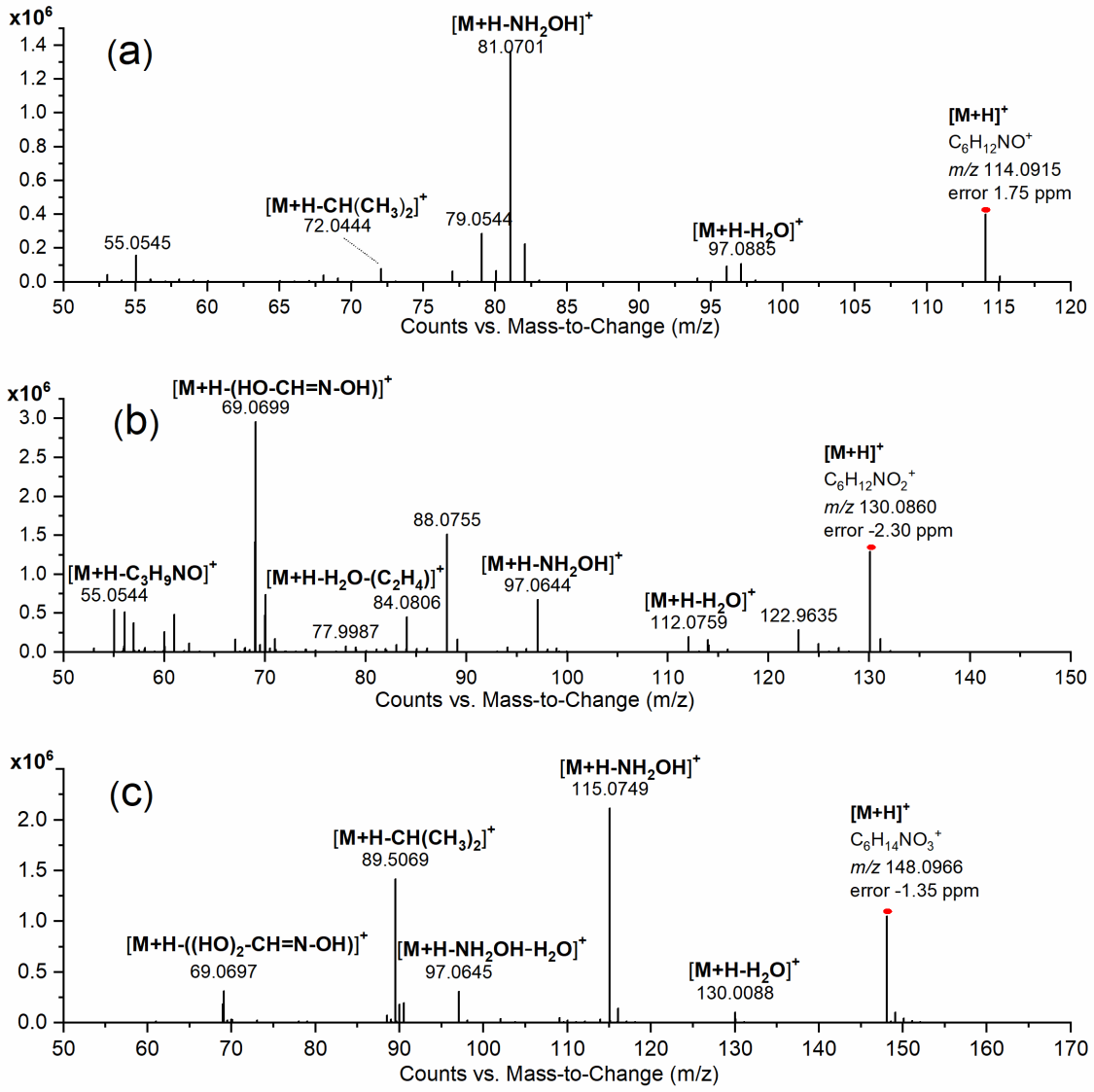

FIGURE A9 - MS/MS spectra of **a)** DMPO and its oxidation byproducts **b)** DMPO-OH, and **c)** DMPO-$(OH)_2$.

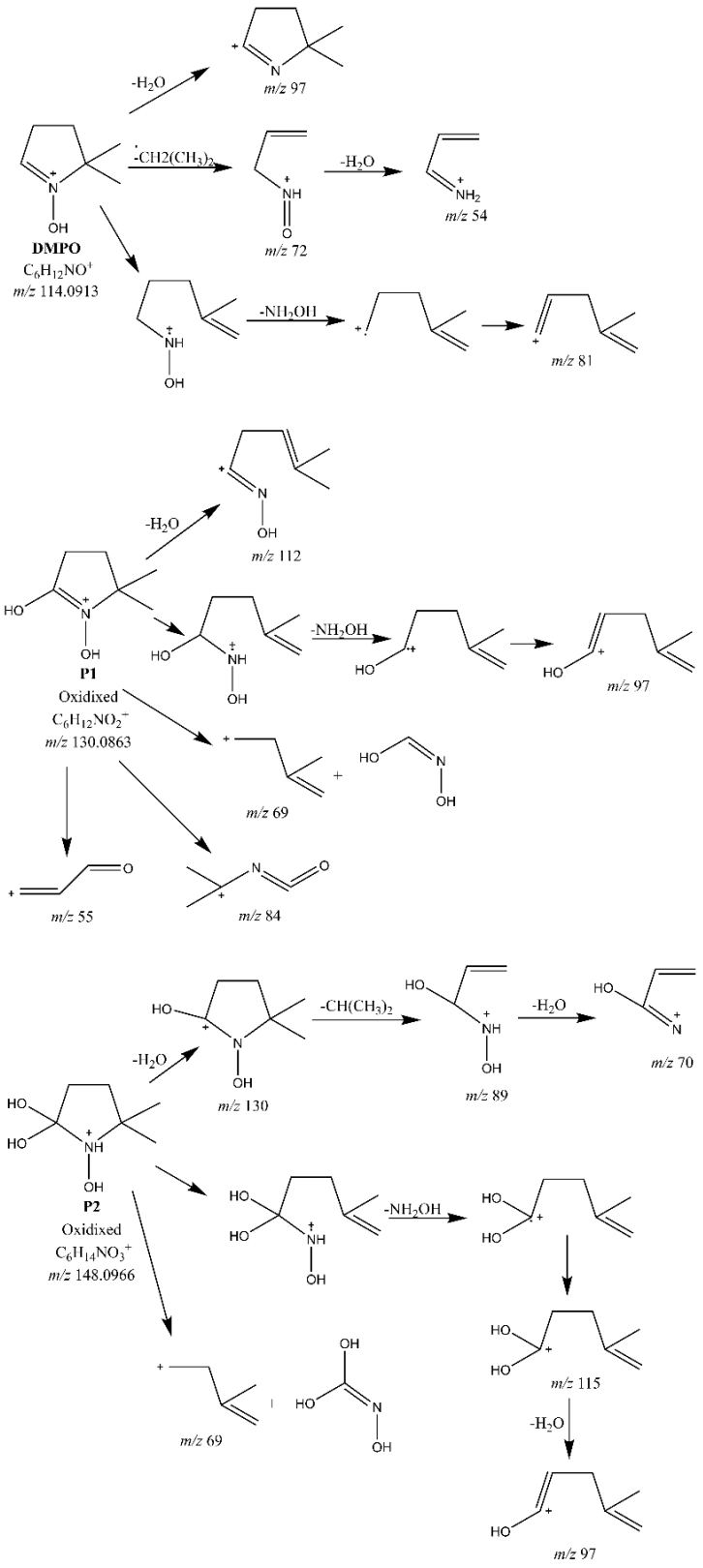

FIGURE A10 - Proposed fragmentation route for the DMPO (*m*/*z* 114.0913), DMPO-OH (P1: *m*/*z* 130.0863), and DMPO-$(OH)_2$ (P2: *m*/*z* 148.0966) compounds.

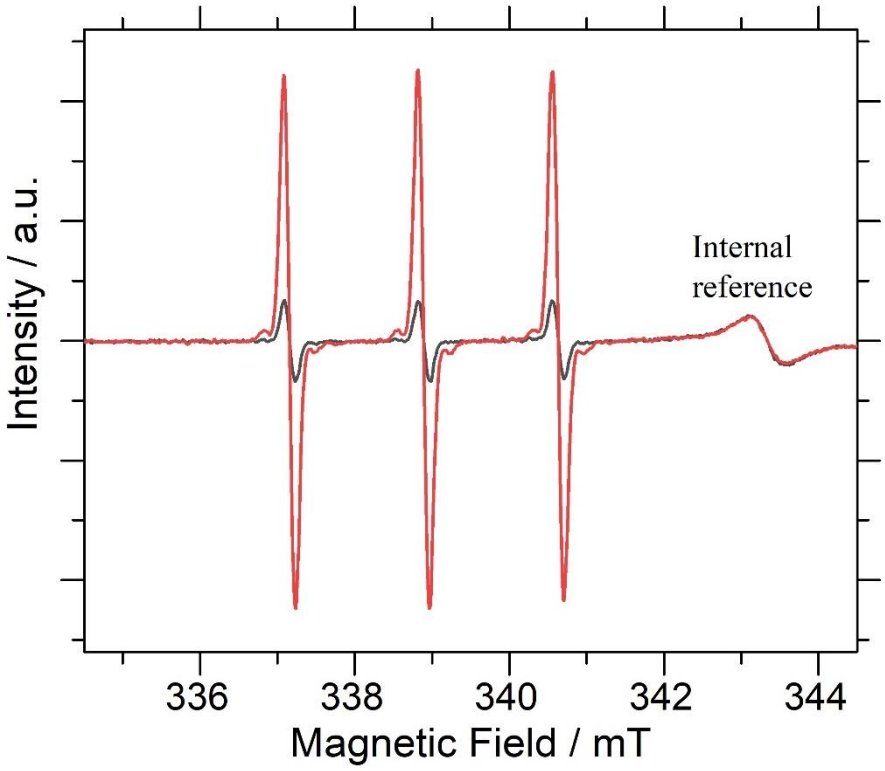

FIGURE A11 - Electron spin resonance measurement for the experiment using TEMP (black line) and TEMP in the presence of PMS (red line). Conditions: [TEMP] = 50 mmol L^{-1} and [PMS] = 1.0 g L^{-1}. No significant modifications were observed in the presence of MnOOH.

ESR measurement conditions: microwave frequency 9.51334 GHz; field amplitude modulation 1.0 G; frequency modulation 100 kHz; time constant 0.064 s; center field 3395 G; field sweep 100 G; sweep time 60 s; microwave power 20 mW.

TABLE A4 - Average oxidation state of Mn for MnOOH at distinct conditions: as-prepared (MnOOH) and after 3 h (3-MnOOH) and 6 h (6-MnOOH) of treatment. Experimental conditions: 50 mg L^{-1} CIP, 1.0 g L^{-1} PMS, 1.0 g L^{-1} MnOOH, pH 3.0, and 25 °C. Mean values were obtained after three repetitions.

Sample	**Mn average oxidation state**
MnOOH	3.02 ±0.03
3-MnOOH	3.26 ±0.03
6-MnOOH	3.357 ±0.001

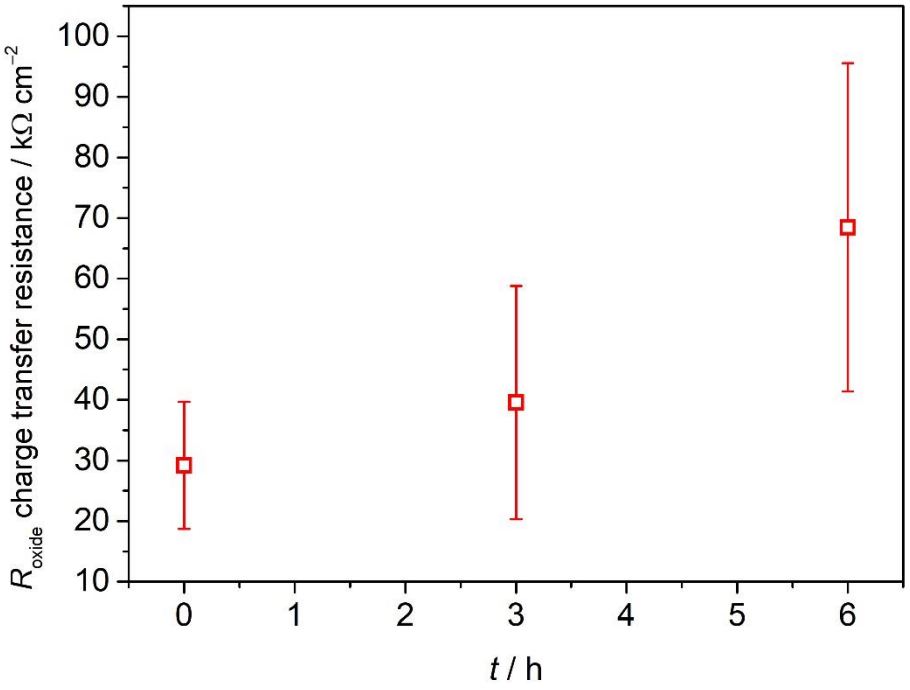

FIGURE A12 - Time evolution of the charge transfer resistance (R_{oxide}) before and after use of the MnOOH compound to activate PMS. The exposed area was close to 1 cm^2. Error bars refer to three repetitions.